MAGYAR ÁLLAMI
EÖTVÖS LORÁND
GEOFIZIKAI INTÉZET

GEOFIZIKAI
KÖZLEMÉNYEK

ВЕНГЕРСКИЙ
ГЕОФИЗИЧЕСКИЙ
ИНСТИТУТ
ИМ Л. ЭТВЕША

ГЕОФИЗИЧЕСКИЙ
БЮЛЛЕТЕНЬ

GEOPHYSICAL
TRANSACTIONS

EÖTVÖS LORÁND GEOPHYSICAL INSTITUTE OF HUNGARY

CONTENTS

VOL. 37. NO. 2–3. DEC. 1992. (ISSN 0016-7177)

BUDAPEST

TARTALOMJEGYZÉK

СОДЕРЖАНИЕ

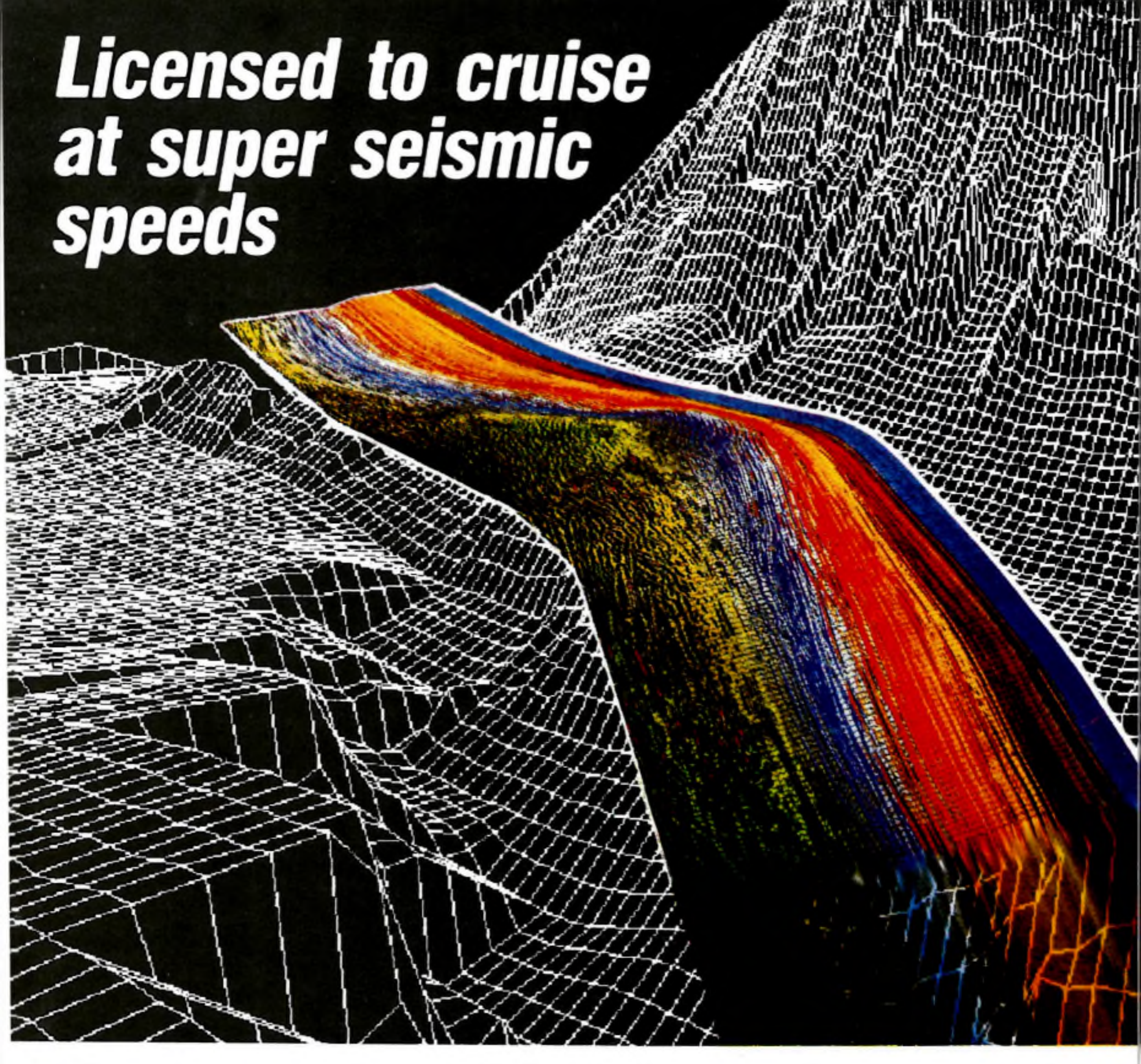

Licensed to cruise at super seismic speeds

EÖTVÖS L. GEOPHYSICAL INSTITUTE OF HUNGARY

THE OLDEST INSTITUTION FOR APPLIED GEOPHYSICS
OFFERS THE LATEST ACHIEVEMENTS FOR

GROUND-WATER PROSPECTING
and
ENVIRONMENTAL PROTECTION

The most often occurring demands:

- local geophysical measurements for the water supply of small communities by a few wells
- regional geophysical mapping to determine hydrological conditions for irrigation, regional agricultural development,
- large-scale exploration for the water supply of towns, extended areas i.e. regional waterworks,
- determination of bank storage of river terraces, planning of bank filtered well systems,
- thermal water exploration for use as an energy source, agricultural use or community utilization,
- cold and warm karst water prospecting,
- water engineering problems, water construction works

The Maxi-Probe electromagnetic sounding and mapping system – produced under licence by Geoprobe Ltd. Canada – is an ideal tool for shallow depths, especially in areas where seismic results are poor or unobtainable

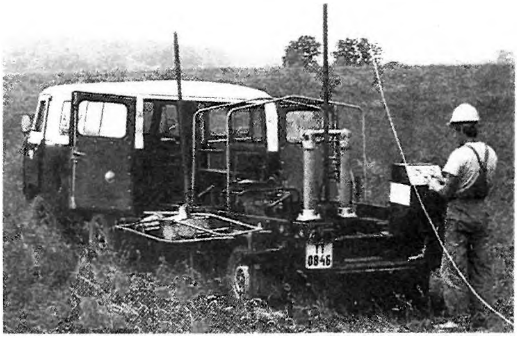

ELGI has a vast experience in solving problems of environmental protection such as control of surface waters, reservoir construction, industrial and communal waste disposal, protection of surface and ground water etc. ELGI's penetrologger provides in-situ information – up to a maximum depth of 30 m – on the strength, sand/shale ratio and density without costly drilling

Field work with ELGI's 24-channel portable seismograph

ELGI offers contracts with co-operating partners to participate in the whole complex process of exploration–drilling–production.

For further information ask for our booklets on instruments and applications. Let us know your problem and we will select the appropriate method and the best instrument for your purpose.

Our address: ELGI POB 35. Budapest,
H–1440. HUNGARY
Telex: 22-6194 elgi h

MAEGS 8

EVOLUTION OF INTRAMONTANE BASINS

8th Meeting of the Association of European Geological Societies

Topic:
EVOLUTION
OF INTRAMONTANE BASINS
ON THE EXAMPLE OF THE PANNONIAN BASIN WITH PARTICULAR EMPHASIS
ON SEQUENCE STRATIGRAPHY AND NEOTECTONICS

Schedule:

September	18 (Sat)	
	19-20 (Sun-Mon)	(A) Pre-Meeting Field Trip: Marginal Facies of the Pannonian Basin (including lignite deposits)
	21 (Tue)	Registration and Sightseeing in Budapest, with a visit to the Hungarian Geological Survey (founded in 1869)
	22-24 (Wed-Fri)	Technical Sessions (including a Poster Session)
	25-26 (Sat-Sun)	Post-Meeting Field Trips: (B) Geology, agriculture, environment and urban engineering. Geology in the Pannonian Basin. (C) Oil and gas, underground water, and geothermy in the Pannonian Basin.

Language: English

During the Meeting,
an All-European Regional Meeting of the International Geological Correlation Programme (IGCP)
will also be held

Address:
MAEGS-8 Org. Com.
Hungarian Geological Society
H-1027 Budapest, Fő u. 68. I. 102.
Hungary

Telephone: 36-1-251-0999; 36 - 1- 251 - 0089 / I. VETŐ
Telex: 61- 225220 (máfi h)
Telefax: 36 - 1 - 251 - 0703

GEOPHYSICAL TRANSACTIONS 1992
Vol. 37. No. 2-3. pp. 111-157

GENERALIZATION AND ROBUSTIFICATION OF THE COVARIANCE MATRIX

Béla HAJAGOS* and Ferenc STEINER*

After some unavoidable simplifications in Section 1 typical instances as well as problematic examples are given for the use of the inverse covariance matrix of the classical statistics for weighting. Because of the limited applicability of this matrix, in Section 2 a generalized version of the covariance matrix is introduced; its applicability is mostly shown using *P*-algorithms, i.e., weighted most freqent value calculations. The generalized inverse covariance matrix turned out to be valid also in the case of small samples if we use *P*-algorithms.

In Section 3 the method for determining this generalized covariance matrix is given as the robustification of the classical one; this determination is (from the viewpoint of the computation technique) consistent with the basic algorithms of the most frequent value procedures.

Keywords: correlation coefficient, asymptotic variance, general covariance matrix, robustification, most frequent value, dihesion

1. Introduction

1.1 Some definitions of classical statistics

The probability theory defines the covariance σ_{xy} of the random variables ξ and η well known as

$$\sigma_{xy} = E\left\{ [\, \xi - E(\xi)\,] \cdot [\eta - E(\eta)] \right\} \tag{1}$$

(E denotes the expected value). If the common density function is denoted by $f(x,y)$, the covariance is to be calculated as the following integral:

---

* University of Miskolc, H-3515 Miskoc-Egyetemváros
Manuscript received: 10 January, 1991

$$\sigma_{xy} = \int_{-\infty}^{\infty}\int_{-\infty}^{\infty} (x-E_x)\,(y-E_y)\,f(x,y)\;\mathrm{d}x\,\mathrm{d}y, \tag{2}$$

and if n pairs of data (x_i,y_i) are given, a very simple expression corresponds to Eq. (2):

$$\sigma_{xy} = \frac{1}{n}\sum_{i=1}^{n} (x_i-\bar{x})\,(y_i-\bar{y})\;; \tag{3}$$

the arithmetic means $\bar{x}$ and $\bar{y}$ are the estimates of the expected values E_x and E_y, respectively.

The degree of stochastic connection between ξ and η is measured by the correlation coefficient ρ_{xy} :

$$\rho_{xy} = \frac{\sigma_{xy}}{\sigma_x \cdot \sigma_y}\;; \tag{4}$$

σ_x and σ_y denote the corresponding scatters, i.e., the square roots of the variances, consequently the integral formula for ρ_{xy} is

$$\rho_{xy} = \frac{\displaystyle\int_{-\infty}^{\infty}\int_{-\infty}^{\infty} (x-E_x)\,(y-E_y,f(x,y)\;\mathrm{d}x\mathrm{d}y}{\sqrt{\displaystyle\int_{-\infty}^{\infty} (x-E_x)^2 f(x)\,\mathrm{d}x} \cdot \sqrt{\displaystyle\int_{-\infty}^{\infty} (y-E_y)^2 f(y)\,\mathrm{d}y}} \tag{5}$$

and the estimate of this value is calculated clearly as

$$\rho_{xy} = \frac{\displaystyle\sum_{i=1}^{n} (x_i-\bar{x})\cdot(y_i-\bar{y})}{\sqrt{\displaystyle\sum_{i=1}^{n} (x_i-\bar{x})^2} \cdot \sqrt{\displaystyle\sum_{i=1}^{n} (y_i-\bar{y})^2}}\;. \tag{6}$$

In the case of J random variables $\xi_1, \xi_2,\ldots,\xi_J$ the notations ρ_{jk} and σ_{jk} represent the correlation coefficient and the covariance of the variables ξ_j and ξ_k. If, similarly, σ_j and σ_k represent the corresponding scatters, the matrix of all covariances, i.e., the so-called covariance matrix $\mathbf{S}$, can be written as

$$\mathbf{S} = \begin{pmatrix} \sigma_1^2 & \rho_{12}\,\sigma_1\,\sigma_2 & \rho_{13}\,\sigma_1\,\sigma_3 & \cdots & \rho_{1J}\,\sigma_1\,\sigma_J \\ \rho_{12}\,\sigma_1\,\sigma_2 & \sigma_2^2 & \rho_{23}\,\sigma_2\,\sigma_3 & \cdots & \rho_{2J}\,\sigma_2\,\sigma_J \\ \cdot & & & & \\ \cdot & & & & \\ \rho_{J1}\,\sigma_1\,\sigma_J & \rho_{J2}\,\sigma_2\,\sigma_J & \rho_{J3}\,\sigma_3\,\sigma_J & \cdots & \sigma_J^2 \end{pmatrix} . \qquad (7)$$

This way of presentation of the covariances— used also in the famous article of INMAN [1975]— clearly shows their meaning and suggests that the interpretation of the correlation coefficients, presented in the correlation matrix

$$\rho = \begin{pmatrix} 1 & \rho_{12} & \rho_{13} & \cdots & \rho_{1J} \\ \rho_{21} & 1 & \rho_{23} & \cdots & \rho_{2J} \\ \cdot & & & & \\ \cdot & & & & \\ \rho_{J1} & \rho_{J2} & \rho_{J3} & \cdots & 1 \end{pmatrix} , \qquad (8)$$

is much more a primary quantity than that of the covariances, although the latter can directly be calculated according to Eqs. (2) or (3) and seemingly (see Eq. 4) the correlation coefficient is the secondary (inasmuch as it is derived) quantity.

1. 2 Simplifications

The significance of the correlation matrix of the errors in respect of inversion algorithms lies in the fact that its inverse can be appropriately used for weighting, see e.g. the already cited paper of INMAN, where a well defined geophysical inversion task is thoroughly treated (including the way of linearization, ridge regression, etc.). In contrast to this way of treatment, in the present paper from the point of view of the possible geophysical tasks only the simplest situation is supposed: direct measurements are made for the same quantity, say, for the rock porosity *n*, but not all data are characterized by the same probable error and/or by the same type of the error distribution. After this simplificaton we can pay full attention to problems of generalization and robustification.

For the clearest presentation of our trains of thought leading to the necessary generalization and robustification of the covariance matrix, however, some further simplifications are unavoidable. In all cases discussed in the present paper the inverse of the covariance matrix shall give the same weight, for n_a data another weight, for the remaining n_b data ($n_b = n-n_a$)i.e., n_a data will have equal weights and this is true for the remaining ones, too.

Consequently, if we give the weight w ($0 \leq w \leq 1$) for the n_a statistically equally behaving data and the weight ($1-w$) for the n_b (from the statistical aspect similarly equal) data, the error-curve of the results obtained by statistical algorithm as a function of w will have its minimum place w_{opt} determined by the inverse of the covariance matrix.

In this Introduction the 'statistical algorithm' mentioned above refers to the classical one, i.e., the minimization of the L_2-norm, — which is here simply the calculation of weighted means as according to our supposition direct measurements are made for the unknown geophysical quantity (say for the porosity of the rock at a given depth level).

Our simplifications enable us to write the variance σ_0^2 of the result x_0 in a simple analytical form, on the basis of the well known general expression

$$\sigma_0^2 = \sum_{i=1}^{n} c_i^2 \sigma_i^2 + \sum_{\substack{j,k=1 \\ j \neq k}}^{n} c_j c_k \rho_{jk} \sigma_j \sigma_k \tag{9}$$

which belongs to the random variable

$$\xi_0 = \sum_{i=1}^{n} c_i \xi_i \ . \tag{10}$$

(In Eq. (9), instead of the often used notations VAR (ξ_i) and COV(ξ_j,ξ_k) σ_i^2 and ρ_{jk} σ_j σ_k, respectively, are written in accordance with the notations already used in Eq. (7).)

If the random variables ξ_i are pair-wise independent, Eq. (9) reduces to

$$\sigma_0^2 = \sum_{i=1}^{n} c_i^2 \sigma_i^2 \ , \tag{11}$$

and this is to be written as

$$\sigma_0^2(w) = \frac{1}{[n_a w + n_b(1-w)]^2} \left\{ n_a w^2 \sigma_a^2 + n_b (1-w)^2 \sigma_b^2 \right\} \tag{12}$$

if (as was agreed earlier),

$$x_0 = \frac{1}{n_a w + n_b(1-w)} \left\{ w \cdot \sum_{i=1}^{n_a} x_i + (1-w) \cdot \sum_{i=n_a+1}^{n} x_i \right\} . \tag{13}$$

In Eq. (12) σ_a and σ_b represent the scatters (i.e., the square roots of the variances) of the n_a and n_b data.

The minimum place $\sigma_0^2(w)$ (see Eq. 12) is

$$w_{opt} = \frac{1/\sigma_a^2}{1/\sigma_a^2 + 1/\sigma_b^2} \tag{14}$$

(which is simply to verify by differentiation). This is in accordance with the following general form of the inverse of the covariance matrix valid for pair-wise independence of the random variables:

$$\mathbf{s}^{-1} = \begin{pmatrix} 1/\sigma_1^2 & 0 & 0 & \dots & 0 \\ 0 & 1/\sigma_2^2 & 0 & \dots & 0 \\ 0 & 0 & 1/\sigma_3^2 & \dots & 0 \\ \cdot & \cdot & \cdot & & \cdot \\ \cdot & \cdot & \cdot & & \cdot \\ 0 & 0 & 0 & \dots & 1/\sigma_n^2 \end{pmatrix} \tag{15}$$

The general form of matrix $\mathbf{s}^{-1}$ in the case of different mutual dependences of the random variables cannot be given in a simple way.

We shall discuss, however, only such cases when only n_b random variables are pair-wise dependent for the neighbouring indices characterized by the same correlation coefficient ρ. (Naturally n_b must now be an even number). Otherwise the simplification made in the independent case remains, i.e., there exits only two different variances σ_a^2 and σ_b^2, consequently the covariance matrix will have the following form:

$$
\mathbf{s} = \begin{array}{cc}
\left(\begin{array}{cccccccccc}
\sigma_a^2 & 0 & 0 & \cdot & \cdot & \cdot & \cdot & \cdot & \cdot & 0 \\
\cdot & & & & & & & & & \cdot \\
0 & \cdot & 0 & \sigma_a^2 & & & & & & 0 \\
0 & \cdot & 0 & 0 & \sigma_b^2 & \rho\sigma_b^2 & 0 & & \dots & 0 \\
0 & \cdot & 0 & 0 & \rho\sigma_b^2 & \sigma_b^2 & 0 & & \dots & 0 \\
\cdot & & & & & & & & & \\
0 & \cdot & \cdot & \cdot & \cdot & \cdot & \cdot & 0 & \sigma_b^2 & \rho\sigma_b^2 \\
0 & \cdot & \cdot & \cdot & \cdot & \cdot & \cdot & 0 & \rho\sigma_b^2 & \sigma_b^2
\end{array}\right) & \begin{array}{l} \\ n_a \text{ rows} \\ \\ \\ \\ \\ n_b \text{ rows} \\ \\ \end{array} \\
n_a \text{ columns} \qquad\qquad n_b \text{ columns} &
\end{array} \tag{16}
$$

In this special case $\mathbf{s}^{-1}$ also has a simple form: (17)

$$
\mathbf{s}^{-1} = \left(\begin{array}{ccccccccc}
1/\sigma_a^2 & 0 & 0 & \dots & \dots & \dots & \dots\ \dots & \dots & 0 \\
0 & \dots & 0 & 1/\sigma_a^2 & & & & & \cdot \\
0 & \dots & 0 & 0 & \frac{1}{\sigma_b^2(1-\rho^2)} & -\frac{\rho}{\sigma_b^2(1-\rho^2)} & 0 & \dots & 0 \\
0 & \dots & 0 & 0 & -\frac{\rho}{\sigma_b^2(1-\rho^2)} & \frac{1}{\sigma_b^2(1-\rho^2)} & 0 & \dots & 0 \\
\cdot & & & & & & \cdot & & \cdot \\
0 & \dots\ \dots & \dots & \dots & \dots & \dots\ 0 & & \frac{1}{\sigma_b^2(1-\rho^2)} & -\frac{\rho}{\sigma_b^2(1-\rho^2)} \\
0 & \dots\ \dots & \dots & \dots & \dots & \dots\ 0 & & -\frac{\rho}{\sigma_b^2(1-\rho^2)} & \frac{1}{\sigma_b^2(1-\rho^2)}
\end{array}\right)
$$

(the product of both matrices in Eqs. (16) and (17) should result in the unity matrix).

Now, the 'proposal' of the matrix $\mathbf{s}^{-1}$ for the weights to be applied is:

$$\begin{array}{ll} \dfrac{1}{\sigma_a^2} & \text{for } n_a \text{ data} \\ & \\ \dfrac{1}{\sigma_b^2\,(1+\rho)} & \text{for } n_b \text{ data} \end{array} \tag{18}$$

In our simplified case the notations of INMAN [1975] correspond to the following: $M=1$ and $P^0=0$ therefore $\Delta P=x_0$; $A=I$ (the unity matrix); $[\Delta G]_i = x_i$; $N^{-1} = \mathsf{S}^{-1}$. Consequently, the expression to be minimized (see Eq. (8) in the just cited article) simplifies to

$$\Phi = \sum_{i,k=1}^{n} \sigma_{ik}^{-1}\,(x_i - x_0)\,(x_k - x_0) \tag{19}$$

(in our notations) having clearly the minimum place defined by

$$c_i = \frac{\sum\limits_{k=1}^{n} \sigma_{ik}^{-1}}{\sum\limits_{i=1}^{n} \sum\limits_{k=1}^{n} \sigma_{ik}^{-1}} \tag{20}$$

(compare our Eq. (10); σ_{ik}^{-1} represent an element of the inverse covariance matrix S^{-1} . The same c_i-s are the results of course if we minimize the expression in our Eq. (9).) The weights in Eq. (18) clearly correspond to the general expression in Eq. (20), taking the actual S^{-1} (see Eq. 17) into consideration.

Expressing the results in Eq. (18) by the earlier introduced variable weight w,

$$w_{opt} = \frac{\dfrac{1}{\sigma_a^2}}{\dfrac{1}{\sigma_a^2} + \dfrac{1}{\sigma_b^2\,(1+\rho)}}\,, \tag{21}$$

(and this clearly reduces to the form given in Eq. (14) if $\rho = 0$). The same result is reached if the general expression in Eq. (9) is concretized to our actual case to get the analogue of Eq. (12):

$$\sigma_0^2\,(w) = \frac{1}{[n_a\, w + n_b\,(1-w)]^2} \left\{ n_a\, w^2 \sigma_a^2 + n_b\,(1-w)^2\,(1+\rho)\,\sigma_b^2 \right\} \tag{22}$$

and we look for the minimum place of this function by differentiation.

It is instructive to show in figures the variation of the error committed by the statistical algorithm used for the whole range of w ($0 \leq w \leq 1$). The 'probable error' (defined by Bessel) and denoted by q is frequently used by engineers: if F is the probability distribution function and F^{-1} its inverse,

$$q = \frac{1}{2}\,[F^{-1}(3/4) - F^{-1}(1/4)] \tag{23}$$

and therefore it is also called 'semi-interquartile range'. The 'semi-intersextile range' Q is similarly defined:

$$Q = \frac{1}{2}\,[\,F^{-1}(5/6) - F^{-1}(1/6)\,]\ . \tag{24}$$

It is obvious that it is twice as probable that absolute errors are *less* than Q, than *greater* than Q whilst these probabilities are equal using q as the error characteristic: one half of the errors are expected inside the interquartile interval, the other half outside of it. We shall use throughout the probable error q, which is to be calculated for a Gaussian error distribution well known as

$$q = 0.6745 \cdot \sigma\ . \tag{25}$$

Sometimes the curve of the semi-intersextile range Q in function of w will be also shown; for the Gaussian case

$$Q = 0.9674 \cdot \sigma \tag{26}$$

holds.

Our demands for accuracy are less rigorous in the case of the errors than in the case of the geophysically important quantities (depths, porosities, etc.) to be determined. If, say, by a geophysical depth-determination the relative error is 4%, this is meant as an error-range between 3.5% and 4.5 %, consequently the relative error of the error is here accepted to be 25 %. Indeed, the relative error of a simple determination of the scatter σ is $100/\sqrt{2n}$ % even in the least problematic case: when the data have Gaussian distribution. For example, if $n=8$, this error is obviously 25 %. (The just cited formula is a special variant of the expression in Eq. (55), namely for $a \to \infty$, *viz*, this limiting case corresponds to the Gaussian distribution of the errors.) Consequently, the difference between Q and σ of only some per cent for the gaussian distribution (see Eq. 26) can be neglected in nearly all practical cases. By theoretical investigations, however, naturally the exact connection given by Eq. (26) is to be taken into consideration.

1.3 Examples, problems, meditations

It is time to show some examples of classical fashion: firstly for Gauss-distributed data. Although on the grounds of Eqs. (22), (25) and (26) both theoretical curves $q(w)$ and $Q(w)$, respectively, are easy to construct for various situations, we also show Monte Carlo results for w = 0; 0.1; 0.2; ...; 0.9; 1.0. More exactly, for all situations random numbers in question N=1000 times were generated and the just investigated statistical algorithm applied in all investigated cases of this paper (this algorithm is, in the first examples, simply the calculation of the weighted average according to Eq. (13), i.e., an L_2-norm algorithm,) and the empirical q-value (sometimes also the Q-value) of these 1000 results were determined. For information about the statistical fluctuation of these probable errors, the whole procedure was repeated three times, and the values obtained were, on the one hand, separately demonstrated in all Figures, and on the other hand, also the interval of the actual fluctuation was indicated as short perpendicular straight line for all w-values. The self-consistence belonging to this demonstration of our Monte Carlo results throughout the paper proved to be fruitful.

In the first example are only (pair-wise) independent errors, all have Gaussian distribution but n_b=4 of them are characterized by $\sigma_b = \sqrt{2}$ and n_a=4 by $\sigma_a = 1$. (As random variables here and later have the meaning of error, the parameter of location will always be equal to zero.)

Fig. 1 shows that Monte Carlo results are in full agreement with the theoretical curve based on Eq. (12), including naturally the fact that w_{opt} is the same both for theoretical and Monte Carlo results. (The theoretical value of the w_{opt} in question will always be indicated on such Figures, sometimes the theoretical q-values for w=0 and 1, will be indicated too.)

In our second example all n=9 data have standard Gaussian distribution but only n_a=3 are independent, ξ_4 and ξ_5, ξ_6 and ξ_7, ξ_8 and ξ_9 are correlated with a correlation coefficient of $\rho = 0.6$. (This is in full agreement with our simplification in Section 1.2 and therefore it would have been enough to write n_b=6 and $\rho = 0.6$.) The Monte Carlo results and the theoretical curve $q(w)$ based on Eqs. (22) and (25) are shown in *Fig. 2*; the conclusions are the same as for Fig. 1. (The ρ-scale also shown in Fig. 2 indicates the w_{opt}-values for the corresponding ρ-s on the ground of Eq. (21) which simplifies in this concrete case to $w_{opt} = (1+\rho)/(2+\rho)$.)

It is illusory, however, always to expect such excellent agreement between theoretical and Monte Carlo results, e.g., if n_q data are Gauss-distributed characterized by $\sigma_G = 3$ and n_b have the density distribution

$$f_T(x) = (1-p)\cdot f_G(1;x) + p\cdot f_G(\sigma_c;x)\,, \quad (p < 0.5)\ , \tag{27a}$$

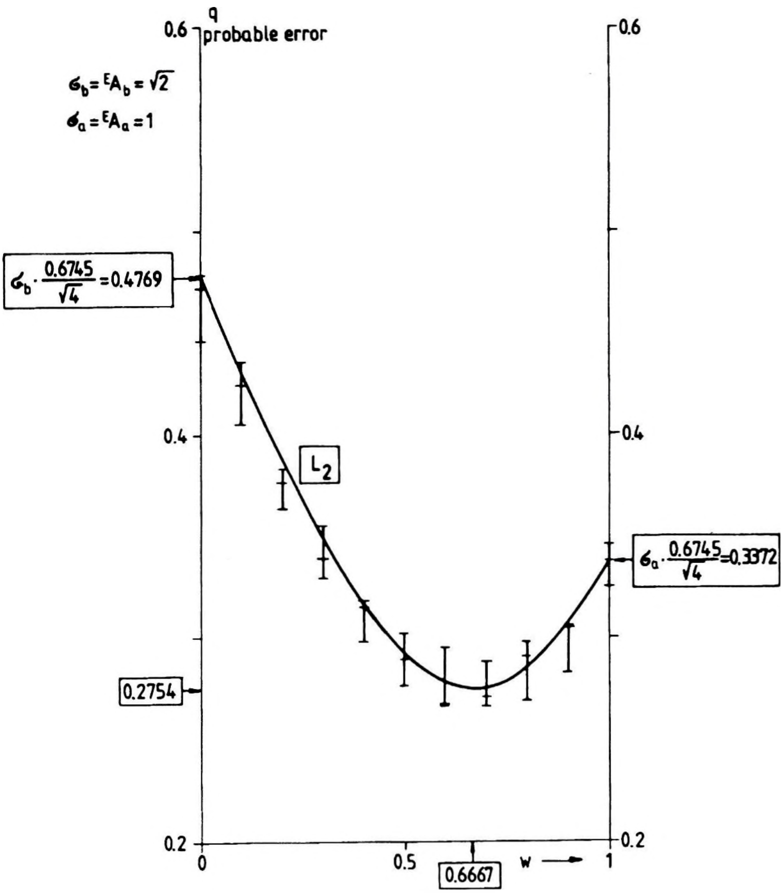

$$w_{opt} = \frac{1/\sigma_2^2}{1/\sigma_2^2 + 1/\sigma_1^2} = \frac{1}{1+1/2} = \frac{2}{3}$$

$$q_{min} = \frac{1}{4[1/\sigma_2^2 + 1/\sigma_1^2]} = 0.2754$$

Fig. 1. Error-curve of the results from the conventional L_2-algorithm, using different weights. The data are independent and Gauss-distributed; $n_a=n_b=4$. The best choice corresponds to the covariance matrix of classical statistics

1. ábra. A hagyományos L_2-algoritmussal nyert eredmények hibagörbéje különböző súlyok alkalmazásakor. A primer adatok függetlenek és Gauss-eloszlásúak ; $n_a=n_b=4$. Az a legjobb súlyválasztás, amely a klasszikus statisztika szerinti kovarianciamátrixnak felel meg

Рис. 1. Кривая погрешности результатов, полученных при традициональном альгорифме L_2 при применении разных весов. Первычные данные независимые и имеют Гауссовское распределение,$n_a=n_b=4$. Лучшим выбором веса является тот, который отвечает ковариационной матрице классической статистики

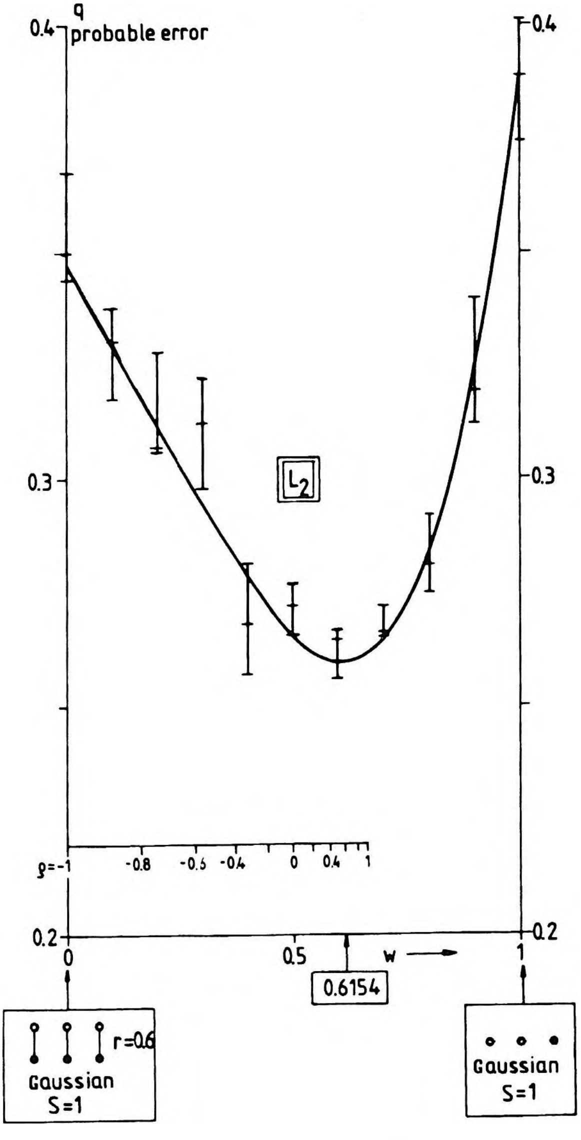

Fig. 2. Error-curve of the results from the conventional L_2-algorithm, using different weights (n_a= 3, n_b= 6; $r_{true}=\rho$= 0.6) . The best choice corresponds to the covariance matrix of classical statistics

2. ábra. A hagyományos L_2-algoritmussal nyert eredmények hibagörbéje különböző súlyok alkalmazásakor (n_a= 3, n_b= 6; $r_{true}=\rho$= 0,6). Az a legjobb súlyválasztás, amely a klasszikus statisztika szerinti kovarianciamátrixnak felel meg

Рис. 2. Кривая погрешности результатов, полученных при традиционном алгорифме L_2 при применении разных весов (n_a= 3, n_b= 6; $r_{true}=\rho$= 0,6). Лучшим выбором веса является тот, который отвечает ковариационной матрице классической статистики i.e., n_b data are Tukey-distributed. (See Eq. (83) in STEINER [1988]; in Eq. (27a) f_G represents the Gaussian density function

$$f_G(\sigma;x) = \frac{1}{\sigma\cdot\sqrt{2\pi}}\, e^{-x^2/2\sigma^2} \tag{27b}$$

In the monograph just cited the density function of arithmetic means for Tukey-distributed data is also given analytically, see Eq. (85).)

The scatter of the Tukey distribution is obviously

$$\sigma_T = \sqrt{(1-p)+p\cdot\sigma_c^2} \tag{27c}$$

and this means a value of $\sigma_T = 67.09$ if we take p=0.2 and σ_c=150 (this case is separately discussed in STEINER [1988]). As independence is also supposed, Eq. (14) would yield the appropriate w_{opt}-value but we have in this way $w_{opt} \approx 0$ in contradiction to the Monte Carlo results for n_a=n_b=1 shown in *Fig. 3a* where the choice w=0.9 seems the best (both $q(w)$ and $Q(w)$ curves are presented in the figure). Seemingly — at least belonging the minimum place — the Monte Carlo results correspont to the 'theoretical' expectations if n_a=n_b=4 (see also Fig. 3a) but this is not true for the whole range of w: we see in *Fig. 3b* (where other ordinate scaling is used) that the q-value from Monte Carlo calculations for w=1 is only a small fraction of the 'theoretical value' according to Eq. (12) which is to be calculated in this case simply as $0.6745\cdot\sigma_T/\sqrt{4}$.

The foregoing calls attention to the fact the scatters in the covariance matrix would be misinterpreted as the minimum of the L_2 norm of the differences $(x-x_0)$ for the other distribution: they are to be understood, on the contrary, as asymptotic scatters of the arithmetic means.

The asymptotic scatter is defined for estimates as

$$A = \lim_{n\to\infty}\sqrt{n}\cdot\sigma_{est} \tag{28}$$

where σ_{est} is the empirical scatter of the estimates. As the estimates frequently approximate Gaussian distribution [see e.g. HUBER 1981] if $n\to\infty$ the approximation $q = 0.6745\cdot A/\sqrt{n}$ or $Q = 0.9674\cdot A/\sqrt{n}$ can be adequately used (see also Eq. (25) and (26)). If we say only 'variance', it means the asymptotic variance of the arithmetic averages.

The foregoing means that the weigthing given by the inverse covariance matrix is to be understood asymptotically, — but what about small samples? In the extreme case n_a=1 shown in Fig. 3a for the weight w=1 is clearly the semi-interqartile range of the mother distribution and it is authentic and not the value $0.6745\cdot\sigma_T$; the former is about an order less in the cited case than in the latter. This means that acceptable results by using the inverse covariance matrix for weighting are to be expected for

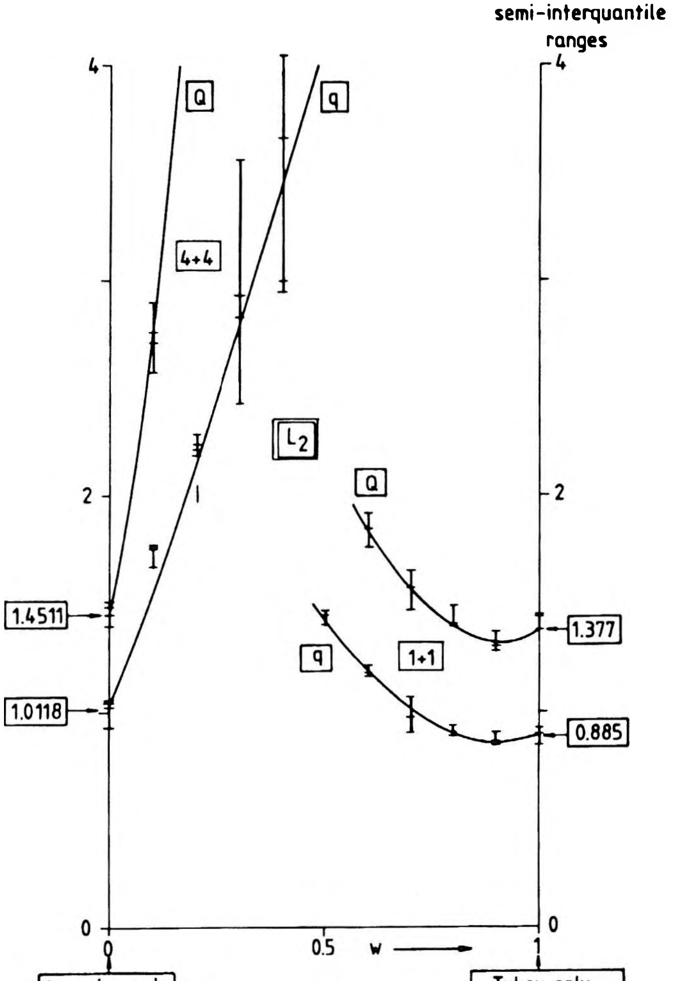

Fig. 3a. Error-curve of the results from the conventional L_2-algorithm, using different weights. The best choice for $n_a=n_b=1$ does not correspond to the classical covariance matrix: w_{opt} can be calculated from the q- and Q-values, respectively, of the mother distributions

3a. ábra. A hagyományos L_2-algoritmussal nyert eredmények hibagörbéje különböző súlyok alkalmazásakor. Az $n_a=n_b=1$ esetben a legjobb súlyválasztás nem felel meg a klasszikus kovarianciamátrixból következőknek: w_{opt} az anyaeloszlások q- ill. Q-értékeiből számítható

Рис. 3а. Кривая погрешности результатов, полученных при традиционный алгорифме L_2 при применении разных весов. В случае $n_a=n_b=1$ лучший выбор веса не отвечает следтствиям классической ковариационной матрици : w_{opt} вычисляется по значениям q и Q матерных распределений

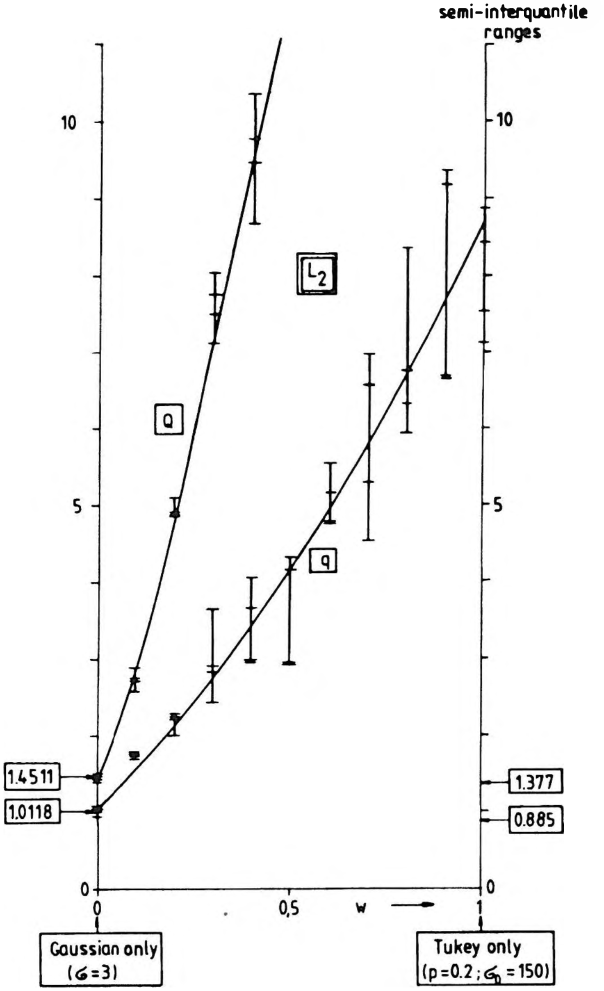

Fig. 3b. Error-curve of the results from the conventional L_2-algorithm, using different weights (n_a=n_b=4). The error-value at w=1 is only a small fraction of the value calculated on the basis of the variance

3b. ábra. A hagyományos L_2-algoritmussal nyert eredmények hibagörbéje különböző súlyok alkalmazásakor (n_a=n_b=4). A w=1-nél csak egy törtrésze az eredmény hibája a szórásból számíthatónak

Рис. 3b. Кривая погрешности результатов, полученных при традиционный алгорифме L_2 при применении разных весов (n_a=n_b=4). При w=1 погрешность результата является лишь дробной частью величины small samples only if the q- and/or the Q-values of the mother distribution do not differ significantly from 0.6745 $\cdot\sigma$ and 0.9674 $\cdot\sigma$, respectively. If this is not the case, n must be large for the adequate use of $\mathbf{S}^{-1}$ for weighting.

In the next example the samples are not yet small: $n_a=n_b=100$ holds. Two types of the $f_m(x)$-supermodel were chosen (see Eq. (143) in STEINER [1988]), namely, for the type parameter values $m=1$ and $m=0.5$, leading on the one hand to the well known Laplace distribution characterized by the density function

$$f_L(x) = \frac{1}{2} e^{-|x|} \tag{29}$$

and, on the other hand, to a very peaky density function

$$f_{ne}(x) = e^{-2\sqrt{|x|}} \tag{30}$$

and therefore it seems to be appropriate to call this latter 'needle distribution'.

Both density functions are shown in *Fig. 4*. The flanks of the needle distribution are heavier than those of the Laplace distribution, therefore also the scatter ($\sigma_{ne} = 2.7386$) is significantly greater than that of the Laplace distribution ($\sigma_L = \sqrt{2}$) yielding, according to Eq. (14), a w_{opt}-value of 0.2105.

The Monte-Carlo results for the weighted means are near to the theoretical ones (see Fig. 5); the just given value of w_{opt} is fully satisfactory but some differences still exist in the neighbourhood of $w=1$ (i.e., $n_a=100$ is not yet enough in this case to speak justifiably about the practically 'total fulfilment' of the asymptotic rule, see the L_2-curve in *Fig. 5,* because of the long tails of the f_{ne} distribution).

In Fig. 5 Monte-Carlo results for weighted medians are also demonstrated (see the L_1-curve); the optimum value of w for this case (=0.8) has really nothing to do with the yet known value w_{opt}=0.2105 which applies to the conventional statistical algorithm (i.e., with the minimization of the L_2-norm, which is in our simplified situations nothing more than weighted mean-calculations). — This L_1 curve will be discussed later more thoroughly; we indicate here only the important fact that the *optimum values of the weights strongly depend upon the statistical algorithm used* and therefore appropriate generalization of the covariance matrix is unavoidable. This generalization must also be able to solve the problem that scatters (figuring in the covariance matrix of Eq. (7)) are often, i.e., for very many type-models of probability distributions, infinite, and also the primarily given definition of σ_{xy} (in Eq. (2)) can lose completely its meaning, e.g., if $f(x,y)$ is the density function of a two-varibale Cauchy distribution. As also

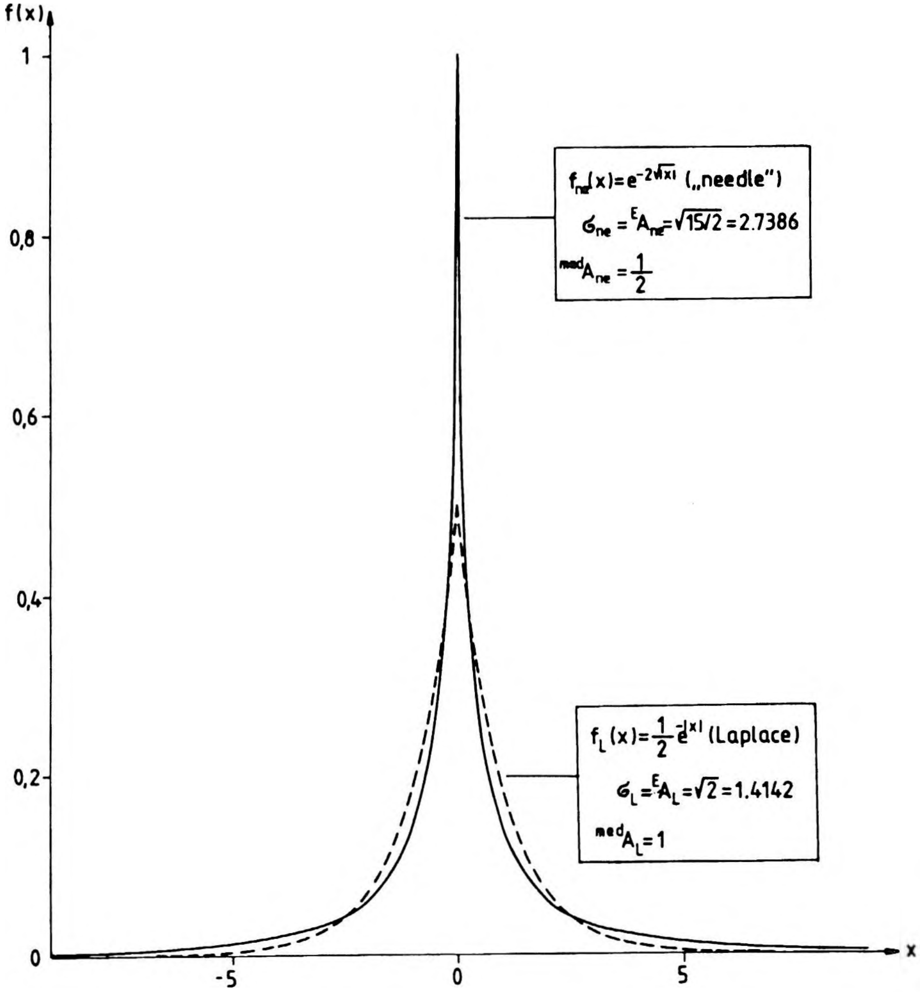

Fig. 4. Probability density function of the Laplace and the so-called 'needle' distribution; the latter is very peaky as well as having much heavier flanks than the Laplace distribution

4. ábra. A Laplace- és az ún. "tű"-eloszlás sűrűségfüggvénye. Az utóbbi egyrészt nagyon hegyes, másrészt viszont jelentősen súlyosabbak a szárnyai, mint a Laplace-eloszlásnak

Рис. 4. Функция плотности распределения Лапласа и иглового распределения. Последное с одной стороны слишком острое, однако его криля имеют больше весов, чем распределение Лапласа

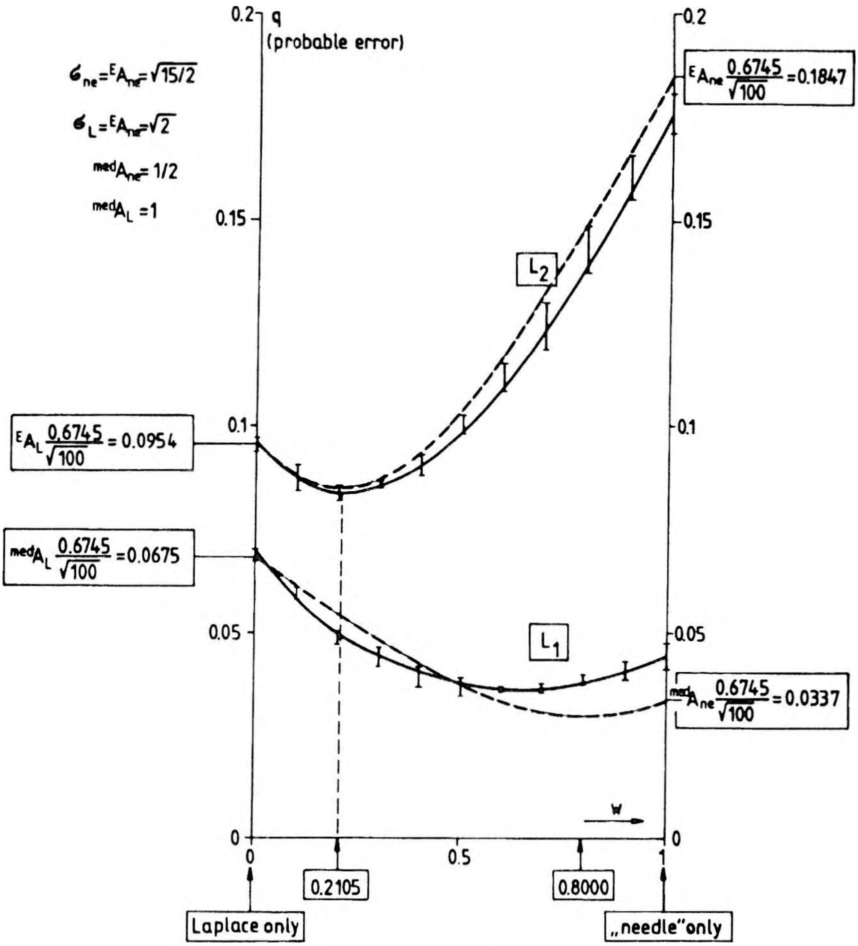

$$L_1:\ w_{opt}=\frac{1/{}^{med}A^2}{1/{}^{med}A^2_{ne}+1/{}^{med}A^2_L}=\frac{4}{4+1}$$

$$L_2:\ w_{opt}=\frac{1/\sigma^2_{ne}}{1/\sigma^2_{ne}+1/\sigma^2_L}=\frac{1/{}^{E}A^2_{ne}}{1/{}^{E}A^2_{ne}+1/{}^{E}A^2_L}=\frac{2/15}{2/15+1/2}=0.2105$$

Fig. 5. Error-curves of the results from the L_2-algorithm and the L_1-algorithm, respectively (n_a=n_b=100). The minimum place of the L_1-curve has nothing to do with the conventional covariance matrix but it is easy to interpret on the basis of the generalized one

5. ábra. Az L_2- ill. L_1-algoritmusokkal nyert eredmények hibagörbéi (n_a=n_b=100). Az L_1-görbe minimumhelyének semmi köze sincs a hagyományos kovarianciamátrixhoz, de könnyen magyarázható az általánosított kovarianciamátrix alapján

Рис.5. Кривые погрешности результатов, полученных по алгорифмам L_2 и L_1 (n_a=n_b=100). Минимум кривой L_1 не имеет ничего общего с традиционной ковариационной матрицей, но легко объясняется по обобщеной ковариационной матрице

ρ_{xy} in Eq. (4) has no meaning in these cases, obviously the correlation matrix must also be generalized.

2. Generalizations

2.1 Generalization of the covariance matrix if the errors are independent

Let $f(x)$ be the density function of the actual but unknown probability distribution. If we choose instead of $f(x)$ a well defined density function $g(x)$ as 'substituting distribution', the so-called I-divergence $I_g(f)$ is defined as

$$I_g(f) = \int_{-\infty}^{\infty} \ln \frac{f(x)}{g(x)} f(x)\, \mathrm{d}x \tag{31}$$

(see HAJAGOS [1982] or STEINER [1988]). As the I-divergence can be interpreted as a measure of the information loss, that T-value of the location parameter figuring in g can be with reason accepted as the most characteristic value for f, which minimizes the information loss, i.e., for them the relations

$$\frac{\partial I_g(f)}{\partial T} = 0 \tag{32}$$

and

$$\frac{\partial^2 I_g(f)}{\partial T^2} > 0 \tag{33}$$

are simultaneously fulfilled. It is easy to verify (see either of the just cited papers,) that both demands are fulfilled if the following integrals result in zero values:

$$\int_{-\infty}^{\infty} \frac{\frac{\partial g}{\partial T}}{g} f(x)\, \mathrm{d}x = 0 \tag{34}$$

and

$$\int_{-\infty}^{\infty} \frac{\frac{\partial^2 g}{\partial T^2}}{g} f(x)\,\mathrm{d}x = 0 \quad . \tag{35}$$

These equations define the statistical algorithm: Eq. (34) gives the algorithm for the determination of the location parameter *T*, Eq. (35) defines that of the parameter of scale (*S*). For example, if *g* is the Gaussian density function, Eq. (34) defines the formula for the expectant value *E* as the location parameter, Eq. (35) defines the formula for the variance σ^2; if *g* is the Cauchy density function, the Eqs. (34) and (35) define the twofold iteration for determining the most frequent value (as *T*) and the dihesion ε (as *S*); etc.

If the following integral denoted by ${}^{g}I$ is calculated such *T* and *S* simultaneously satisfy Eqs. (34) and (35), we get the 'developed information' using the statistical algorithm defined originally by the substituting distribution *g*:

$${}^{g}I = \int_{-\infty}^{\infty} \left(\frac{\frac{\partial g}{\partial T}}{g} \right)^2 \cdot f(x)\,\mathrm{d}x \quad . \tag{36}$$

(Another name for ${}^{g}I$ is 'relative information', see HAJAGOS [1982] where the definition of ${}^{g}I$ is first given.) The maximum value *I* of ${}^{g}I$ presents itself in the case of $g=f$; *I* is the well known Fisher-information. In this case the whole information is exhausted and therefore the straightforward definition of the efficiency *e* of the statistical algorithm defined by *g* is

$$e = {}^{g}I/I \quad ; \tag{37}$$

and it also seems appropriate to use ${}^{g}I$ as weights. HAJAGOS [1985] has shown that

$${}^{g}I = \frac{1}{{}^{g}A^2} \quad , \tag{38}$$

where ${}^{g}A^2$ is the asymptotic variance of the estimates if *g* defines (by means of Eqs. (34) and (35)) the statistical algorithm. Substituting the expression of ${}^{g}I$ given by Eq. (38) in Eq. (37), and taking also into considetarion that $I = 1/A^2_{\min}$, we in fact get the well known formula fot the efficiency

$$e = A^2_{\min}/{}^{g}A^2 \quad .$$

If Eq. (38) defines the weights for data characterized by different error distributions, the diagonal matrix of these weights can be considered as the inverse $({}^{g}A^{-1})$ of the following general covariance matrix:

$$
{}^{g}A = \begin{pmatrix} {}^{g}A_1^2 & 0 & \dots & 0 \\ 0 & {}^{g}A_2^2 & \dots & \cdot \\ \cdot & & & 0 \\ 0 & \dots & 0 & {}^{g}A_n^2 \end{pmatrix} ; \tag{39}
$$

${}^{g}A_i^2$ means here the asymptotic variance if the estimates concern the random variable ξ_i. From the general covariance matrix ${}^{g}A$ for independent random variables obviously follows the classical one if g is Gaussian:

$$
\mathbf{s} = \begin{pmatrix} \sigma_1^2 & 0 & \dots & 0 \\ 0 & \sigma_2^2 & & \cdot \\ \cdot & & & 0 \\ 0 & \dots & 0 & \sigma_n^2 \end{pmatrix} \tag{40}
$$

(the inverse of $\mathbf{s}$ was given in Eq. (15)), as the expected value E is defined by Eq. (34) if g is Gaussian, and the asymptotic variance of the estimates for E is well known the variance itself (i.e., σ_i^2 in case of ξ_i). — It is convenient to denote also by an arbitrary statistical algorithm the asymptotic scatter ${}^{g}A$ by the characteristic itself which is estimated, e.g., if g is the Laplace distribution, the median (med) of ξ is estimated (as it can easily be verified on the ground of Eq. (34)), therefore ${}^{med}A$ is written in this case (and ${}^{E}A \equiv \sigma$ evidently holds). The only exception is the standard version of the most frequent value calculations, i.e., if the theoretical value of M is estimated: simply A is written instead of ${}^{M}A$ and thus the covariance matrix has the form, in case of independence if the P-norm is minimized:

$$
A = \begin{pmatrix} A_1^2 & 0 & \dots & 0 \\ 0 & A_2^2 & & \cdot \\ \cdot & & & 0 \\ 0 & \dots & 0 & A_n^2 \end{pmatrix} . \tag{41}
$$

Instead of citing many papers we prefer to give in brief here the basic definitions and relations belonging to the P-norm, the standard version of the most frequent value calculations, etc.

The P-norm is defined as

$$P = \varepsilon \,.\, \exp\left\{\frac{1}{2}\cdot\int_{-\infty}^{\infty}\ln\left[\,1+\left(\frac{x-x_0}{2\,\varepsilon}\right)^2\right] f(x)\,\mathrm{d}x\right\} \tag{42}$$

where for ε (i.e., for the so-called dihesion)

$$\varepsilon^2 = \frac{3\displaystyle\int_{-\infty}^{\infty}\frac{(x-x_0)^2}{\left[\varepsilon^2+(x-x_0)^2\right]^2}\,f(x)\,\mathrm{d}x}{\displaystyle\int_{-\infty}^{\infty}\frac{1}{\left[\varepsilon^2+(x-x_0)^2\right]^2}\,f(x)\,\mathrm{d}x} \tag{43}$$

must hold iteratively. The minimum P-value is reached if $x_0=M$ is defined by

$$M = \frac{\displaystyle\int_{-\infty}^{\infty} s(x)\,x\,f(x)\,\mathrm{d}x}{\displaystyle\int_{-\infty}^{\infty} s(x)\,f(x)\,\mathrm{d}x}\;. \tag{44}$$

M is called the most frequent value (in standard version); the functions $s(x)$ is defined by

$$s(x) = \frac{4\,\varepsilon^2}{4\varepsilon^2+(x-M)^2}\;. \tag{45}$$

Eqs. (44) and (43) simultaneously define M and ε (in Eq. (43) naturally $x_0=M$ must be substituted); in the case of a homogeneous sample $x_1, \ldots, x_n$ the estimates for M and ε are calculated (by means of a twofold iteration) on the ground of the sum-counterparts of Eqs. (43) and (44). These equations are easy to get if we substitute

$$f(x) = \sum_{i=1}^{n} x_i\,\delta\,(x-x_i) \tag{46}$$

into Eqs. (43) and (44); for more details see the summarizing tables at the end of STEINER [1990] and [1991].

The asymptotic variance of the most frequent values is to be calculated according to

$$A^2 = \frac{\displaystyle\int_{-\infty}^{\infty}\frac{(x-M)^2}{[4\varepsilon^2+(x-M)^2]^4}\,f(x)\,\mathrm{d}x}{\left[\displaystyle\int_{-\infty}^{\infty}\frac{4\varepsilon^2-3\,(x-M)^2}{[4\varepsilon^2+(x-M)^2]^3}\,f(x)\,\mathrm{d}x\right]^2} \tag{47}$$

(see e.g. Eq (134) with k=2 in STEINER [1988]).

The most important question in respect of the inverse algorithms is the following: Do the basic statements concerning the optimum weighting discussed in Section 1 remain after this generalization of the covariance matrix? In particular if our independent data are distributed according to two different ways (we have agreed that this simplification is consequently used in this paper), does the analogue of Eq. (14), i.e.,

$$w_{opt} = \frac{1/{}^{g}A_a^2}{1/{}^{g}A_a^2 + 1/{}^{g}A_b^2} \tag{48}$$

really give the optimum weight? For example, for $L1$-norm algorithms (i.e., for calculation of sample medians) really

$$w_{opt} = \frac{1/{}^{med}A_a^2}{1/{}^{med}A_a^2 + 1/{}^{med}A_b^2} , \tag{49}$$

in the case of the P-norm (i.e., for calculations of the most frequent values) is

$$w_{opt} = \frac{1/A_a^2}{1/A_a^2 + 1/A_b^2} \tag{50}$$

really the best choice?

We have seen the Monte Carlo results from calculating medians in Fig. 5 (see once more the L_1-curve). The asymptotic scatter of the sample medians can be expressed (see e.g. CRAMÉR [1946]) simply as

$${}^{med}A = \frac{1}{2f(med)} \tag{51}$$

for the distributions defined in the Eqs. (29) and (30). The w_{opt}=0.8 value calculated according to Eq. (49) fully corresponds to the Monte Carlo results. In addition, the following analogue of Eq. (12) also seems to be valid for independent cases

$${}^{g}A_0^2(w) = \frac{1}{[n_a w + n_b(1-w)]^2} \left\{ n_a w^2 \cdot {}^{g}A_a^2 + n_b (1-w)^2 \cdot {}^{g}A_b^2 \right\} , \tag{52}$$

as by substituting ${}^{med}A$ instead of the general ${}^{g}A$ two times in Eq. (52), the theoretical $q(w)$ calculated as 0.6745. ${}^{med}A_0^2(w)$ is near to the Monte Carlo results.

Two remarks: a/ theoretical curves are drawn in the overwhelming majority of our figures with dashed lines; b/ as far as the applied constant 0.6745 is concerned, we refer once more to the fact that estimates very often have (but not always) Gaussian distribution (see HUBER [1981]).

The small departures between the theoretical curve and the Monte Carlo results in the neighbourhood of $w=1$ are similar using the L_1-norm as in the discussed case of the L_2-algorithm because $n_a=100$ is not enough to get complete accordance with the asymptotic rules. The reasons, however, are quite different: the flanks of f_{ne} are very elongated and therefore the sample size must be very large if we wish the averages to behave according to the asymptotic rule, the behaviour of the central zone has hardly any influence; — on the contrary: the calculation of the sample medians is extremely sensitive in the case of symmetrical and unimodal distributions to the data around the maximum place of the density curve if the latter has a peaky maximum but in the case of the extreme pointedness of f_{ne}-curve (see Fig. 4) $n_a=100$ is really not yet enough to detect accurately this feature of the density curve on the basis of the sample (it is completely indifferent in respect of the sample medians if the flanks are heavy or not).

In Fig. 1 we saw in the case of $n_a=n_b=4$ full agreement between Monte Carlo results and the theoretical curve expressing primarily asymptotic behaviour. The first example for the eventual discordance was shown on the right hand side of Fig. 3a: the Monte Carlo results have expressed well the characteristic of the *mother distribution itself,* — but this was *very far* from the theoretical value calculated according to the asymptotic rule, namely, on the ground of the *asymptotic scatter* (${}^{E}A = \sigma$) of the averages. The just discussed departures in Fig. 5 are traceable to similar origin, not only for L_2 but also for L_1, too.

From the viewpoint of geophysical practice it is very important that small samples also behave at least approximately according to the asymptotic rule and this is achieved if some significant characteristic of the mother distribution, say, q or Q, is near to the asymptotic scatter of the estimates obtained by the statistical algorithm in question. As according to Eq.(26), $Q \approx {}^{E}A = \sigma$ holds for the very classical, namely for the Gaussian case, we should see whether the intersextile range Q is far from or near to the asymptotic scatter of the standard most freqent value calculations (i.e., of the characteristic of the algorithms based on the P-norm, denoted by A) for frequently occuring mother distribution types.

The distribution types of the '$f_a(x)$-supermodel' defined by

$$f_a(x) = \frac{\Gamma(\frac{a}{2})}{\sqrt{\pi}\cdot\Gamma(\frac{a-1}{2})}\cdot\frac{1}{(1+x^2)^{a/2}} \qquad (a > 1) \qquad (53)$$

proved to be adequate for modelling actual error distributions which occur in geophysical practice. Introducing $p=1/(a-1)$ as parameter of type it can be proven that p_2-p_1 well approximates the type-distance of the corresponding distributions (defined by a_2 and a_1). Consequently it is straightforward to show all important characteristics as a function of p for a great type interval, mostly from the Gaussian (p=0) to the Cauchy distribution (p=1; for more details about the supermodel $f_a(x)$, e.g. Cramér-Rao bounds, efficiencies, etc., see STEINER [1988]).

In our case in *Fig. 6* the curve of the quotient A/Q was drawn as a function of p; for comparison the σ/Q curve is also shown in the same figure.

Our conclusion on the ground of the A/Q-curve of Fig. 6 is that $A \approx Q$ is satisfactorily fulfilled for a very broad type interval (from the Gaussian type at least to the Cauchy-distribution); consequently, it is justifiable to expect that *asymptotic rules are applicable* (with the demanded accuracy) *also for small samples if algorithms based on the P-norm are used.* As a lower limit four data in a sample can be expected because for only three data the notion 'most frequent value' is hard to interpret adequately (and for two data all algorithms investigated — based on L_1-, L_2- or P-norm — give the same estimate).

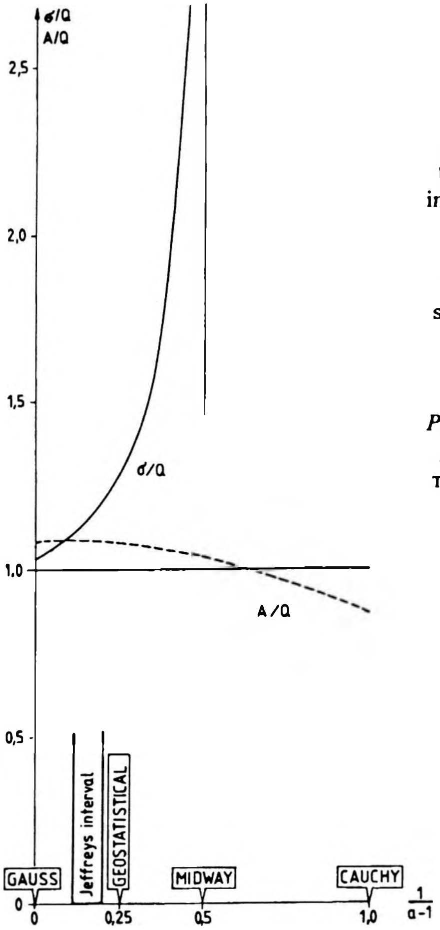

Fig. 6. Relation $A \approx Q$ holds for a large type interval; $\sigma \approx Q$ is valid only for the immediate neighbourhood of the Gaussian

6. ábra. Az $A \approx Q$ közelítő egyenlőség széles típustartományra érvényes; $\sigma \approx Q$ csak a Gauss-eloszlásra és közvetlen környezetére teljesül

Рис. 6. Приближенное равенство $A \approx Q$ действует для широкого диапазона типов; $\sigma \approx Q$ выполняется лишь для гауссовских распределений и их непосредственной близости

The σ/Q-curve of Fig. 6 shows that $\sigma \approx Q$ holds only for a surprisingly small type interval in the very neighbourhood of the Gaussian distribution; the problems shown in the Introduction are therefore to be understood without any difficulty. As

$$\sigma^2 = \begin{cases} \dfrac{1}{a-3} , & \text{if } a>3 \\ \infty , & \text{if } a\leq 3 \end{cases} \tag{54}$$

holds for f_a distributions, σ is infinite for a great variety of probability distribution types. In addition, it can be proved, that the asymptotic scatter of empirical scatters divided by the true value of σ is to be calculated according to the formula

$$A_\sigma/\sigma = \begin{cases} \dfrac{1}{2}\sqrt{3\dfrac{a-3}{a-5} - 1} , & \text{if } a>5 \\ \infty , & \text{if } a\leq 5 \end{cases} \tag{55}$$

It means that in the case of the very often occuring $a=5$ (see the density curve of the type-occurence in Fig. 19) the determination of the elements of the covariance matrix becomes problematic (at least from the in point of view of acceptable accuracy).

Let us look at some examples. But first of all a remark which belongs to all the examples shown in this Section: to tell the truth, it would really be necessary to discuss in detail an enormous number of variants but if we were to do this, there would be the danger of losing the clarity of the present paper. The most essential things, however, can be shown, too, if we restrict ourselves to Cauchy-distributed data: the classical covariance matrix is not even defined in this case and therefore these examples stress best of all the importance and necessity of the generalized covariance matrix. In some cases the sample will consist of Cauchy- as well as of Gauss-distributed data. The calculations were made on the ground of the generally applicable P-norm.

Curiously enough also the theoretical $q(w)$-curve of the L_2-results can be simply given if the sample contains only Cauchy-distributed data but n_a of them have a probable error of q_a and n_b are to be characterized by q_b:

$$q_0(w) = \frac{1}{n_a w + n_b (1-w)} \left\{ n_a w \cdot q_a + n_b (1-w) \cdot q_b \right\} . \tag{56}$$

The validity of Eq. (56) can easily be proven on the basis of the Cauchy distribution being a so-called stable one (see Subsection 2.2). The $q_0(w)$ function in Eq. (56) is evidently a monotonous one and therefore no minimum exists for $0<w<1$.

Fig. 7 shows the theoretical $q(w)$ and $Q(w)$-curves, respectively, as 0.7645 and 0.9674 times (see Eqs. (25) and (26)) of the $A_0(w)$-values calculated according to

$$A_0(w) = \frac{1}{n_a w + n_b(1-w)} \cdot \sqrt{n_a w^2 \cdot A_a^2 + n_b (1-w)^2 \cdot A_b^2} \ , \tag{57}$$

which is clearly a special variant of Eq. (52) for P-algorithms. (The numerical values of A obtained by using Eq. (47) are given for some distribution types in STEINER [1990], e.g., A=1.5 holds for the standard Cauchy distribution and A=1.0466 is valid for the standard Gaussian distribution. If the parameter of scale S differs from unity, A (being valid for the standard case) is to be multiplied by the actual value of S. The Monte Carlo results agree satisfactorily with the theoretical ones in the case of Fig. 7 although only a small sample was investigated (n_a=n_b=4). The same is true for the P-curve of *Fig. 8*; in this case samples contained data of Cauchy type as well as of Gaussian type. Consequently, the inverse of the generalized covariance matrix informs us adequately about the best weight w_{opt} to be used.

2. 2 *Generalization of the correlation matrix*

The elements of the classical correlation matrix ρ (see Eq. 8) are defined by Eqs. (4) and (5) and calculated on the ground of data pairs according to Eq. (6). These matrix elements, i.e., the correlation coefficients, are used popularly in practice (it is certain that one of the reasons for this is that $-1 \leq \rho \leq 1$ always holds), — although their definition do not make possible a plausible interpretation of this notion for appliers.

An obvious interpretation of ρ, however, can be simply given in the special case if ξ , η and ζ have equally standard Gaussian distribution ξ and ζ are independent and the relation

$$\eta = \rho \cdot \xi + \zeta \cdot \sqrt{1-\rho^2} \tag{58}$$

holds. Namely, it can be proven (see e.g. CRAMÉR [1946]) that in this case Eq. (5) results really in the correlation coefficient ρ having, according to Eq. (58), an immediate meaning: the random variable η 'contains' the random variable ξ to the extent of the proportionality factor ρ.

As Eq. (58) gives an obvious and simple connection of random variables, this relation should be regarded by our generalizing as a primary definition of a value which measures the closeness of the connection between random variables ξ and η. In the general case we shall denote this proportionality factor by r_{true}, — but how can Eq. (58) itself be generalized?

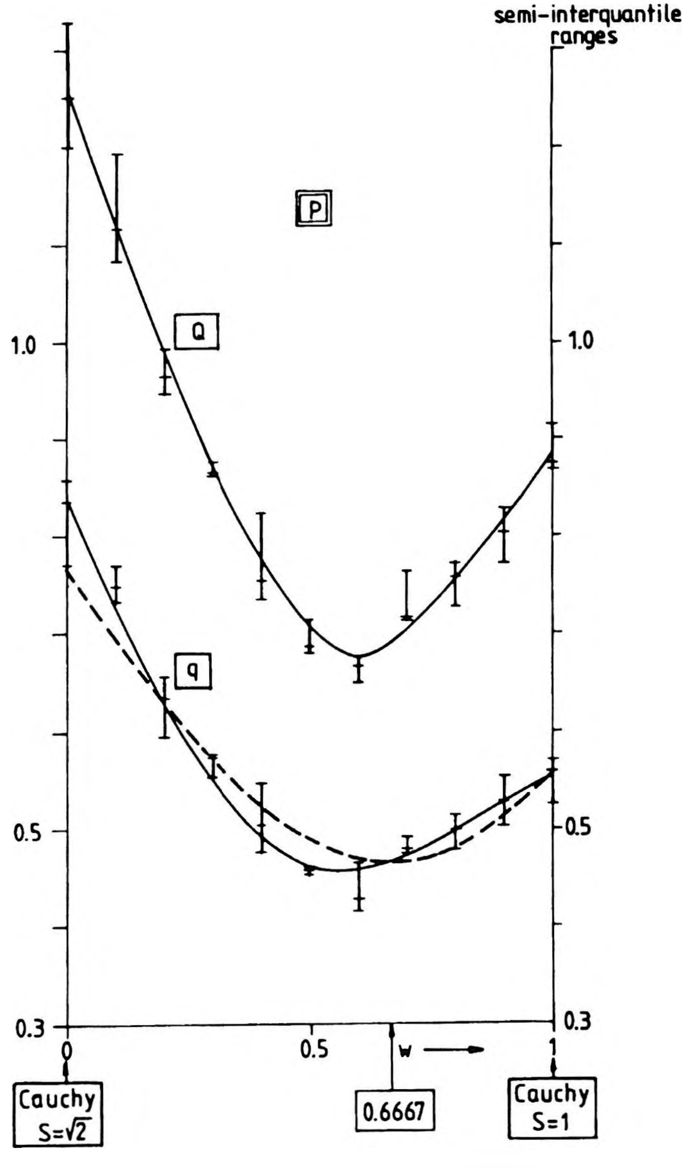

Fig. 7. Error curve of the results from the *P*-algorithm (n_a=n_b=4). The best choice of the weights corresponds to the generalized covariance matrix

7. ábra. *P*-algoritmussal nyert eredmények hibagörbéje (n_a=n_b=4). A súlyok optimális választása az általánosított kovarianciamátrixnak felel meg

Рис. 7. Кривая погрешностей результатов, полученных по алгорифму *P* (n_a=n_b=4). Оптимальный выбор весов отвечает обобщенной ковариационной матрице

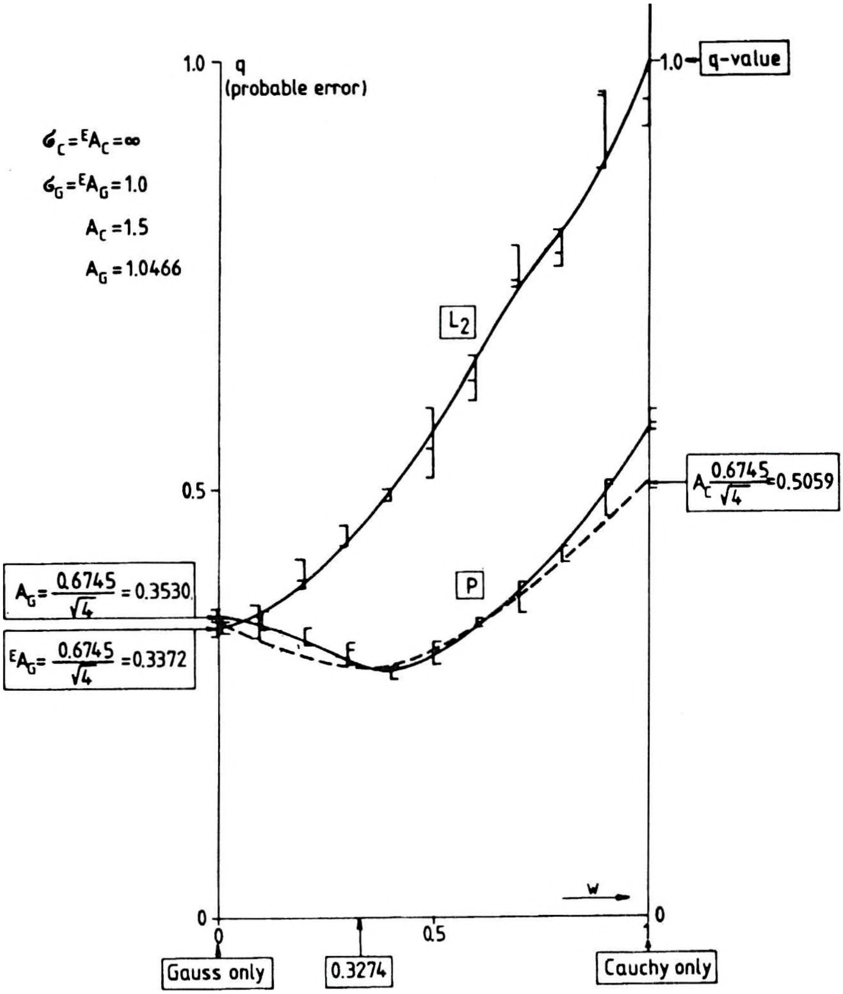

$$P:\ w_{opt} = \frac{1/A_C^2}{1/A_C^2 + 1/A_G^2} = \frac{1/1.5^2}{1/1.5^2 + 1/1.0466^2} = 0.3274$$

$$L_2:\ w_{opt} = \frac{1/{}^EA_C^2}{1/{}^EA_C^2 + 1/{}^EA_G^2} = 0$$

Fig. 8. Error curve of the results from the *P*-algorithm (n_a=4 data are Cauchy-distributed, n_b=4 are Gaussian). The best choice of the weights corresponds to the generalized covariance matrix

8. ábra. P-algoritmussal nyert eredmények hibagörbéje (n_a=4 adat Cauchy-, n_b=4 adat pedig Gauss-eloszlású). A súlyok optimális választása az általánosított kovarianciamátrixnak felel meg

Рис. 8. Кривая погрешностей результатов, полученных по альгорифму *P* (данные n_a=4 имеют распределение Коши, а данные n_b=4 гауссовское распределение). Оптимальный вибор весов отвечает обобщенной ковариационной матрице

In the first step the premise of the Gaussian distribution of the probability distributions should be given up. The supposition of the Gaussian type of all three random variables was convenient in respect of Eq. (58) because of the so-called stability of the Gaussian distributions: the sum of two Gaussian random variables is also Gaussian. There are, however, plenty of stable and symmetrical distributions besides the Gaussian, namely the types of the $f_\alpha(x)$-supermodel defined by

$$f_\alpha(x) = \frac{1}{\pi}\int_0^\infty \exp\left(-|t|^\alpha/\alpha\right) \cdot \cos(xt)\, \mathrm{d}t \qquad (0 < \alpha \leq 2) \tag{59}$$

(for more about this supermodel see in STEINER [1990]; $f_\alpha(x)$ is the Gaussian density function if $\alpha = 2$, and in the case of $\alpha = 1$ we get the Cauchy distribution). Our generalization is simple: α should have all its possible values, not only the value 2. In this case the following generalized version of Eq. (58) is needed:

$$\eta = r_{true} \cdot \xi + \zeta \cdot (1 - |r_{true}|^\alpha)^{1/\alpha} \tag{60}$$

(see Eq. (3) in HAJAGOS and STEINER [1989b]) and this corresponds to the following density function:

$$f_\alpha(x,y) = \frac{1}{(1-|r_{true}|^\alpha)^{1/\alpha}} \cdot f_\alpha(x) \cdot f_\alpha\left[\frac{y - r_{true} \cdot x}{(1-|r_{true}|^\alpha)^{1/\alpha}}\right] . \tag{61}$$

With $\alpha = 2$ this expression clearly gives the well known formula for the two-variable Gaussian distribution.

The f_α and f_a distributions are very similar, see e.g. *Fig*. 9, — but this close connection can also be demonstrated theoretically (based on the investigation of efficiencies, see again the just cited paper. The following empirical formula yields that value of α for a given type parameter *a*; in such cases f_α is most similar to f_a:

$$\alpha(a) = 2 - 0.92 \cdot \operatorname{arc\,tan} \frac{1.9}{a-1} , \tag{62}$$

see *Fig. 10*). Consequently, the two-variable $f_a(x,y)$ can be written as

$$f_a(x,y) = \frac{1}{(1-|r_{true}|^\alpha)^{1/\alpha}} \cdot f_a(x) \cdot f_a\left[\frac{y - r_{true} \cdot x}{(1-|r_{true}|^\alpha)^{1/\alpha}}\right] , \tag{63}$$

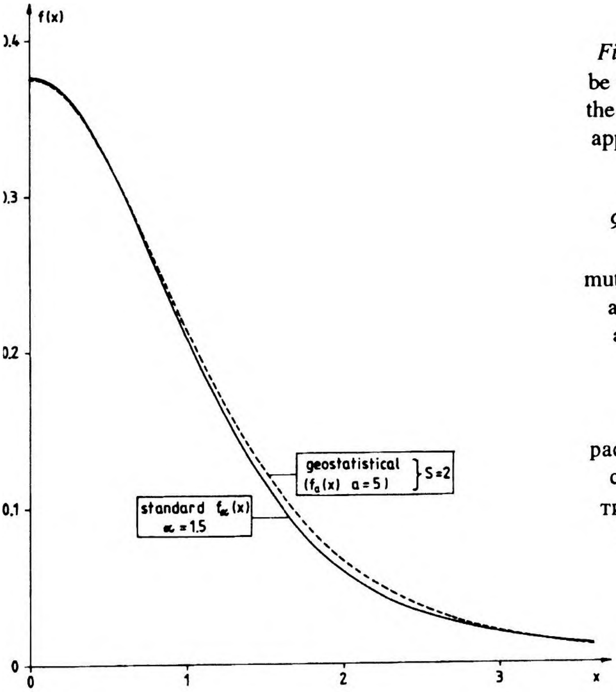

Fig. 9. Stable f_α distributions can be very similar to f_a distributions if the value of the α type parameter is appropriately chosen for the given value of **a**

9. ábra. A stabil f_α-eloszlások nagyfokú hasonlóságot mutathatnak az f_a-eloszlásokkal, ha az α típusparaméter értékét az adott **a**-értéknek megfelelően választjuk

Рис. 9. Стабильные f_α распределения весьма сходные с f_α распределениями, если типовой параметр α выбрать соответственно данному значению **a**

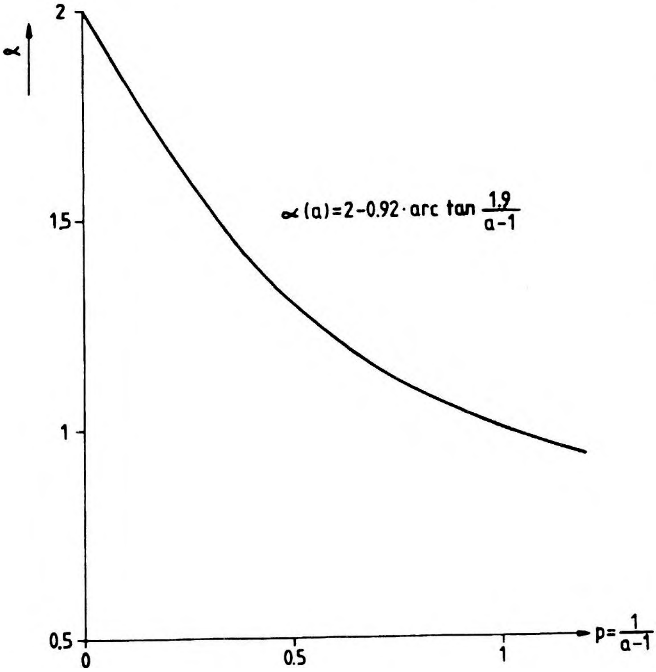

Fig. 10. Curve of the empirical α(*a*)-function

10. ábra Az empirikus α(*a*)-függvény görbéje

Рис.10. Кривая эмпирической функции α(*a*) where the α-value is defined by Eq. (62).

After the foregoing the generalized correlation matrix can be written as

$$r_{true} = \begin{pmatrix} 1 & r_{true;1,2} & \cdots & r_{true;1,n} \\ r_{true;2,1} & 1 & \cdots & r_{true;2,n} \\ \cdot & & & \cdot \\ r_{true;n,1} & & \cdots & 1 \end{pmatrix} \tag{64}$$

($r_{true;i,k}$ characterizes the closeness of the statistical connection between ξ_i and ξ_k). Nothing was said, however, till now about the determination of the $r_{true;i,k}$-values; this will be treated from the point of view of practice in Subsection 3.1.

To have some idea about the error committed if we regard the expression for ρ in Eq. (6) as an estimate of r_{true}, see the curves for different α-values in *Fig. 11* (reprinted from HAJAGOS and STEINER [1989b]). For $\alpha = 1.5$, which often occurs ρ is greater by nearly 0.1 for a large r_{true}-interval, and for $\alpha = 1$ the difference can be 0.25, too, — and this value is a

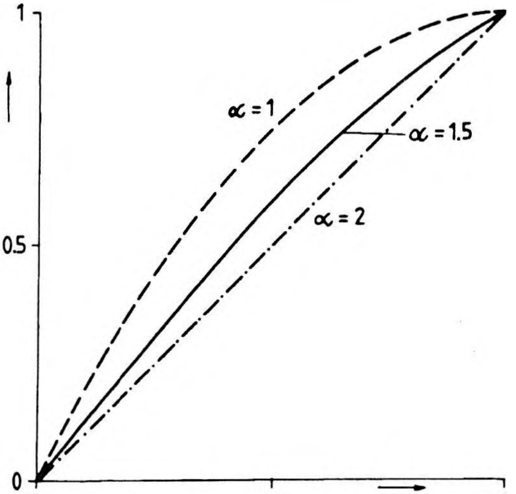

Fig. 11. Value of correlation coefficient ρ defined in classical statistics is systematically larger than r_{true} if the distributions in question are stable distributions characterized by $\alpha<2$ ($\alpha=2$ is the Gaussian case)

11. ábra. A klasszikus statisztika által definiált ρ korrelációs együttható szisztematikusan nagyobb, mint r_{true}, ha $\alpha<2$ ($\alpha=2$ esetén Gauss-eloszlással van dolgunk)

Рис. 11. Коэффициент корреляции ρ, дефинированный по классической статистике систематически выше, чем r_{true}, если $\alpha<2$. (В случае $\alpha=2$ имеем дело с гауссовским распределением) quarter of the whole $|r_{true}|$-range. No wonder that practicians mostly believe in the existence of any correlation only if ρ is greater (or even significantly greater) than 0.5 (it should not be forgotten that $\alpha=1$ means the Cauchy distribution type — and this type can be utilized for modeling the unavoidable outliers, too, in the case of error distributions originally having not such heavy flanks, see TARANTOLA [1987]).

2. 3 *Generalization of the covariance matrix*

The elements of the classical covariance matrix are to be written as $\rho_{ik}\cdot\sigma_i\cdot\sigma_k$, see Eq. (7). We have seen, however, that $r_{true;i,k}$ is the proper generalization of ρ_{ik}, on the one hand (see Subsection 2.2), and on the other hand, the asymptotic scatter ${}^gA_i$ can in every respect be regarded as the generalization of the scatter σ_i (see Subsection 2.1). The straightforward generalization of the covariance matrix results therefore in

$$
{}^g\mathbf{A} = \begin{bmatrix}
{}^gA_1^2 & r_{true;1,2}\cdot{}^gA_1\cdot{}^gA_2 & \cdots & r_{true;1,n}\cdot{}^gA_1\cdot{}^gA_n \\
r_{true;2,1}\cdot{}^gA_2\cdot{}^gA_1 & {}^gA_2^2 & & \\
\vdots & & & \vdots \\
\vdots & & \ddots & \vdots \\
r_{true;n,1}\cdot{}^gA_n\cdot{}^gA_1 & r_{true;n,2}\cdot{}^gA_n\cdot{}^gA_2 & \cdots & {}^gA_n^2
\end{bmatrix}; \quad (65)
$$

if all r_{true} are zero we get the already known form of ${}^g\mathbf{A}$ given in Eq. (39) for the case of independent random variables. If *P*-norm algorithms are used (i.e., most frequent values are calculated), the covariance matrix **A** clearly has the form

$$
\mathbf{A} = \begin{bmatrix}
A_1^2 & r_{true;1,2}\cdot A_1\cdot A_2 & \cdots & r_{true;1,n}\cdot A_1\cdot A_n \\
r_{true;2,1}\cdot A_2\cdot A_1 & A_2^2 & & \\
\vdots & & & \vdots \\
\vdots & & \ddots & \vdots \\
r_{true;n,1}\cdot A_n\cdot A_1 & r_{true;n,2}\cdot A_n\cdot A_2 & \cdots & A_n^2
\end{bmatrix} \quad (66)
$$

(this is, formally regarded, very nearly the same as Eq. (65): the only difference is that no *g*-indices figure in Eq. (66)).

The examples (*Figs. 12–18*) for showing the influence of various weighting and especially the a priori weighting according to A^{-1} in the case of P-algorithms demonstrate not only Monte Carlo results for small samples but also the corresponding theoretical curve, too. These curves were calculated according to

$$q(w) = \frac{0.6745}{n_a w + n_b (1-w)} \cdot \sqrt{n_a w^2 \cdot A_a^2 + n_b (1-w)^2 \cdot (1+r_{true}) A_b^2} \tag{67}$$

(this expression is clearly the analogue of Eq. (22) taking also Eq. (25) into consideration). Is was really unavoidable to show these empirical and theoretical $q(w)$-curves (the latter always with dashed line) for some situations to be able to draw important conclusions but the detailed discussion of the shown seven examples were superfluous. The reader will be satisfied in all cases with the agreement between the theoretically obtained (asymptotic) w_{opt}-value calculated on the ground of the corresponding A^{-1} which means in our simplified cases

$$w_{opt} = \frac{\frac{1}{A_a^2}}{\frac{1}{A_a^2} + \frac{1}{A_b^2 \cdot (1+r_{true})}}, \tag{68}$$

and the optimal **w** shown by the Monte Carlo results for small samples.

Departures between theoretical and Monte Carlo curves can be really significant if there are only three data (see the neighbourhood of $w=1$ in Figs. 13, 15, 16, 17) but minimum places coincide very well also in these cases. If four data are present the departures became insignificant; this was already known, however, on the basis of Figs. 7 and 8.

The error of an inversion is to be calculated also on the ground of the covariance matrix which is to be interpreted asymptotically. Therefore it is important to investigate the departures between the asymptotic and the Monte Carlo values of $q(w_{opt})$, too, but this question is not treated in the present paper in detail. If we remember, however, our train of thought concerning the customarily demanded accuracy of the errors (see the paragraph after Eq. (26)) and we also take into account Figs. 20 and 21 from the next Section, the differences between the asymptotic and the empirical $q(w_{opt})$-values can be regarded in all shown cases to be acceptable; in some cases the agreement is excellent.

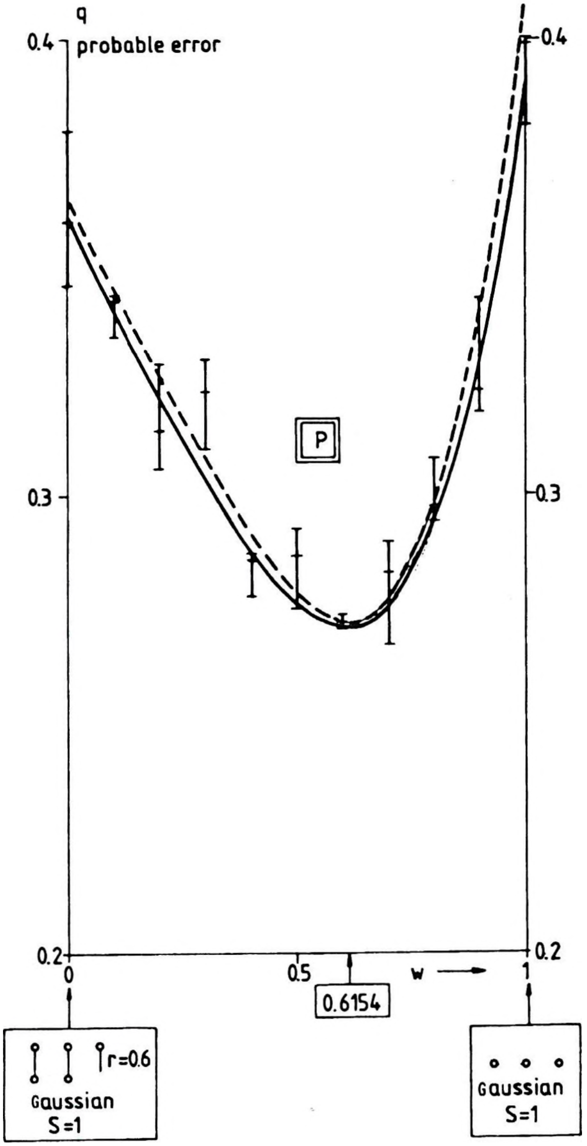

Fig. 12. Error curve of the results from the *P*-algorithm (Gauss-distributed data; n_a=3, n_b=6; r_{true}=0.6). The best choice of the weights corresponds to the generalized covariance matrix

12. ábra. *P*-algoritmussal nyert eredmények hibagörbéje (az adatok Gauss-eloszlásúak; n_a=3, n_b=6; r_{true}=0,6). A súlyok optimális választása az általánosított kovarianciamátrixnak felel meg

Рис.12. Кривые погрешности результатов, полученных альгорифмом *P* (данные имеют гауссовское распределение, n_a=3, n_b=6; r_{true}=0.6) Оптимальный выбор весов

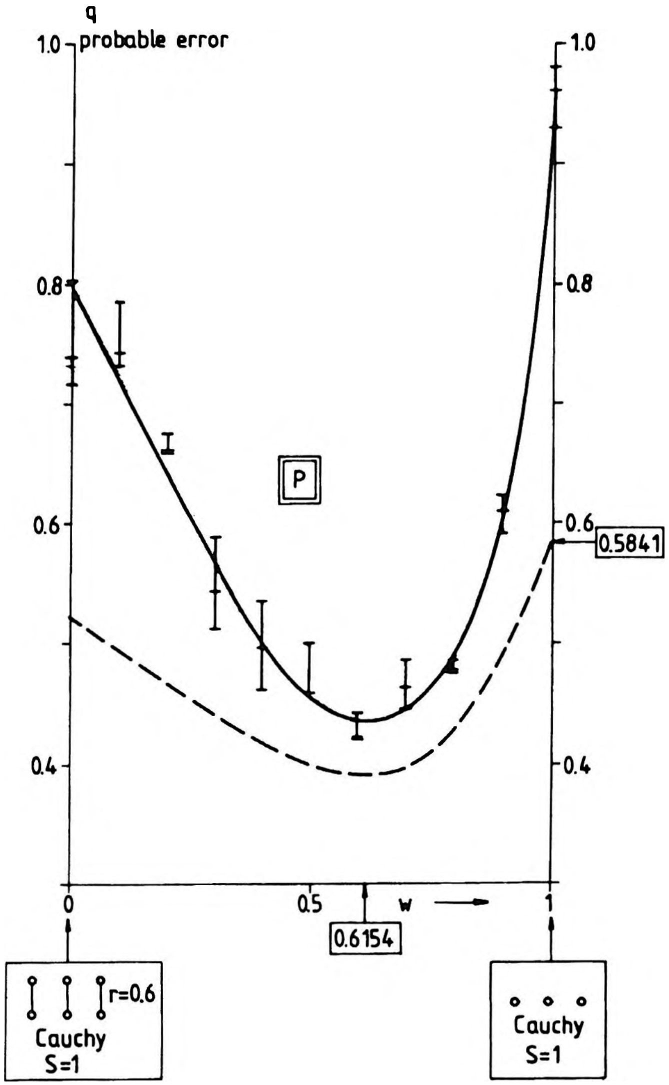

Fig. 13. Error curve of the results from the *P*-algorithm (n_a=3, n_b=6; r_{true}=0.6). The best choice of the weights correspontds to the generalized covariance matrix (the theoretical curve itself differs significantly on both sides)

13. ábra. P-algoritmussal nyert eredmények hibagörbéje (n_a=3, n_b=6; r_{true}=0,6). A súlyok optimális választása az általánosított kovarianciamátrixnak felel meg (noha az elméleti görbe mindkét széle szignifikáns eltérést mutat)

Рис.13. Кривые погрешности результатов, полученных альгорифмом *P* (n_a=3, n_b=6; r_{true}=0.6). Оптимальный выбор весов соответствует обобщенной ковариационной матрице (несмотря на то, что обе края теоретической кривой показывают расхождение)

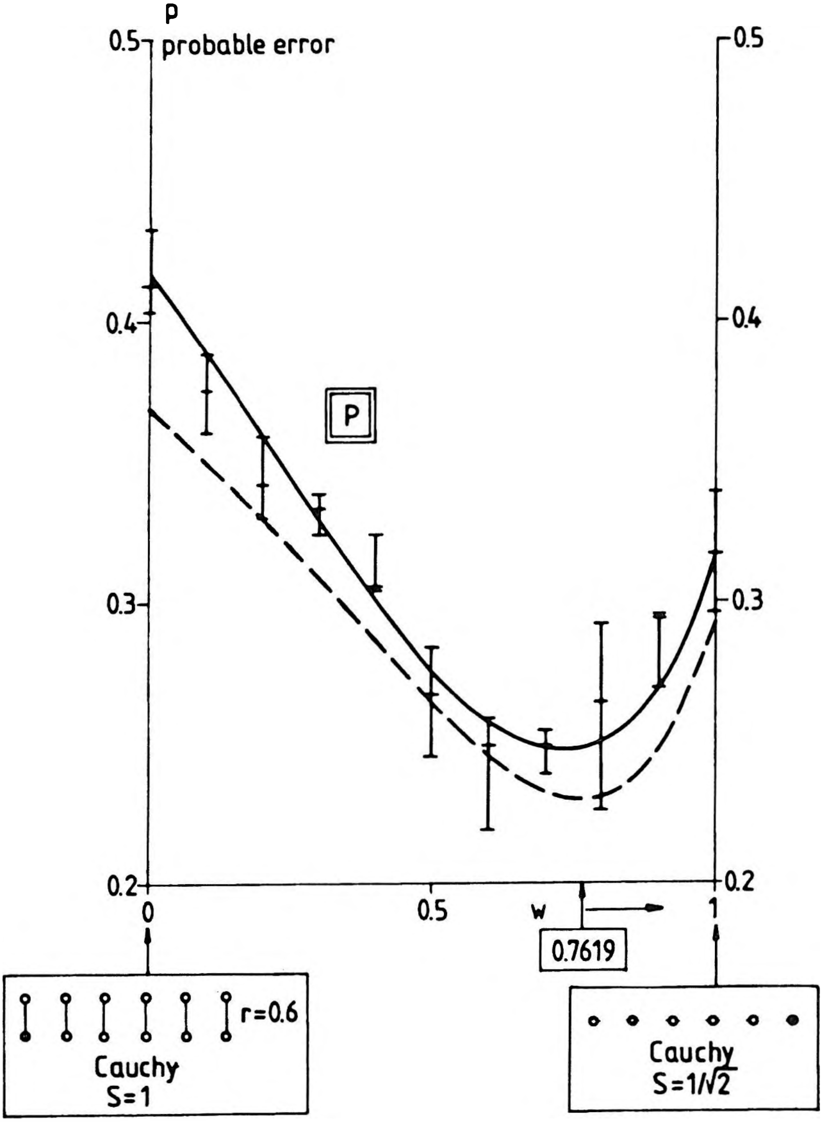

Fig. 14. Error curve of the results from the P-algorithm (n_a=6, n_b=12; r_{true}=0.6). The best choice of the weights corresponds to the generalized covariance matrix

14. ábra. P-algoritmussal nyert eredmények hibagörbéje (n_a=6, n_b=12; r_{true}=0,6). A súlyok optimális választása az általánosított kovarianciamátrixnak felel meg

Рис. 14. Кривые погрешности результатов, полученных алгорифмом P (n_a=6, n_b=12; r_{true}=0.6). Оптимальный выбор весов соответствует обобщенной ковариационной матрице

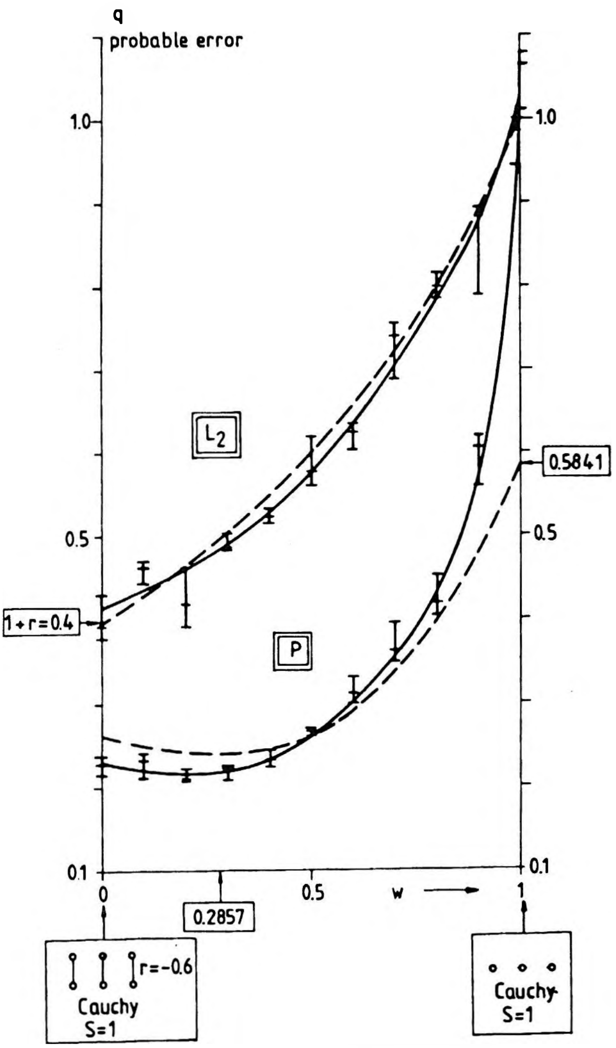

Fig. 15. Error curve of the results from the P-algorithm (n_a=3, n_b=6; r_{true}=-0.6). The best choice of the weights corresponds to the generalized covariance matrix. The error curve of the results from the classical L_2-algorithm is also shown

15. ábra. P-algoritmussal nyert eredmények hibagörbéje (n_a=3, n_b=6; r_{true}=-0,6). A súlyok optimális választása az általánosított kovarianciamátrixnak felel meg. A klasszikus statisztikai algoritmussal számított eredmények hibáit az L_2-vel jelölt folytonos görbe mutatja

Рис. 15. Кривые погрешности результатов, полученных альгорифмом P (n_a=3, n_b=6; r_{true}= - 0.6). Оптимальный выбор весов соответствует обобщенной ковариационной матрице. Погрешности результатов, полученных альгорифмом классической статистики показаны непрерывной кривой L_2

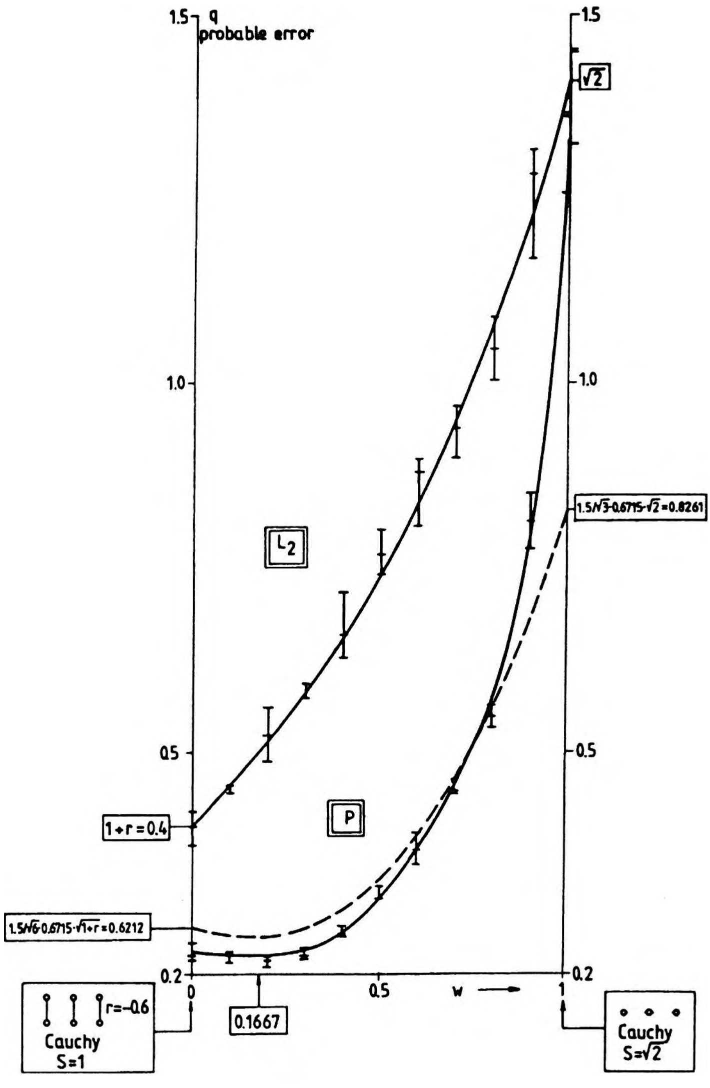

Fig. 16. Error curve of the results from the *P*-algorithm (n_a=3, n_b=6, r_{true}=-0.6; the scale parameters of the mother distributions are: $S_a=\sqrt{2}$ and S_b=1). The best choice of the weights corresponds to the generalized covariance matrix

16. ábra. *P*-algoritmussal nyert eredmények hibagörbéje (n_a=3, n_b=6, r_{true}=-0,6; az anyageloszlások skálaparaméterei: $S_a=\sqrt{2}$ és S_b=1) . A súlyok optimális választása az általánosított kovarianciamátrixnak felel meg

Рис.16. Кривые погрешности результатов, полученных альгорифмом *P* (n_a=3, n_b=6, r_{true}= - 0.6; параметры шкали распределения $S_a=\sqrt{2}$ and S_b =1). Оптимальный выбор весов соответствует обобщенной ковариационной матрице

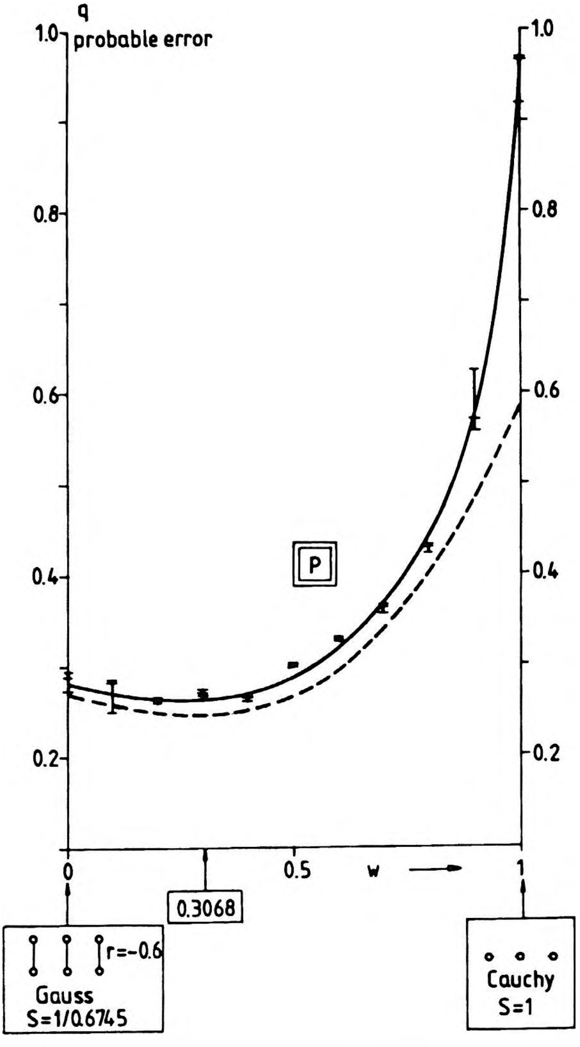

Fig. 17. Error curve of the results from the P-algorithm if n_a=3 data are Cauchy-distributed and independent, n_b=6 Gaussian data are pair-wise correlated: r_{true}=-0.6. (Both mother distributions have the same probable error.) The best choice of the weights corresponds to the generalized covariance matrix

17. ábra. P-algoritmussal nyert eredmények hibagörbéje, ha n_a=3 adat Cauchy-eloszlású és független, az n_b=6 db adat Gauss-eloszlású és páronként korrelált: r_{true}=-0,6. (A két anyaeloszlást azonos valószínű hiba jellemzi.) A súlyok optimális választása az általánosított kovarianciamátrixnak felel meg

Рис.17. Кривые погрешности результатов, полученных альгорифмом P, если данные n_a =3 независимые и отвечают распределению Коши, а n_b=6 данных имеют гауссовское распределение и попарно коррелированы : r_{true}= - 0.6. (Исходные распределения характеризуются такой же вероятностной погрешностью.) Оптимальный выбор весов соответствует обобщенной ковариационной матрице

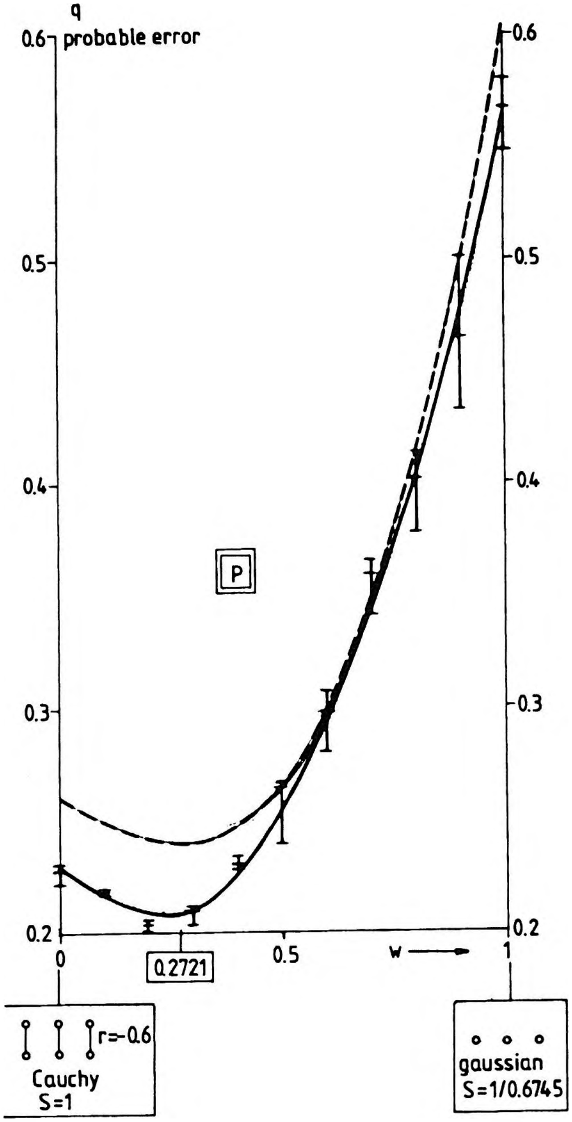

Fig. 18. Error curve of the results from the *P*-algorithm. The mother distribution types are changed, otherwise the samples were generated very similar to the case of Fig. 17. The best choice of the weights corresponds to the generalized covariance matrix

18. ábra. *P*-algoritmussal nyert eredmények hibagörbéje. A minták képzésénél az anyaeloszlás-típusokat megcseréltük, egyébként a 17. ábra felirata szerint jártunk el. A súlyok optimális választása az általánosított kovarianciamátrixnak felel meg

Рис. 18. Кривые погрешности результатов, полученных альгорифмом *P*. При задавании образцов тип исходных распределений поменяли, прочие условия те же, как на рис. 17. Оптимальный выбор весов соответствует обобщенной ковариационной матрице

3. Robustification

In Section 2 the covariance matrix was always regarded — as is usual — as 'a priori' given. In practice, however, the expression 'a priori' generally means nothing more than that these matrix elements were determined at an earlier stage of the work. In this Section we treat how these determinations are performed.

3.1 Robustification of the correlation matrix

In the literature of robust statistics it is customary to make robustifications of ad hoc type; this can be sanctioned by practice even if there is no satisfactory theoretical background. Let us now make such robustification of the formulae in Eqs. (5) and (6), forgetting for a moment the results of Section 2. Denoting the robustified ρ_{xy} by r_{xy}, our definitions are the following:

$$r_{xy} = \frac{\int\limits_{-\infty}^{\infty}\int\limits_{-\infty}^{\infty} [s(x)\cdot(x-M_x)]\cdot[s(y)\cdot(y-M_y)]\cdot f(x,y)\,\mathrm{d}x\mathrm{d}y}{\sqrt{\int\limits_{-\infty}^{\infty} s^2(x)\cdot(x-M_x)^2\cdot f(x)\,\mathrm{d}x}\cdot\sqrt{\int\limits_{-\infty}^{\infty} s^2(y)\cdot(y-M_y)^2\cdot f(y)\,\mathrm{d}y}} \tag{69}$$

if *f(x,y)* is known. If data-pairs are given,

$$r_{xy} = \frac{\sum\limits_{i=1}^{n} [s(x_i)\cdot(x_i-M_x)]\cdot[s(y_i)\cdot(y_i-M_y)]}{\sqrt{\sum\limits_{i=1}^{n} s^2(x_i)\cdot(x_i-M_x)^2}\cdot\sqrt{\sum\limits_{i=1}^{n} s^2(y_i)\cdot(y_i-M_y)^2}}\,; \tag{70}$$

the *s*-values are calculated according to Eq.(45) with M_x and ε_x in the case of *s(x)* and with M_y and ε_y in the case of *s(y)*.

The question rightfully arises whether the r_{xy} values, calculated on the ground of Eq. (69), really do not differ significantly from the r_{true}-values defined in Subsection 2.2. As practical cases can be well modelled by f_a-distributions, calculations for checking purposes were made for some values of the type parameter **a**. (By choosing these values, we also took into account the probability density function of the occurrence of different **a**-values in *Fig. 19*; see STEINER [1990]). After this choice, the *f(x,y)* in

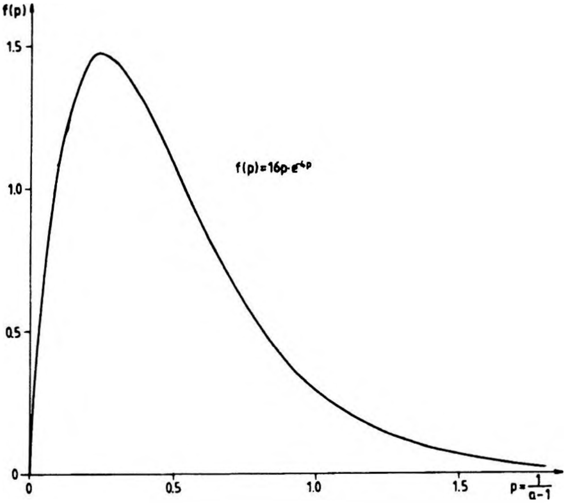

Fig. 19. Density function modelling the occurrence probabilities of different probability distribution type intervals of the $f_a(x)$-supermodel
19. ábra. Sűrűségfüggvény, amely az $f_a(x)$-szupermodell különböző valószínűségeloszlás típus-intervallumainak előfordulási valószínűségét modellezi
Рис. 19. Функция плотности, моделлирующая вероятность наблюдения разных интерваллов типа распределения вероятности супермоделли $f_a(x)$

Eq. (69) was taken according to Eq. (63); *Table I.* shows the differences $(r_{xy}-r_{true})$.

The maximum difference is 0.071 (see the row for the Cauchy distribution); if $a \geq 3$ can be supposed in an actual case, all absolute differences are less than 0.05.

These differences (of the character of bias) can be neglected by comparison with the expected statistical fluctuations. To have some idea about the measure of the latter; for $n=100$, pairs of data (of different probability distribution type) were generated according to Eqs. (60) and (62) in the first step; on the basis of these data-pairs r_{xy}-values were calculated according to Eq. (70) (for comparison the ρ_{xy} values were also determined, see Eq. (6)). This procedure was repeated $N=200$ times for each type investigated, consequently the interquartile- (full line), the intersextile- (dashed line) and the whole range (thin line) of the data were easy to construct (see *Fig. 20* where also the medians were indicated). The shifts correspond to the already known bias (see Table I) being in general less than the probable error even in the investigated case of $n=100$. (This statement does not hold for the values of ρ_{xy},— except the very classical but seldom if ever occuring Gaussian distribution.) A further consequence can be made on the basis of Fig. 20: the statistical fluctuation of r_{xy} is nearly

r_{true} =	0	0.1	0.2	0.3	0.4	0.5	0.6	0.7	0.8	0.9	1
Gauss ($a \to \infty$)	0	-0.008	-0.016	-0.023	-0.029	-0.032	-0.035	-0.033	-0.028	-0.017	0
a=10 } Jeffreys-interval	0	-0.006	-0.010	-0.014	-0.016	-0.017	-0.016	-0.014	-0.009	-0.004	0
a=6 }	0	-0.002	-0.003	-0.003	-0.003	-0.002	0	0.002	0.005	0.007	0
geostatistical (a=5)	0	0	0.001	0.003	0.005	0.007	0.009	0.011	0.013	0.012	0
midway (a=3)	0	0.011	0.023	0.033	0.041	0.047	0.049	0.048	0.043	0.026	0
Cauchy (a=2)	0	0.029	0.050	0.064	0.070	0.071	0.067	0.057	0.041	0.029	0

Table I. The differences $(r_{xy}-r_{true})$ for different values of r_{true} and for various probability distribution types

I. táblázat. Az $(r_{xy}-r_{true})$ különbségek r_{true} különböző értékeire és néhány valószínűségeloszlástípusra

Табл. I. Разницы $(r_{xy}-r_{true})$ для разных значений r_{true} и при изменении типа распределения вероятности

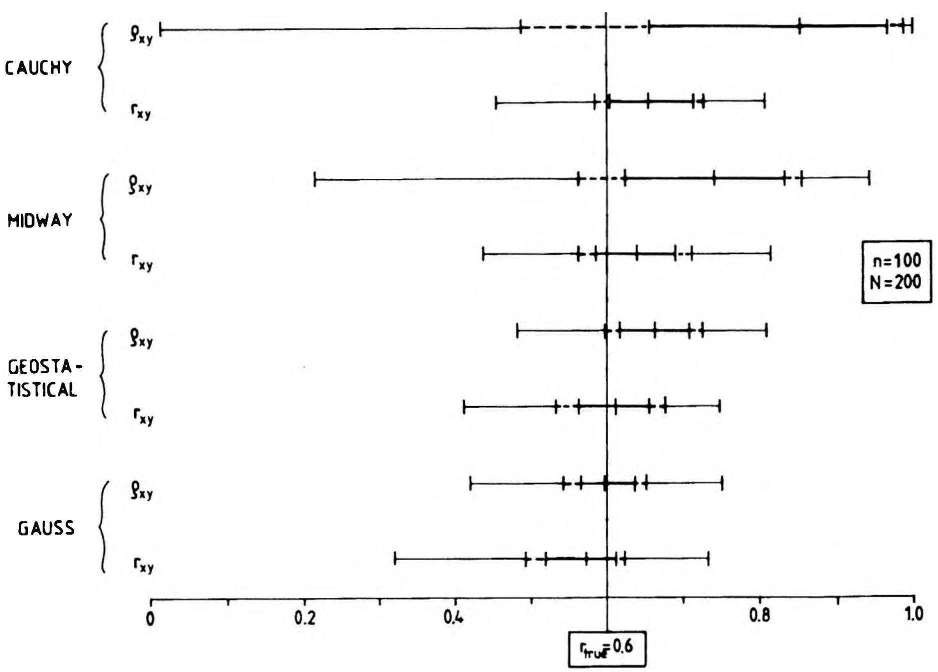

Fig. 20. Statistical fluctuatuions of the r_{xy} - and ρ_{xy}-values in the case of n=100

20. ábra. Az r_{xy}- és ρ_{xy}-értékek statisztikus ingadozása n=100 esetén

Рис. 20. Статистическое колебание значений r_{xy} и ρ_{xy} при n=100 independent of the distribution type; on the contrary, that of ρ_{xy} strongly depends on it and, in addition, we can state that the measure of the statistical fluctuation is also in itself fully unacceptable in the case of the Cauchy distribution (a similar statement characterizes the midway distribution), to say nothing about the great shifts (obtained in full agreement with Fig. 11, see e.g. curve '$\alpha=1$').

Concerning statistical fluctuations it is perhaps not superfluous to reprint two figures from CRAMÉR [1946] (see *Fig. 21*): in the frequently occuring cases of n=50 and n=10 the density functions of the ρ_{xy}-values show that unexpectedly large statistical errors occur even in the least problematic case: if the data are Gauss-distributed; this is closely linked with the fact that any kind of correlaton coefficient is characteristic of a *two-varibale* distribution. It can be stated as a conclusion that *the statistical fluctuation of* ρ_{xy} *in the very negihbourhood of the Gaussian as well as that of the* r_{xy}*-values in a broad type interval is significantly greater* at sample sizes used in the overwhelming majority of cases *than the bias of the* r_{xy}*-values.* Consequently, *the robustified correlation matrix defined by*

$$\boldsymbol{r} = \begin{pmatrix} 1 & r_{1,2} & r_{1,3} & \cdots & r_{1,n} \\ r_{2,1} & 1 & r_{2,3} & \cdots & r_{2,n} \\ \cdot & & & & \cdot \\ \cdot & & & & \cdot \\ r_{n,1} & & \cdots & \cdots & 1 \end{pmatrix} \tag{71}$$

can be regarded as a satisfactory approximation of the generalized correlation matrix $\boldsymbol{r}_{true}$. As for the computing techniques: the calculation of r_{xy} organically and simply joins with the basic algorithms of the most frequent value procedures (no special programs are needed).

3.2 *Robustification of the covariance matrix*

The meaning of the word 'robust' involves not only the applicability on a broad type interval but often the resistance, i.e., the insensitivity to outliers, too. In actual fact, the s-functions figuring in Eqs. (69) and (70) (i.e., in the formulae of the robust correlation coefficient) guarantees the resistance, too.

The s-function, however, is a basic function of the most frequent value calculations, and if we intend to robustify the scatter by means of this function, in a self-consistent way we can only set the aim that the A_i-values should be approximated by the robustified scatters.

A possible robustified form of the scatter is the following:

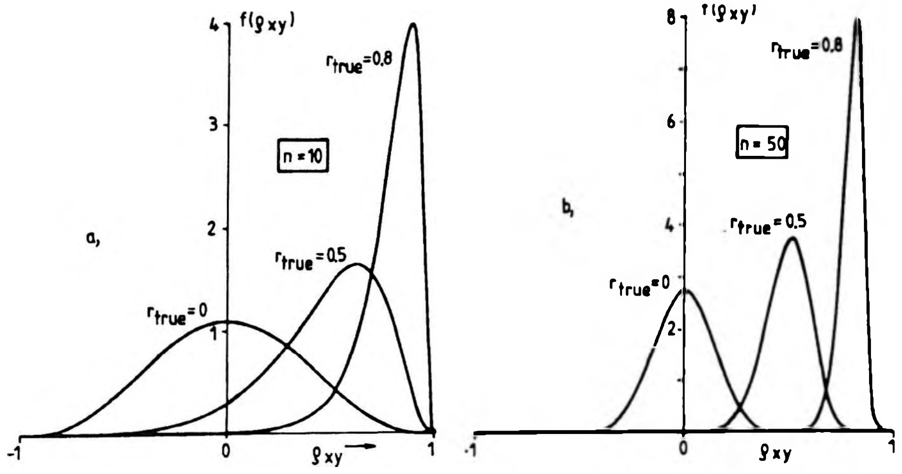

Fig. 21. Density functions of ρ_{xy} (from CRAMÉR [1946]) for $n=10$ and $n=50$ if the random variables have Gaussian distribution

21. ábra. A ρ_{xy} sűrűségfüggvényei Gauss-eloszlású valószínűségi változók esetén, ha az adatpárok száma $n=10$ illetve $n=50$

Рис. 21. Кривые плотности ρ_{xy} для вероятностных переменных с гауссовским распределением, если количество пар данных $n=10$, $n=50$

$$\bar{A}=\sqrt{\frac{9}{5}\int_{-\infty}^{\infty} s(x)\cdot(x-M)^2 f(x)\,\mathrm{d}x}\ ; \qquad (72)$$

its estimate is clearly

$$\bar{A}=\sqrt{\frac{9}{5n}\sum_{i=1}^{n} s(x_i)\cdot(x_i-M)^2}\ . \qquad (73)$$

The notation $\bar{A}$ anticipates that $\bar{A}\approx A$ is valid (it is clear that a notation $\bar{\sigma}$ would equally be justifiable). *Table II.* gives the values A and $\bar{A}$ for some probability distribution types and the departures, too (in per cent).

	A	Ā	100.(Ā-A)/A
Gauss	1.0466	1.0369	-0.93 %
a=10	0.3694	0.3666	-0.76 %
a= 6	0.5173	0.5150	-0.44 %
geostatistical	0.5917	0.5904	-0.22 %
midway	0.9236	0.9350	+1.23 %
Cauchy	1.5000	1.5492	+3.28 %

As the fulfilment of $\bar{A} \approx A$ is satisfactory, the robustified covariance matrix $\bar{\bar{A}}$ (which gives nearly $\bar{A}$, see Eq. (66)) can be written as follows:

$$\bar{\bar{A}} = \begin{pmatrix} \bar{A}_1^2 & r_{1,2}\cdot\bar{A}_1\cdot\bar{A}_2 & \cdots & r_{1,n}\cdot\bar{A}_1\cdot\bar{A}_n \\ r_{2,1}\cdot\bar{A}_2\cdot\bar{A}_1 & \bar{A}_2^2 & & \\ \cdot & & & \cdot \\ \cdot & & & \cdot \\ r_{n,1}\cdot\bar{A}_n\cdot\bar{A}_1 & r_{n,2}\cdot\bar{A}_n\cdot\bar{A}_2 & & \bar{A}_n^2 \end{pmatrix} . \qquad (74)$$

Thorough investigation of the determination errors of the matrix elements is beyond the scope of the present article (e.g., whether the method given in HAJAGOS and STEINER [1989a] for extraordinary outliers is to be applied or not). Such investigations should preferably be made parallely with the study of practical cases.

The authors are indebted to L. FERENCZY, consultant (Geophysical Exploration Co., Budapest) for having initiated this work, and to their colleagues L. CSERNYÁK, Á. GYULAI and T. ORMOS for fruitful discussions .

REFERENCES

CRAMÉR H. 1946: Mathematical Methods of Statistics. Princeton University Press, Princenton

HAJAGOS B. 1982: Der häufigste Wert, als eine Abschätzung von minimalem Informationsverlust etc. Publications of the Technical University for Heavy Industry Series A Mining **37**, 1-2, pp. 95-114

HAJAGOS B. 1985: Die verallgemeinerten Student-scken t-Verteilungen und die häufigsten Werte. Publications of the Technical University for Heavy Industry Series A Mining **40**, 1-4, pp. 225-238

HAJAGOS B., STEINER F. 1989a: Methods to increase the resistance etc. Acta Geodaetica, Geophysica et Montanistica Acad. Sci. Hung. **24**, 3-4, pp. 289-307

HAJAGOS, B., STEINER F. 1989b: Measure of the linear dependence. Acta Geodaetica, Geophysica et Montanistica Acad. Sci. Hung. **24**, 3-4, pp. 417-439

HUBER P. J. 1981: Robust Statistics. Wiley, New York

INMAN J. R. 1975: Resistivity inversion with ridge regression. Geophysics, **40**, 5, pp. 790-797

STEINER F. 1988: Most frequent value procedures. Geophysical Transactions, **34**, 2-3, pp. 139-260

STEINER F. 1990: Foundations of Geostatistics (in Hungarian). Tankönyvkiadó, Budapest, 363 p.

STEINER F. (Ed.) 1991: The Most Frequent Value. Akadémiai Kiadó, Budapest, 315 p.

TARANTOLA A. 1987: Inverse Problem Theory. Elsevier, Amsterdam

A KOVARIANCIAMÁTRIX ÁLTALANOSÍTÁSA ÉS ROBUSZTIFIKÁLÁSA

HAJAGOS Béla és STEINER Ferenc

A dolgozat első része az egyszerű szemléltethetőség érdekében néhány elkerülhetetlen egyszerűsítést vezet be. Ezután a klasszikus statisztika kovarianciamátrixának inverzével való súlyozás optimális voltát mutatja meg a cikk Gauss-eloszlású hibákra, ugyanakkor példákkal hívja fel a figyelmet arra, hogy ettől eltérő hibaeloszlásoknál, kis mintaelemszám esetén, az optimális súlyozást nem okvetlenül ez a megoldás szolgáltatja.

A második rész a kovarianciamátrix általánosított, az alkalmazott statisztikai algoritmusnak megfelelő alakját definiálja; példákat zömmel P-algorimust alkalmazó eljárásokra, azaz súlyozott leggyakoribb érték-számításokra mutat be. Kiderült, hogy az általánosított kovarianciamátrix inverze kis mintaelemszámok esetén is alkalmazható, ha a leggyakoribb értékek szerinti algoritmusokkal dolgozunk.

A harmadik rész ezen általánosított kovarianciamátrixot a klasszikus eset robusztifikálásával javasolja egyszerűség kedvéért meghatározni. Ez a meghatározás ui. számítástechnikai szempontból szorosan illeszkedik a leggyakoribb érték szerinti számítások alapvető algoritmusaihoz.

ОБОБЩЕНИЕ И РОБУСТИФИКАЦИЯ КОВАРИАЦИОННОЙ МАТРИЦЫ

Бела ХАЯГОШ, Ференц ШТЕИНЕР

В первой части статьи вводятся некоторые необходимые для наглядности упрощения. После этого показывается оптимальность взвешивания обратной ковариационной матрицы классической статистики для погрешностей Гауссовского распределения, и обращается внимание на то, что при отличающемся от Гауссовского распределение погрешностей и при небольшом количестве образцов оптимальное взвешивание получается необязательно данным способом.

Во второй части дается определение обобщенного, подходящего для прминенного статистического альгорифма вид ковариационной матрицы. Примеры показываются прежде всего для способов, применяющих альгорифм P, то есть показываются расчеты взвешенной наиболее частой величины. Выявилось, что обратнуаю матрицу обобщенной ковариационной можно применять и в случае небольшого количества образцов, если работать с альгорифмами по наиболее частым величинам. В третьей части рекомендуется для простаты определить эти обобщенные ковариационные матрицы при робустификации классической, ввиду того, что такое определение непосредственно связано с основными альгорифмами расчетов по наиболее частым величинам.

GEOPHYSICAL TRANSACTIONS 1992
Vol. 37. No. 2-3. pp. 159-176

FAST COMPUTING OF TRANSIENT ELECTROMAGNETIC FIELD ON THE SURFACE OF A LAYERED HALF-SPACE

Ernő PRÁCSER*

Time domain electromagnetic fields can be computed by the spectral technique, viz. using the inverse Fourier-transform applied to frequency domain, or by solving Maxwell's equations in the time domain. For a layered half-space and for the total time domain, accurate computations for the latter method are very time consuming because of the presence of a partial differential equation in the derivation of the formulae determining the transient field that cannot be solved by analytical functions. The numerical solution of partial differential equations is very time consuming. On the other hand, the differential equation that arises in the frequency domain can be expressed by analytical functions. If we do not require an accurate solution to the total time domain, then the solution of the partial differential equation occurring in the time domain can be computed by analytical functions, too. The paper discusses a case which is valid for a non-conducting basement and is based on an asymptotic solution that is valid at late times.

Keywords: transient methods, electomagnetic field, half-space, dipole, computer programs

1. Introduction

In most cases the interpretation of the transient and other electromagnetic measurements is based on assuming a layered half-space at the site of the measurement and we try to determine the parameters of the half-space, from which a conclusion can be drawn on the geoelectric structure. In order to determine the layer parameters that belong to the measured curves a direct problem solving program is needed for computing the theoretical curves from optional layer parameters. Though in the case of the transient method there are many computational methods for solving the problem,

---

* ELGI, Budapest, XIV. Columbus u. 17-23.
Manuscript received: 15 July, 1991

none of them is so fast that it would not be worth the effort of increasing the speed of computation. The speed is especially important when applying a curve computating program for curve fitting. On a 12 MHz IBM PC/AT equipped with a coprocessor the computation of the direct problem by the spectral method takes about 10 s/layer and it gives accurate results at early and at late times [PRÁCSER 1986]. The transient electromagnetic field takes the form of a Hankel transform of a kernel function as a result of the solution of the Maxwell's equations in the time domain. This kernel function is the solution of a partial differential equation that can be solved by the finite difference method [GOLDMAN 1983]. Computation based on this theory is much slower than the spectral technique. If we accept that for the early times we do not get accurate transient field values then the kernel function in the time domain can be generated in the form of a series expansion. In that case the computation requires much less time than by the finite difference method. In the Soviet literature we find that this method used to be applied to two- and three-layered halfspaces [TIKHONOV, SKUGAREVSKAYA 1950]. At late times even the first term of the series gives an accurate result; at early times we have to take more terms into consideration. Even though this method was known as far back as 1950, at that stage of computational techniques it probably could not be applied in practice and once computers had come into general use in geophysics the spectral method was preferred in transient calculus. In the following we show the computation based on the series expansion of the kernel function for an n-layered model.

2. Transient field of an electric dipole at the surface of a layered half-space

Let us examine the electric dipole on the surface of a layered half-space when the current flowing in a conductor of elementary length is turned off at time t=0 and the effect of the displacement current is negligible. The induced electromagnetic field is defined by Maxwell's equations:

$$\begin{aligned} &\operatorname{rot} \vec{H} = \sigma \vec{E} + \vec{J} \qquad && \operatorname{div} \vec{H} = 0 \\ &\operatorname{rot} \vec{E} = -\mu \frac{\partial}{\partial t} \vec{H} && \operatorname{div} \vec{E} = 0 \end{aligned} \tag{1}$$

where:

$\vec{E}$ — electric field vector

$\vec{H}$ — magnetic field vector

μ — magnetic susceptibility

t — time

$\vec{J} = (J_x, 0, 0), \quad J_x = \dfrac{I(t)\, dl\, \delta(z)\, \delta(r)}{2\pi r}$ — exciting current

r — length between the dipole and the measuring point

$I(t) = \begin{cases} I_0 & t \le 0 \\ 0 & t > 0 \end{cases}$ — current flowing in the dipole

dl — length of the electromagnetic dipole

$\delta(z)$, $\delta(r)$ — Dirac-delta functions

σ — conductivity function depending only on the z coordinate that is defined as follows:

$$\sigma(z) = \begin{cases} 0 & z \ge z_0 = 0 \\ \sigma_j & z_{j-1} > z > z_j \qquad j = 1, \ldots, n-1 \\ \sigma_n = 0 & z < z_{n-1} \end{cases}$$

z_j — coordinates of the layer boundaries

n — number of layers

We shall briefly discuss the most important steps of the derivation of Eq. (1) that defines the transient field. As can be seen from the definition of σ we deal only with that case when the conductivity of the n-th layer is zero. One of the disadvantages of the computation based on the theory in question is that the n-th layer has to be a non-conductor or an ideal conductor. Here we discuss only the case of $\sigma_n = 0$ because it has much greater importance in practice than the case of $\sigma_n = \infty$. With the spectral technique there is no need for such a restriction. We start to solve the system of equations (1) in the usual way by introducing the $\vec{A}$ vector potential.

$$\vec{H} = \operatorname{rot} \vec{A}, \qquad \vec{A} = (A_x, 0, A_z) \tag{2}$$

The $\vec{A}$ vector potential, as can be derived from Maxwell's equations, satisfies the following partial differential equation:

$$\vec{A} - \mu\sigma \frac{\partial}{\partial t} \vec{A} = -\vec{J} \tag{3}$$

Bearing in mind that in most cases in transient measurement only the vertical component of the time derivative of the magnetic field vector is measured it is enough to determine the horizontal component of the vector potential because H_z does not depend on A_z (Eq. 2). From Eq. (3), written in cylindrical coordinates, the integral representation of A_x can be derived by the separation of variables:

$$A_x = c \int_0^\infty J_0(\lambda r)\, X(\lambda,z,t)\, \mathrm{d}\lambda$$

where:

J_0 — Bessel function of the first kind, zero order

$X(\lambda,z,t)$ — kernel function in time domain

Constant c can be obtained if we compare the magnetic field of an electric dipole in vacuum, expressed by vector potential, with the law of Biot-Savart, by which we get:

$$c = \frac{I_0\, dl}{4\pi}$$

So the formula defining the x component of the vector potential is:

$$A_x = \frac{I_0\, dl}{4\pi} \int_0^\infty J_0(\lambda r)\, X(\lambda,z,t)\, \mathrm{d}\lambda \tag{4}$$

3. Determination of the kernel function $X(\lambda,z,t)$

From Eq. (3) it follows that the $X(\lambda,z,t,)$ kernel function satisfies the following partial differential equation:

$$\frac{\partial^2 X(\lambda,z,t)}{\partial z^2} - \lambda^2 X(\lambda,z,t) = \mu\sigma \frac{\partial}{\partial t} X(\lambda,z,t) \tag{5}$$

For the uniqueness of Eq. (5) it is necessary to satisfy certain boundary conditions. The electromagnetic components and their time derivatives have a continuous transition through layer boundaries. For $t > 0$ it is valid for the kernel function $X(\lambda,z,t)$ and for its time derivatives too. If we take it into consideration that for $z > z_0$ and $z < z_{n-1}$ the conductivity of the medium is equal to zero then from Eq. (5) it follows that the kernel function $X(\lambda,z,t)$ has the form of $c_0 e^{-\lambda z}$ and $c_n e^{\lambda z}$ where c_0 and c_n are constants. So at the uppermost and at the lowest layer boundaries Eq. (5) has to be complemented with the following boundary conditions:

$$\frac{\partial X(\lambda,z,t)}{\partial z} + \lambda\, X(\lambda,z,t) = 0 \qquad z = z_0 \tag{6a}$$

$$\frac{\partial X(\lambda,z,t)}{\partial z} - \lambda\, X(\lambda,z,t) = 0 \qquad z = z_{n-1} \tag{6b}$$

For $t \leq 0$ current flows at a constant I_0 current intensity, viz. the time derivative is equal to zero in Eq. (5). Because of this the A_x component of the vector potential is the same as it should be in a vacuum from which we get the boundary condition at t=0:

$$X(\lambda,z,t) = e^{\lambda z} \qquad t = 0,\ \ z < 0 \tag{7}$$

Partial differential equation (5) defining the kernel function $X(\lambda,z,t)$ can be solved by the finite difference method, too [GOLDMAN 1983] but this method is very time consuming. Here we would comment that the frequency domain form of Eq. (5) will be simpler because instead of time derivation there is conjunction $i\omega$, where $i = \sqrt{-1}$ is the imaginary unit and ω is the radian frequency. So the exact solution can be expressed by a linear combination of exponential functions.

In this paper the solution of Eq. (5) is sought by separating the variables in the form of an infinite series:

$$X(\lambda,z,t) = \sum_{k=1}^{\infty} \beta_{k,j}(\lambda,z)\, \alpha_{k,j}(t) \qquad j = 1,\ldots, n-1 \tag{8}$$

If the expansion in series (8) of kernel function $X(\lambda,z,t)$ is substituted into Eq. (5) we get the differential equation defining functions $\beta_{k,j}$ and $\alpha_{k,j}$ in the j-th layer:

$$\frac{\dfrac{\partial^2}{\partial z^2}\beta_{k,j}(\lambda,z)}{\beta_{k,j}(\lambda,z)} - \lambda^2 = -\nu_{k,j} \tag{9}$$

$$\mu\sigma_j \frac{\dfrac{\partial}{\partial t}\alpha_{k,j}(t)}{\alpha_{k,j}(t)} = -\nu_{k,j} \tag{10}$$

The solution of Eq. (10) is:

$$\alpha_{k,j}(t) = c_k\, e^{-\frac{\nu_{k,j}}{\mu\sigma_j}t} \tag{11}$$

From the continuity of functions $\alpha_{k,j}$ in direction z it follows that the exponents have to be independent of j. Because of this the $\nu_{k,j}$ separational constants can be determined as a function of conductivity:

$$\nu_{k,j} = w_j \chi_k$$

where $w_j = \frac{\sigma_j}{\sigma_1}$, and χ_k is a constant that will be determined later.

Knowing $\nu_{k,j}$ let us rearrange differential equation (9) determining $\beta_{k,j}$ in the j-th layer:

$$\frac{\partial^2}{\partial z^2} \beta_{k,j}(\lambda,z) = -\beta_{k,j}(\lambda,z)\,(w_j \chi_k - \lambda^2) \qquad z_{j-1} > z > z_j \qquad (12)$$

Depending on the sign of the $\omega_j \chi_k - \lambda^2$ function, $\beta_{k,j}$ is a linear combination of trigonometric or hyperbolic functions:

$$\beta_{k,j}(\lambda,z) = a_{k,j} \cos P_{k,j}(z - z_{j-1}) + b_{k,j} \sin P_{k,j}(z - z_{j-1})$$

$$P_{k,j} = \sqrt{w_j \chi_k - \lambda^2} \qquad \text{if} \quad w_j \chi_k > \lambda^2 \qquad (13a)$$

$$\beta_{k,j}(\lambda,z) = a_{k,j} \,\mathrm{ch}\, P_{k,j}(z - z_{j-1}) + b_{k,j} \,\mathrm{sh}\, P_{k,j}(z - z_{j-1})$$

$$P_{k,j} = \sqrt{\lambda^2 - w_j \chi_k} \qquad \text{if} \quad \lambda^2 > w_j \chi_k \qquad (13b)$$

The values of χ_k have to be chosen in such a way that the kernel function $X(\lambda,z,t)$ and its derivative in direction z should be continuous through the layer boundaries and satisfy Eq. (6). According to the series expansion (8) functions $\beta_{k,j}$ have to satisfy the same conditions. In consequence of Eq. (6a) at the surface:

$$\lambda\, a_{k,1} + P_{k,1}\, b_{k,1} = 0 \qquad (14a)$$

At the j-th layer boundary in consequence of the continuity of $\beta_{k,j}$:

$$a_{k,j} \cos \Phi_{k,j} + b_{k,j} \sin \Phi_{k,j} - a_{k,j+1} = 0 \qquad (14b)$$

At the j-th layer boundary in consequence of the continuity of $\frac{\partial}{\partial z} \beta_{k,j}$:

$$-a_{k,j} P_{k,j} \sin \Phi_{k,j} + b_{k,j} P_{k,j} \cos \Phi_{k,j} - b_{k,j+1} P_{k,j+1} = 0 \qquad (14c)$$

At the lowest layer boundary in consequence of Eq. (6b):

$$\begin{aligned}&-a_{k,\,n-1}\,P_{k,\,n-1}\sin\Phi_{k,\,n-1}-a_{k,\,n-1}\lambda\cos\Phi_{k,\,n-1}+\\&+b_{k,\,n-1}\,P_{k,\,n-1}\cos\Phi_{k,\,n-1}-b_{k,\,n-1}\,\lambda\sin\Phi_{k,\,n-1}=0\end{aligned}\qquad(14\text{d})$$

where:

$$\Phi_{k,j}=P_{k,j}(z_j-z_{j-1})\qquad j=1,\dots,n-1$$

Equations (14) are valid in the case of $w_j\,\lambda_k>\lambda^2$ in every layer, viz. $\beta_{k,j}(\lambda,z)$ is generated by linear combination of sine and cosine functions (13a). Formulae similar to Eqs. (14) are valid even if function $\beta_{k,j}(\lambda,z)$ is a linear combination of functions that are hyperbolic in one layer or some layers only (13b). Thus coefficients $a_{k,j}$ and $b_{k,j}$ are determined by the homogeneous system of linear equations (14). In the case of n layers the number of equations and unknowns is $2(n\text{-}1)$. It is necessary that the determinant of the system of equations be zero in order to have a solution of this system in addition to the solution that is identical with zero. This can be achieved by choosing χ_k properly. Bearing in mind that only the proximal elements of the main diagonal are not equal to zero, the value of the determinant can be computed by a relatively simple algorithm. Hereafter χ will be marked with index k occurring in the expansion of Eq. (8) when it de facto indicates a number for which the system of equations (14) can be solved. Let us show as an example the determinant of the system of equations (14) for a four-layer case for every χ where condition $\chi w_j-\lambda^2>0$ is satisfied in every layer:

$$D(\lambda,\chi)=$$

$$\begin{vmatrix}\lambda, & P_1, & 0, & 0, & 0, & 0,\\ \cos\Phi_1, & \sin\Phi_1, & -1, & 0, & 0, & 0,\\ -P_1\sin\Phi_1, & P_1\cos\Phi_1, & 0, & -P_2, & 0, & 0,\\ 0, & 0, & \cos\Phi_2, & \sin\Phi_2, & -1, & 0,\\ 0, & 0, & -P_2\sin\Phi_2, & P_2\cos\Phi_2, & 0, & -P_3\\ 0, & 0, & 0, & 0, & -P_3\sin\Phi_3-\lambda\cos\Phi_3, & P_3\cos\Phi_3-\lambda\sin\Phi_3\end{vmatrix}$$

where:

$$P_j=\sqrt{\chi w_j-\lambda^2},\qquad \Phi_j=(z_j-z_{j-1})\,P_j$$

Now we show the determinant-computing algorithm taking into account the case of both Eq. (13a) and Eq. (13b). Let $D_{j,j}$ and $D_{j+1,j}$ denote minor determinants. $D_{j,j}$ consists of the first j lines and columns of $D(\lambda,\chi)$ but in the case of $D_{j+1,j}$ instead of j-th lines of $D(\lambda,\chi)$, $(j+1)$-th lines will occur. Let β_j denote the solution of the system of equations (12) in the j-th layer for arbitrary χ. The minor determinants that correspond to the first layer are:

$$D_{2,2}=\lambda \sin\Phi_1 - P_1\cos\Phi_1$$

$$D_{3,2} = \lambda P_1 \cos\Phi_1 + P_1^2 \sin\Phi_1 \tag{15a}$$

Or if $\beta_1(\lambda,z)$ is generated by hyperbolic functions:

$$D_{2,2}=\lambda \,\mathrm{sh}\, \Phi_1 - P_1 \mathrm{ch}\, \Phi_1$$

$$D_{3,2}=\lambda P_1 \mathrm{ch}\, \Phi_1 - P_1^2 \mathrm{sh}\, \Phi_1 \tag{15b}$$

Computation of minor determinants belonging to the $(j+1)$-st layer on the basis of the minor determinants of the j-th layer is carried out in the following way:

$$D_{2(j+1),\,2(j+1)} = D_{2j,\,2j}\, P_{j+1} \cos\Phi_{j+1} + D_{2j+1,\,2j} \sin\Phi_{j+1}$$

$$D_{2(j+1)+1,\,2(j+1)} = -D_{2j,\,2j}\, P_{j+1}^2 \sin\Phi_{j+1} + D_{2j+1,\,2j} \cos\Phi_{j+1} \tag{16a}$$

The same expression when $\beta_{j+1}(\lambda,z)$ is a linear combination of hyperbolic functions follows:

$$D_{2(j+1),\,2(j+1)} = D_{2j,\,2j}\, P_{j+1}\, \mathrm{ch}\, \Phi_{j+1} + D_{2j+1,\,2j}\, \mathrm{sh}\, \Phi_{j+1}$$

$$D_{2(j+1)+1,\,2(j+1)} = D_{2j,\,2j}\, P_{j+1}^2\, \mathrm{sh}\, \Phi_{j+1} + D_{2j+1,\,2j}\, \mathrm{ch}\, \Phi_{j+1} \tag{16b}$$

Finally the total determinant based on the minor determinant corresponding to the $(n$-2)-nd layer is:

$$D(\lambda,\chi) = D_{2(n-2),\,2(n-2)}\,(-P_{n-1}^2 \sin\Phi_{n-1} - P_{n-1}\, \lambda \cos\Phi_{n-1}) +$$

$$+ D_{2(n-2)+1,\,2(n-2)}\,(P_{n-1} \cos\Phi_{n-1} - \lambda \sin\Phi_{n-1}) \tag{17a}$$

If $\beta_{n-1}(\lambda,z)$ is a linear combination of hyperbolic functions the same expression will be:

$$D(\lambda,\chi) = D_{2(n-2),\,2(n-2)}\,(P_{n-1}^2\,\mathrm{sh}\,\Phi_{n-1} - P_{n-1}\,\lambda\,\mathrm{ch}\,\Phi_{n-1}) +$$
$$+ D_{2(n-2)+1,\,2(n-2)}\,(P_{n-1}\,\mathrm{ch}\,\Phi_{n-1} - \lambda\,\mathrm{sh}\,\Phi_{n-1}) \tag{17b}$$

Henceforth if function β has only one index then it denotes a function that is defined in every layer, viz:

$$\beta_k(\lambda,z) = \beta_{k,j}(\lambda,z) \qquad \text{if } z_{j-1} > z > z_j$$

Let us see whether function $\beta_k(\lambda,z)$ that belongs to any root χ_k of equation $D(\lambda,\chi) = 0$ is generated by sine and cosine functions in at least one layer, viz. in at least one layer $w_j\,\chi_k > \lambda^2$. This is important because it ensures the existence of a smallest χ_k, viz. series (8) is actually an infinite sum in only one direction and the first term of the series will be determinant for late times. Assume that contrary to our statement $\beta_k(\lambda,z)$ is a linear combination of hyperbolic functions in every layer which means that Eqs. (15b), (16b) and (17b) are valid when determinant $D(\lambda,\chi)$ is computed. As $\Phi_1 < 0$, $D_{2,2} < 0$ and $D_{3,2} > 0$ follow from Eq. (15b). Taking $\Phi_{j+1} < 0$ into account it results from Eq. (16b) that this property is hereditary from layer to layer, viz. $D_{2j,\,2j} < 0$ and $D_{2j+1,\,2j} > 0$ if $0 < j < n-1$. Finally taking it into consideration that $\Phi_{n-1} < 0$, $D(\lambda,\chi) > 0$ is also true according to (17b), which means that equation $D(\lambda,\chi) = 0$ has no root. In consequence a function $\beta_k(\lambda,z)$ belonging to any χ_k root of the equation is a linear combination of sine and cosine functions in at least one layer.

The computation of kernel function $X(\lambda,z,t)$ has to be started with the determination of roots χ_k of equation $D(\lambda,\chi) = 0$, which is the most crucial part of the process. A numerical method is required that makes it unnecessary to compute determinant $D(\lambda,\chi)$ too many times in which case one of the advantages of the method, viz. the speed, could be lost. With the knowledge of χ_k we have to compute values $P_{k,j}$ in Eq. (13), then to solve the linear system of equations (14). Since function $\alpha_{k,j}(t)$ Eq. (11) contains a constant that will be determined later, constant $b_{k,1}$ can be chosen to equal 1 in the system of equations (14) and $a_{k,1}$ can be expressed by Eq. (14a). Knowing $a_{k,j-1}$ and $b_{k,j-1}$ Eqs. (14b) and (14c) make it possible to determine $a_{k,j}$ and $b_{k,j}$. Constants c_k can be determined by applying condition (7) after substituting formula (8) into (7) with t=0.

$$\sum_{k=1}^{\infty} c_k\,\beta_k(\lambda,z) = e^{\lambda z} \tag{18}$$

Formally, Eq. (18) is the series expansion of function $e^{\lambda z}$ in term of functions $\beta_k(\lambda,z)$. Before determining constants c_k on this basis we have to prove the orthogonality of functions $\beta_k(\lambda,z)$. For a given layered model the definition of the scalar product defined in interval $(z_{n-1}, 0)$ in the space of continuously differentiable functions can be given as:

$$\langle f, g\rangle = \sum_{j=1}^{n-1} \int_{z_j}^{z_{j-1}} f(z)\, g(z)\, w_j \, dz \tag{19}$$

For the computation of the scalar product of functions $\beta_k(\lambda,z)$ and $\beta_l(\lambda,z)$ (Eq. 19) belonging to different roots χ_k and χ_1 of equation $D(\lambda,\chi) = 0$ let us take the integral that is valid for the j-th layer:

$$\int_{z_j}^{z_{j-1}} \beta_{k,j}(\lambda,z)\, \beta_{l,j}(\lambda,z)\, w_j \, dz = \frac{1}{\chi_k - \chi_j}\left(\left[-\frac{\partial}{\partial z}\beta_{k,j}\, \beta_{l,j} \right]_{z_j}^{z_{j-1}} + \left[\beta_{k,j} \frac{\partial}{\partial z}\beta_{l,j} \right]_{z_j}^{z_{j-1}} \right) \tag{20}$$

Integral (20) can be obtained by partial integration by considering differential equation (9) relating to function $\beta_{k,j}$. During the computation of scalar product (19), as integrals (20) corresponding to the layers are summed up, terms $\beta_k(\lambda,z)$ and $\frac{\partial}{\partial z}\beta_k(\lambda,z)$ that belong to inner layer boundaries will cancel out because of the continuity. However terms corresponding to the surface and to the lowest layer boundary will cancel out owing to boundary conditions (6). Thus the system of functions $\beta_k(\lambda,z)$ is orthogonal to the scalar product definied by formula (19). As $\beta_k(\lambda,z)$ is only orthogonal but not orthonormal, normalization is required to compute expansion coefficients c_k.

$$c_k = \frac{\langle e^{\lambda z}, \beta_k \rangle}{\langle \beta_k, \beta_k \rangle} \tag{21}$$

When we compute the numerator of fraction (21) only the term that corresponds to the surface will not cancel out when integrals are summed up.

$$< e^{\lambda z}, \beta_k > = \sum_{j=1}^{n-1} \int_{z_j}^{z_{j-1}} e^{\lambda z} \beta_{k,j}(\lambda,z)\, w_j \, dz = \frac{2\lambda a_{k,1}}{\chi_k} \qquad (22)$$

Calculation of the denominator of (21) is a little more complicated but as in this case there are integrals of analytical functions and those can be computed by partial integration there is no need for numerical integration.

Tables I and *II* contain values of kernel function $X(\lambda,z,t)$ for different time values that were computed by the finite difference method and by formula (8).

time	$X(\lambda,z,t)$	
	finite difference method	series expansion
0.15020E-04	0.506120E-07	0.466440E-07
0.18399E-04	0.456334E-07	0.433343E-07
0.22154E-04	0.414997E-07	0.402167E-07
0.26659E-04	0.377440E-07	0.370948E-07
0.32391E-04	0.342071E-07	0.339257E-07
0.39050E-04	0.310262E-07	0.309217E-07
0.47310E-04	0.281279E-07	0.280964E-07
0.57072E-04	0.255988E-07	0.255910E-07
0.68712E-04	0.234067E-07	0.234051E-07
0.82980E-04	0.215164E-07	0.215161E-07
0.99876E-04	0.200088E-07	0.200087E-07
0.12015E-03	0.188494E-07	0.188494E-07
0.14456E-03	0.180045E-07	0.180046E-07
0.17384E-03	0.174167E-07	0.174168E-07
0.20914E-03	0.170042E-07	0.170043E-07
0.25156E-03	0.166867E-07	0.166871E-07
0.30000E-03	0.164108E-07	0.164113E-07

Table I. Computational results of kernel function $X(\lambda,z,t)$ by finite difference method (second column) and by formula (8) (third column). Parameters: $\rho_1=10$ Ωm, $\rho_2=100$ Ωm, $\rho_3=\infty$ Ωm, $d_1=50$ m, $d_2=50$ m, $\lambda = 0.001$

I. táblázat. Az $X(\lambda,z,t)$ magfüggvény számítása a véges differenciák módszerével (2. oszlop) és a (8) képlettel (3. oszlop). Paraméterek: $\rho_1=10$ Ωm, $\rho_2=100$ Ωm, $\rho_3=\infty$ Ωm, $d_1=50$ m, $d_2=50$ m, $\lambda = 0.001$

Табл. I. Расчет ядровой функции $X(\lambda,z,t)$ методом конечных разностей (столбец 2) и по формуле (8) (столбец 3). Параметры: $\rho_1=10$ омм, $\rho_2=10$ омм, $\rho_3=$ омм, $d_1=5$ м, $d_2=50$ м, $\lambda = 0.001$

It can be seen that for early times the results given by the two methods are different while for late times the difference between the two columns is less than 0.1 %. Computations were made by taking into account the first three terms of series expansion (8). The running time applying equation (8) is at least two orders less than in the case of the finite difference method. Taking into consideration that $v_{k,j} = w_j \chi_k$ and numbers χ_k form an ascending monotone series keeping to an infinite limit, from Eq. (11) it can be seen that for late times it is enough to compute only some of the first terms of series (8). Namely according to the effect of the exponential function further terms of the series are several orders less.

time	$X(\lambda,z,t)$	
	finite difference method	series expansion
0.15020E-04	0.133314E-07	0.122711E-07
0.18399E-04	0.111302E-07	0.104967E-07
0.22154E-04	0.929339E-08	0.893233E-08
0.26659E-04	0.766964E-08	0.748458E-08
0.32291E-04	0.623251E-08	0.615204E-08
0.39050E-04	0.505931E-08	0.502986E-08
0.47310E-04	0.411569E-08	0.410739E-08
0.57072E-04	0.339869E-08	0.339722E-08
0.68712E-04	0.285418E-08	0.285443E-08
0.82980E-04	0.243411E-08	0.243465E-08
0.99876E-04	0.212551E-08	0.212607E-08
0.12015E-03	0.190150E-08	0.190205E-08
0.14456E-03	0.174634E-08	0.174690E-08
0.17384E-03	0.164559E-08	0.164618E-08
0.20914E-03	0.158266E-08	0.158331E-08
0.25156E-03	0.154206E-08	0.154277E-08
0.30000E-03	0.151244E-08	0.151324E-08

Table II. Computational results of kernel function $X(\lambda,z,t)$ by finite difference method (second column) and by formula (8) (third column). Parameters: ρ_1=100 Ωm, ρ_2=10 Ωm, $\rho_3=\infty$ Ωm, d_1=50 m, d_2=50 m, λ = 0.001

II. táblázat. Az $X(\lambda,z,t)$ magfüggvény számítása a véges differenciák módszerével (2. oszlop) és a (8) képlettel (3. oszlop). Paraméterek: ρ_1=100 Ωm, ρ_2=10 Ωm, $\rho_3=\infty$ Ωm, d_1=50 m, d_2=50 m, λ = 0.001

Табл. II. Расчет ядровой функции $X(\lambda,z,t)$ методом конечных разностей(столбец 2) и по формуле (8) (столбец 3). Параметры: ρ_1=100 омм, ρ_2=10 омм, $\rho_3=\infty$ омм , d_1=50 м, d_2=50 м, λ = 0.001

4. Computing of the vertical component of the magnetic field strength at the midpoint of a circular induction loop

In consequence of the definition of vector potential (2) in the case of electric dipole:

$$H_z(t) = -\frac{\partial}{\partial z} A_x$$

Applying this to generate integral A_x of Eq. (4) we get the vertical component of the magnetic field strength:

$$H_z(t) = \frac{I\,dl\,y}{4\,\pi\,r} \int_0^\infty J_1(\lambda r)\,\lambda\,X(\lambda,z,t)\,\mathrm{d}\lambda$$

For a circular transmitter loop of radius r and with the receiver in the centre of the circle:

$$H_z(t) = \frac{I\,r}{2} \int_0^\infty J_1(\lambda r)\,\lambda\,X\,(\lambda,z,t)\,\mathrm{d}\lambda$$

Let us substitute its series form (Eq. 8) for kernel function $X(\lambda,z,t)$:

$$H_z(t) = \frac{I\,r}{2} \int_0^\infty J_1(\lambda r)\,\lambda \sum_{k=1}^{\infty} a_{k,1}\, c_k\, e^{-\frac{\chi_k}{\mu\,\sigma_1} t}\,\mathrm{d}\lambda \qquad (23)$$

As in practice the time derivative of the magnetic field strength is commonly measured let us derive equation (23) in terms of time and let us put the value given by formula (21) in the place of c_k:

$$\frac{\partial}{\partial t} H_z(t) = \frac{I\,r}{2\,\mu\,\sigma_1} \int_0^\infty J_1(\lambda r)\,\lambda \sum_{k=1}^{\infty} \frac{2\,P_{k,1}^2}{\lambda\,\langle \beta_k, \beta_k \rangle}\, e^{-\frac{\chi_k}{\mu\,\sigma_1} t}\,\mathrm{d}\lambda \qquad (24)$$

Thus transient curves measured by a central induction loop (CIL) array can be calculated by formula (24). We would mention that if we apply kernel function $X(\lambda,z,t)$, that can be obtained by formula (8), the transient field of a vertical magnetic field can be calculated, too. The integral that contains the Bessel function can be computed by filtering [ANDERSON 1979]. In *Table III.* we show the comparison of field values computed by different methods for a three-layered model. Henceforth we denote by n_s the number of terms that will be taken into account from series (8). The second column of the table contains ($\partial H_z(t) / \partial t$) values computed by the spectral method and in the fourth column values computed by formula (24) in case of $n_s=1$ are. At early times there is a little deviation but from the fourth time value it is less than 0.5 %. The speed of computation is one order greater than that of spectral technique. If $n_s>1$ then the accuracy improves even for early times, but it proportionally increases the running time. The third and fifth columns of Table III. contain apparent resistivity

time	dH_z/dt	apparent resistivity	dH_z/dt	apparent resistivity
0.89000E-04	-0.22504E+01	66.086	-0.18666E+01	75.449
0.11204E-03	-0.16354E+01	55.917	-0.14925E+01	59.449
0.14106E-03	-0.11949E+01	47.120	-0.11521E+01	48.351
0.17758E-03	-0.86452E+00	39.976	-0.86540E+00	40.242
0.22356E-03	-0.61168E+00	34.441	-0.61191E+00	34.432
0.28144E-03	-0.41838E+00	30371	-0.41966E+00	30.306
0.35432E-03	-0.27511E+00	27.510	-0.27602E+00	27.447
0.44606E-03	-0.17535E+00	25.627	-0.17406E+00	25.573
0.56155E-03	-0.10498E+00	24.545	-0.10526E+00	24.499
0.70695E-03	-0.60949E-01	24.153	-0.61099E-01	24.113
0.89000E-03	-0.34005E-01	24.394	-0.34081E-01	24.357
0.11204E-02	-0.18264E-01	25.253	-0.18299E-01	25.220
0.14106E-02	-0.94625E-02	26.760	-0.94779E-02	26.730
0.17758E-02	-0.47401E-02	28.980	-0.47463E-02	28.955
0.22356E-02	-0.23014E-02	32.028	-0.23041E-02	32.002
0.28144E-02	-0.10859E-02	36.057	-0.10872E-02	36.027
0.35432E-02	-0.49945E-03	41.274	-0.50012E-03	41.237
0.44606E-02	-0.22459E-03	47.947	-0.22489E-03	47.904
0.56155E-02	-0.99026E-04	56.421	-0.99134E-04	56.379
0.70695E-02	-0.42929E-04	67.133	-0.42952E-04	67.110

Table III. Comparison of ($\partial H_z(t) / \partial t$) values computed by the spectral technique (second column) and by formula (24) (fourth column). Layer parameters: $n=3$, $\rho_1=100$ Ωm, $\rho_2=10$ Ωm, $\rho_3=\infty$ Ωm, $d_1=50$ m, $d_2=50$ m

III. táblázat. Spektrál módszerrel (2. oszlop) és a (24) képlettel (4. oszlop) számított ($\partial H_z(t) / \partial t$) értékek összehasonlítása. A rétegparaméterek: $n=3$, $\rho_1=100$ Ωm, $\rho_2=10$ Ωm, $\rho_3=\infty$ Ωm, $d_1=50$ m, $d_2=50$ m

Табл. III. Сравнение значений ($\partial H_z(t) / \partial t$), полученных спектральным способом (столбец 2) и по формуле (24) (столбец 4). Параметры: $n=3$, $\rho_1=100$ омм, $\rho_2=10$ омм, $\rho_3=\infty$ омм, $d_1=50$ м, $d_2=50$ м values near $(\partial/\partial t)\ H_z$ values. In *Fig. 1* a comparison can be made between results computed by $n_s=1$, 2 and 4 and by the spectral technique. For early times the apparent resistivity curve corresponding to $n_s=1$ is above the resistivity value of the first layer (30 Ωm). The curve *of* $n_s=4$ is almost equal to the curve computed by the spectral technique. In the time interval corresponding to the measuring range of the transient equipment the applicability and values n_s of the described method depend on the layer parameters. For thick and conductive layers only the greater values of n_s can give adequate results whereas in the case of thin and non-conductive layers even $n_s=1$ gives an accurate result. If the layer parameters are such that in the major part of the measuring interval even with $n_s=4$ we cannot get an acceptable result then it is only worth applying the spectral technique. *Fig. 2* shows what restriction it means that the described computation method works only in the case of a non-conductive basement. The computed apparent resistivity curves of a three-layered model are drawn on each other and the resistivity of the basement changes (500 Ωm, 1000 Ωm,

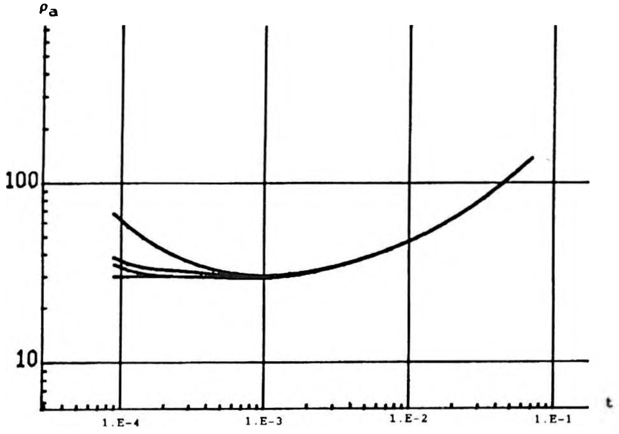

Fig. 1. Transient curves computed by spectral technique (lowest curve) and on the basis of formula (24). Layer parameters: $n=3$, $\rho_1=30$ Ωm, $\rho_2=100$ Ωm, $\rho_3=\infty$ Ωm, $d_1=200$ m, $d_2=600$ m, $r=50$ m. The curves from top to bottom were computed by taking into account terms 1, 2 and 4 of series (24)

1. ábra. Spektrál módszerrel (legalsó görbe) és a (24) képlet alapján számított tranziens görbék. A rétegparaméterek: $n=3$, $\rho_1=30$ Ωm, $\rho_2=100$ Ωm, $\rho_3=\infty$ Ωm, $d_1=200$ m, $d_2=600$ m, $r=50$ m. A különböző görbék felülről lefelé a (24) sor 1, 2, illetve 4 tagjának figyelembevételével készültek

Рис.1. Кривые переходного процесса, полученные спектральным способом и по формуле (24). Параметры слоев: $n=3$, $\rho_1=30$ OMM, $\rho_2=100$ OMM, $\rho_3=\infty$ OMM, $d_1=200$ M, $d_2=600$ M, $r=50$ M. Разные кривые получены при учете 1, 2 и 4-ого члена формулы (24)

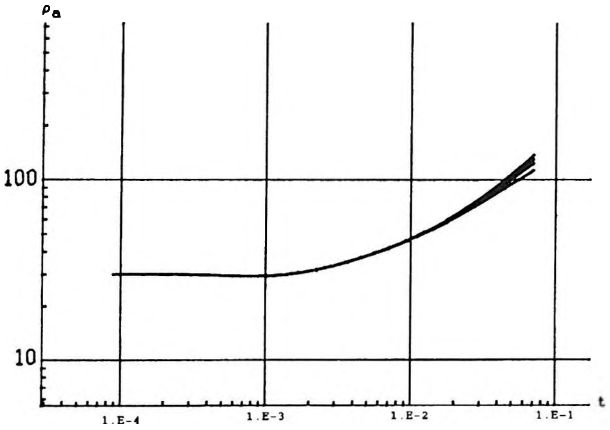

Fig. 2. Curves computed by spectral technique to demonstrate the effect of a non-conductive basement. Layer parameters: n=3, ρ_1=30 Ωm, ρ_2=100 Ωm, ρ_3=500, 1000, 2000 and ∞ Ωm, d_1=200 m, d_2=600m

2. ábra. Spektrál módszerrel számított tranziens görbék a rosszul vezető aljzat hatásának a szemléltetésére. A rétegparaméterek: n=3, ρ_1=30 Ωm, ρ_2=100 Ωm, ρ_3=500, 1000, 2000 és ∞ Ωm, d_1=200 m, d_2=600m

Рис.2. Кривые переходного процесса, расчитанные спектральным способом, для иллюстрации влияния плохопроводящего фундамента. Параметры слоев: n =3, ρ_1=30 омм, ρ_2=100 омм, ρ_3=500, 1000, 2000 и ∞ омм, d_1=200 м, d_2=600 м

2000 Ωm and non-conductive basement). For the given model deviations between the curves even for late times are small.

Conclusions

Formula (23) makes it possible to compute transient curves faster than till now, which essentially makes it quicker to interpret measured curves by curve fitting. Though the applicability of the method is restricted by assuming a non-conductive basement, and that for certain models it is inaccurate for early times, for most of the models that occur in practice it can be applied. One of the possible procedures of interpretation is to apply this computational method at the beginning, and when we only have to fit that part of the curve that belongs to early times we can change to the curve computation spectral technique.

REFERENCES

ANDERSON W. L. 1979: Numerical integration of related Hankel transforms of orders 0 and 1 by adaptive digital filtering. Geophysics, **44**, 7, pp. 1287-1305

GOLDMAN M. M. 1983: The integral finite difference method for calculating transient electromagnetic fields in a horizontally stratified medium. Geophysical Prospecting, **31**, 4, pp. 664-686

PRÁCSER E. 1986: Computing of transient response of a layered halfspace; problems in apparent resistivity inversion. Geophysical Transactions **32**, 3, pp. 221-234

SKUGAREVSKAYA O. A. 1959: Calculation of transient electromagnetic field for late times in a three-layered medium. (in Russian) Izv. Akad. Nauk. SSSR, Ser. Geofiz., No. 1, pp. 59-72

TIKHONOV A. N. and SKUGAREVSKAYA O. A. 1950: Concerning transient electrical current in an inhomogeneous layered medium. (in Russian) Izv. Akad. Nauk. SSSR, Ser. Geograf. Geofiz., XIV., 4, pp. 282-293

RÉTEGZETT FÉLTÉR FELSZÍNÉN KIALAKULÓ TRANZIENS ELEKTROMÁGNESES TÉR GYORS SZÁMÍTÁSA

PRÁCSER Ernő

Az időtartománybeli elektromágneses terek spektrál módszerrel, azaz a frekvenciatartománybeli értékekre alkalmazott inverz Fourier transzformálttal, vagy a Maxwell egyenletek időtartománybeli megoldásával számíthatók. Az utóbbi elven alapuló, a rétegzett féltér esetére érvényes és a teljes időtartományban pontos számítások általában időigényesek. Ennek az az oka, hogy a tranziens teret meghatározó képletek levezetésekor olyan parciális differenciálegyenlet is fellép, amelynek a megoldása nem állítható elő analitikus függvények segítségével. A parciális differenciálegyenletek numerikus megoldása viszont rendkívül időigényes. Ezzel szemben a spektrál módszerrel történő számítások során a frekvenciatartományban felmerülő differenciálegyenlet megoldása kifejezhető analitikus függvényekkel. Abban az esetben azonban, amikor nem törekszünk a teljes időtartományban pontos megoldásra, az időtartományban fellépő parciális differenciálegyenlet megoldása is előállítható analitikus függvények segítségével. Egy ilyen esetet ismertet a cikk, amely szigetelő aljzat esetére érvényes és a késői időkre pontos, aszimptotikus megoldáson alapul.

БЫСТРОЕ ВЫЧИСЛЕНИЕ ЭЛЕКТРОМАГНИТНОГО ПОЛЯ ПЕРЕХОДНОГО ПРОЦЕССА НА ПОВЕРХНОСТИ СЛОИСТОГО РАЗРЕЗА

Эрнё ПРАЧЕР

Электромагнитные поля во временной области могут быть рассчитаны спектральным способом, — то есть при помощи обратного преобразования Фурье, примененного для величин заданных в частотной области, или путем решения уравнений Максвелла. Способы расчетов, основанные на последнем принципе, применяемые для слоистого полупространства и точные во всем диапазоне времени, как правило, требуют много машинного времени. Это связано с тем, что при выведении формул, определяющих поле переходного процесса, имеется и такое частное дифференциальное уравнение, решение которого нельзя найти с помощью аналитических функций, а числовое решение таких уравнений является трудоемким. Наоборот, дифференциальные уравнения, возникающие при решении задачи в частотной области, можно выражать аналитическими функциями. Если не требуется точное решение во всей временной области, то и дифференциальные уравнения, заданные во временной области, могут решаться при помощи аналитических функций. В статье излагается такой случай, когда при наличии фундамента-изолятора для поздних времен получим точное решение асимптотическим способом.

GEOPHYSICAL TRANSACTIONS 1992
Vol. 37. No. 2-3. pp. 177-209

A PERCOLATION MODEL FOR THE PERMEABILITY OF KAOLINITE-BEARING SANDSTONES

Gábor KORVIN*

After a brief review of recent theories on the permeability of porous rocks, and of the rudiments of percolation theory, I shall develop a new model for the permeability of shaly sandstones containing discrete particle (kaolinite) clays. The experimentally found decrease in permeability for sufficiently high clay contents and low but non-zero porosities will be recognized as a percolation phenomenon, due to the blocking of a critical fraction of throats between the pore by kaolinite particles.

The main result is an expression for permeability (Eqs. 26a-f) in terms of grain size, porosity and kaolinite volume fraction. The expression contains a percolation factor $(p-p_c)^{PEX}$ which is identified with the divergence of the tortuosity near the percolation threshold. The percolation exponent *PEX* is simply connected to the fractal dimension of the tortuous fluid path.

The model was applied to compute the permeability of 229 kaolinite-bearing sandstone samples from Jurassic to Early Cretaceous fluvial and lacustrine reservoirs of the Eromanga Basin, South Australia. The coordination number of the approximating discrete percolation lattice and the percolation exponent were determined by computerised optimum search. There were no other adjustable parameters.

Fair agreement was found between the measured and computed permeabilities over more than 7 orders of magnitudes. Different percolation exponents were found for different lithologies: 0 for high permeability fine sand; 1.5-2 for coarse sand and siltstone; 3-5.5 for medium sand and 4.5-5.5 for low permeability (k < 100 md) fine sand.

Keywords: percolation, sandstone, permeability, fractals, models, kaolinite

---

* On leave from the Department of Geology and Geophysics, University of Adelaide, South Australia, Present address: PO Box 189, Rundle Mall, South Australia 5000

Manuscript received: 12 August, 1991

1. Historical introduction and problem discussion

1.1 Previous work on the permeability of shaly sandstones

The permeability of porous rocks can be expressed [WALSH, BRACE 1984] as:

$$k = \frac{1}{b}\Phi^3\left(\frac{V}{A_s}\right)^2\frac{1}{\tau^2} \tag{1}$$

where k is permeability, A_s/V is the surface area per unit volume, τ is tortuosity of the flow path and the constant b is equal to 2 for circular tubes and equal to 3 for cracks. An equivalent expression is:

$$k = \frac{R_{HYD}^2}{b}\Phi\frac{1}{\tau^2} \tag{2}$$

where R_{HYD} is the hydraulic radius, defined as the ratio of the pore volume to the wetted area. By definition [DULLIEN 1979], a porous material has a permeability of 1 darcy if a pressure difference of 1 atm produces a flow rate of 1 cm^3/sec of fluid with 1 cP viscosity through a cube having sides 1 cm in length. It is easy to check that 1 darcy = 0.987 μm^2, that is, if we express R_{HYD} in Eq. (2) in mm and k in millidarcies, the equation becomes:

$$k\,[md] = \frac{(R_{HYD}\,[mm])^2}{b}\Phi\frac{1}{\tau^2}10^9 \tag{3}$$

The tortuosity in Eqs. (1-3) is between 2-4 in clean sands [VOLAROVICH et al. 1968], its role has generally been neglected in permeability studies. Equation (2) correctly describes the empirical fact [MARTIN, HAMILTON 1981] that permeability generally increases with increasing porosity. To find the grain-size dependence of permeability, assume spherical grains of radius r. Then a volume V of rock of porosity Φ will contain

$$N = V(1-\Phi) : \frac{4r^3\pi}{3} = \frac{3V(1-\Phi)}{4r^3\pi}$$

grains of total surface area:

$$A_s = N\,4r^2\pi = \frac{3V(1-\Phi)}{r}$$

That is, by Eq. (1) the permability can be expected to increase with the square of grain-size [MARTIN, HAMILTON 1981], or using a similar argument, with the square of the pore size [SERRA 1984].

It has recently been realized that the permeability of clay-bearing sandstones cannot be described by simple equations like (1) or (2) in a way universally valid for different values of clay content and for all clay morphologies. Any theoretical model attempting to describe fluid flow in shaly sands must conform with the following experimental facts:

a) The permeability of shaly sandstones rapidly decreases which increasing clay content and becomes almost zero (even for $\Phi > 0$) if the clay content is greater than about 15 % (HANIN [1951] cited in [EREMENKO 1968]. DENSON et al. [1968] also found that kaolinite clays in amounts of above 16 % reduce the permeability of sands with grainsize 0.3 mm ± 0.18 mm *SD* to practically zero.).

b) The relation between porosity and permeability depends on clay morphology. AMAEFULE et al. [1988] found different trends in the permeability versus porosity crossplots for reservoir sands, depending on whether the dominant clay minerals were of the 'pore bridging' (illite), 'pore lining' (chlorite) or 'discrete particle' (kaolonite) type [NEASHAM 1977].

c) The net confining pressure has a much larger effect on permeability than on porosity [AMAEFULE et al. 1988], the pressure sensitivity is strongly correlated with clay content [AMAEFULE et al. 1988] and is different for the various clay mineralogies [AMAEFULE et al. 1988].

As by Eq. (1) permeability is inversely proportional to the square of the internal surface-to-volume ratio of the rock, it is reasonable to assume that in shaly samples this ratio is affected, or even dominated, by the enormous specific surface of the clay particles [GOODE, SEN 1988, MICHAELS, LIN 1954]. (VAN OLPHEN, FRIPIAT [1979] quote 46 m^2/g specific surface for montmorrilonite, 8-13 m^2/g for kaolinite, 100 m^2/g for illite.) Since there is a well-established empirical correlation between the cation exchange capacity (*CEC*) and the specific surface of clays [PATCHETT 1975, STEWARD, BURCK 1986], GOODE, SEN [1988] have recently expressed the volume-to-surface ratio in Eq. (1) in terms of *CEC*. They deduced an expression:

$$k \approx C\,\Phi^{m}\,\frac{\Omega_{+}^{2}}{Q_{V}^{2}} \tag{4}$$

where C is an unknown constant, Q_V is charge per unit pore volume (computed from the measured values of *CEC* as:

$$CEC = \frac{Q_V\,\Phi}{[(1-\Phi)\,\rho_g]} \tag{5}$$

ρ_g being grain density), Ω_+ is the surface charge density of clay, m is the (electric) tortuosity, determined by conductivity measurements [SEN et. al 1988].

Equation (4) is based on the assumption that the specific surface of the sand/clay composite is dominated by the surface areas of the clay particles. In Darcy's Law [DULLIEN 1979], however, we are only concerned with that part of the internal surface which actually becomes wetted. In case of pore lining (chlorite) or discrete particle (kaolinite) clays (using the classification of NEASHAM [1977]) only a small fraction of the total clay surface will be exposed to fluid flow and only in the case of pore bridging clays (illite) will most of the clay surface be wetted. Another problem with Eq. (4) is that it cannot explain the observed pressure sensitivity of the permeability of shaly sands. Because of the well-known experimental pressure dependence of porosity [HEDBERG 1926], the Goode-Sen model [GOODE, SEN 1988] (Eqs. 4 and 5) predicts a continuous decrease in permeability with increasing pressure and increasing clay content, rather than an abrupt disappearance of permeability at certain pressure and clay percentages.

To explain these discontinuous permeability changes we should have recourse to the Percolation Theory of Statistical Physics [DULLIEN 1979, ESSAM 1972, ZIMAN 1979, EFROS 1986].

1.2 Basic concepts of percolation theory

Historically, the very first published problem in percolation theory was a question related to the design of impermeable gas masks. It was raised by S. R. Broadbent — in abstract mathematical form — at a Symposium of the Royal Statistical Society on Monte Carlo Methods [BROADBENT 1954, HAMMERSLEY 1983]. At that time (1954) Broadbent was working at the British Coal Utilization Research Association on the design of gas masks for use in coal mines. The masks contained porous carbon granules into which the gas could penetrate. Broadbent found that if the pores were large enough and sufficiently well connected, the gas could permeate the interior of the granules; but if the pores were too small or inadequately connected, the gas would not get beyond the granules' surface. There was a critical porosity and pore interconnectedness, above which the mask worked well and below which it was ineffective. Thresholds of this sort are typical of percolation processes.

The basic result of percolation theory is represented in *Fig. 1* (after ZALLEN [1983]). In the (bond-) percolation problem we assume that a fraction $1-p$ ($0 \leq p \leq 1$) of the bonds of a regular grid are randomly cut and a fraction p are left uncut. Then there exists a critical fraction p_c (called percolation threshold) such that there is no continuous connection along

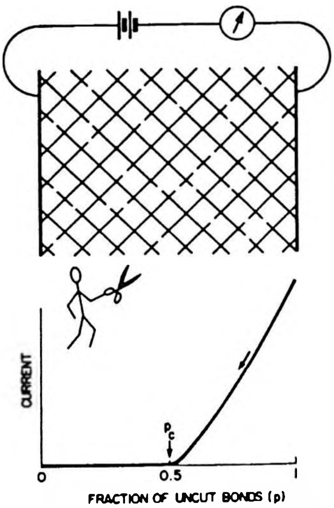

Fig. 1. Randomly cut network as example for percolation (after ZALLEN [1983])

1. ábra. Példa a perkolációra: négyzetrács véletlenszerűen elvágott élekkel. (ZALLEN [1983] nyomán)

Рис.1. Пример перколяции: квадратная решетка со случайно пересеченный гранями (по ZALLEN [1983])

the bonds of the network between the opposite faces for $p < p_c$, and there exists a connection with probability 1 for $p > p_c$.

For the 2-dimensional square lattice (Fig. 1) the percolation threshold is 0.5. In the more general case the percolation threshold depends on the dimensionality of the network, *d*, and on its coordination number *Z* (where the coordination number is the average number of bonds connected to any node of the network), but it is independent of the detailed structure of the network. *Table I* (from ZIMAN [1979]) lists coordination numbers and

Network	Dimension d	Coordination number Z	p_c
Honeycomb	2	3	0.6527
Square	2	4	0.5
Triangular	2	6	0.3473
Tetrahedral (diamond)	2	4	0.39
Simple Cubic	3	6	0.25
Body Centered Cubic	3	8	0.18
Face Centered Cubic	3	12	0.12
Hexagonal Close Packing	3	12	0.12

Table I. Bond percolation tresholds
I. táblázat. Él-perkolációs küszöbértékek
Табл. I. Пороговые значения граневой перколяции

percolation thresholds for some common networks. It was first observed by VYSSOTSKY et al. [1961] that the percolation thresholds of Table I conform quite closely to the simple empirical rule:

$$Zp_c = \frac{d}{d-1} \tag{6}$$

For a 3-dimensional network $\frac{d}{d-1} = 1.5$, that is percolation only occurs if there are on the average more than 1.5 links to any node.

Close to the percolation threshold ($p > p_c$) the nodes which are connected with each other by continuous paths form large clusters of average size ξ called the correlation distance. The correlation distance diverges for $p \rightarrow p_c$ as:

$$\xi \sim (p - p_c)^{-\nu} \tag{7}$$

(see FISCH, HARRIS [1978]). For 3-dimensional networks we have [FISCH, HARRIS 1978]:

$$\nu = 0.83 \tag{8}$$

independently of the coordination number. Obviously, the percolation between two opposite nodes of a cluster, a distance ξ apart, takes place along tortuous zig-zag paths. Near the percolation threshold the length $L(\xi)$ of a typical zig-zag path will grow as a power of ξ:

$$L(\xi) \sim \xi^{\alpha} \quad \text{for} \quad p \rightarrow p_c,\ p > p_c \tag{9}$$

or using Eqs. (7 and 8):

$$L(\xi) \sim (p - p_c)^{-\beta} \quad \text{for} \quad p \rightarrow p_c,\ p > p_c \tag{10}$$

where, for 3-dimensional lattices $\beta = \nu\alpha = 0.83\ \alpha$. As the correlation length ξ is the natural length scale in percolation problems, we shall follow RITZENBERGER, COHEN [1984] and define the tortuosity τ of the percolation path as:

$$\tau = \frac{L(\xi)}{\xi} = \xi^{\alpha - 1} = (p - p_c)^{-0.83\,(\alpha - 1)} = (p - p_c)^{-\gamma} \tag{11}$$

The exponents describing the length and tortuosity of the paths are compiled in *Table II* for different percolation models.

Definition of the path	α in $L \sim \xi^{\alpha}$	β in $L \sim (p-p_c)^{-\beta}$	γ in $\tau \sim (p-p_c)^{-\gamma}$	Ref.*	Note
Correlation length ξ	1	0.83	0	a	3-D percolation
Minimum path	1.3	1.08	0.25	b,c	3-D percolation
Conductive path	1.35	1.12	0.29	d	3-D percolation-conduction
Self-avoiding random walk on uncut bonds	1.7	1.41	0.58	e	3-D percolation
Brownian motion in 3-D	2	1.66	0.83	f	
Brownian walk on a d_f-dimensional fractal	$\alpha = \frac{3}{2} d_f$	0.83	0.83(α-1)	c	$\alpha = (3/2) d_f$ is called the 'Alexander-Orbach conjecture' [STANLEY 1986]
Brownian walk on a 3-D dimensional fractal	4.5	3.74	2.91		The pore space of certain sandstones forms an almost 3-dimensional fractal [WONG 1988]

Table II. Percolation exponents
(*REFERENCES: a— FISCH, HARRIS 1978; b—RITZENBERGER, COHEN 1984; c—STANLEY 1986; d—LUBENSKY 1977; e—LE GUILLOU, ZINN-JUSTIN 1977; f—MOSOLOV, DINARYEV 1987

II. táblázat. Perkolációs hatványkitevők
(*HIVATKOZÁS: a— FISCH, HARRIS 1978; b—RITZENBERGER, COHEN 1984; c—STANLEY 1986; d—LUBENSKY 1977; e—LE GUILLOU, ZINN; f—MOSOLOV, DINARYEV 1987

Табл. II. Перколяционные степени
(*ЛИТЕРАТУРА: a— FISCH, HARRIS 1978; b—RITZENBERGER, COHEN 1984; c—STANLEY 1986; d—LUBENSKY 1977; e—LE GUILLOU, ZINN; f—MOSOLOV, DINARYEV 1987

The exponent α in Eq. (9) has a simple physical meaning [RITZENBERGER, COHEN 1984]: for distances x smaller than ξ, α is the fractal dimension [MANDELBROOT 1982, KORVIN 1992] of the fluid paths between two nodes x apart.

1.3 Percolation models of rock permeability

The pore structure of a sedimentary rock can be converted to a discrete lattice model by letting the pores correspond to nodes and the throats to bonds. The coordination number of the pore system is defined as the average number of throats which connect each pore, it is a measure of connectivity of the network of pores [DULLIEN 1979, WARDLAW, MCKELLAR 1981] and can be determined experimentally by serial sectioning [DULLIEN 1979]. Recent theoretical work in continuum percolation [ELAM et al. 1984, HALPERIN et al. 1985] has proved the general applicability of discrete lattice models in simulating continuous problems, though the percolation transport exponents for conductivity and permeability have been found larger than their discrete lattice counterparts [HALPERIN et al. 1985].

Early application of percolation theory centred around qualitative problems of oil recovery [DULLIEN 1979] and mercury porosimetry [WARDLAW, MCKELLAR 1981]. Recent, quantitative results are reviewed by THOMPSON et al. [1987] and WONG [1988]. In 1985 HALPERIN et al. [1985] at the Harvard University introduced a 'Swiss cheese' permeability model in which the holes play the role of sand grains and the cheese is the flowing water. They found that if we make more and more holes there is a critical fraction of cheese $\Phi_c \approx 0.03-0.04$ at which electric conductivity vanishes as $(\Phi - \Phi_c)^t$ and hydraulic permeability vanishes as $(\Phi - \Phi_c)^e$, with t=2.4 and e=4.4. In an important paper KATZ, THOMPSON [1986] of Exxon Production Research, Houston, assumed that only throats wider than a given characteristic length l_c can significantly contribute to permeability and then applied percolation arguments to derive permeability in the form:

$$k = \beta \, \Phi \, l_{\max}^2 \, [p(l_{\max}) - p(l_c)]^t \tag{12}$$

with $\beta = 1/32$; for t they simply took the percolation conductivity exponent [FISCH, HARRIS 1978] t=1.9. In Eq. (12) $p(l)$ means the probability that a throat is wider than l; l_c is a critical width such that the throats wider than l_c still form a connected net across the rock; l_{max} is another size parameter. The critical width l_c can be experimentally determined using mercury intrusion [KATZ, THOMPSON 1986].

In the present study I shall develop a percolation-theoretical model for the permeability of kaolinite-bearing sandstones from oil reservoirs of the Eromanga Basin, South Australia. I shall prove that there is a percolation threshold at some critical kaolinite content, and that the tortuosity of the flow path (figuring in Eq. 2) diverges at the percolation threshold as described in Eq. (11).

The main result is contained in Eqs. (26a-f), which is formally similar to the KATZ, THOMPSON [1986] equation (12), but the power-like disappearance of permeability at the percolation threshold is attributed here to the divergence of tortuosity.

The results are only applicable to 'discrete particle' [NEASHAM 1977] clay morphologies (as kaolinite). Possible extensions to pore lining and pore bridging [NEASHAM 1977] clays will be mentioned at the end of the paper.

2. Materials and methods

2.1 Previous studies of eromanga basin petrophysics [GRAVESTOCK, ALEXANDER 1986, 1988, 1989]

The Eromanga Basin, Australia's largest onshore hydrocarbon province, covers an area approximately 1,000,000 sq km, within which up to 3,000 m of Jurassic to Late Cretaceous sediments are preserved. The sequence consists of a lower suite of continental deposits which unconformably overlie deeper Palaeozoic basins or older metamorphic and igneous rocks, and an upper suite of transgressive marine sediments which in turn are overlain by thick paralic to continental strata. Numerous oil and gas accumulations have been discovered in the lower suite over the past 10 years.

In 1985, the South Australian Department of Mines and Energy commenced a study of the petrophysics of Eromanga Basin reservoirs. Funding for the project was provided by the Commonwealth Department of Primary Industries and Energy (NERRDDC Project 820). Cores from 18 wells were selected for analysis *(Fig. 2, Table III)* and 638 cylindrical

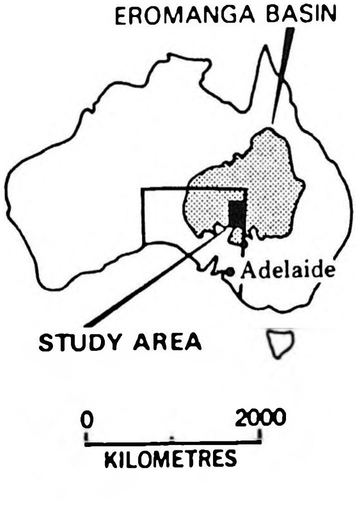

Fig. 2. Location map of the study area
2. ábra. A kutatási terület sematikus térképe
Рис.2. Карта-схема участка

core plugs were cut from lithologies ranging from coarse sandstones to mudrocks. Petrophysical analyses were carried out by the Australian Mineral Development Laboratories (AMDEL Ltd., Adelaide, South Australia).

Mid-core depth (m)	Number of samples			
	Porosity and permeability	Grain density and *CEC*	XRD	Electrical properties
1207.5	31	9	4	4
1209.8	26	14	-	-
1243.0	7	3	1	2
1247.7	29	11	4	4
1434.6	65	28	4	7
1448.4	26	10	-	5
1495.5	14	8	-	-
1505.2	42	14	4	-
1564.2	16	8	3	2
1571.2	22	11	-	3
1587.2	21	10	-	2
1608.1	35	12	4	4
1635.2	16	7	1	-
1682.7	35	10	4	-
1693.9	92	37	6	12
1797.7	49	10	5	-
1843.9	61	20	3	9
1878.5	22	9	-	4
2166.2	7	3	-	-
2663.1	22	12	4	2
Total	638	246	47	60

Table III. Summary of petrophysical measurements
The results are tabulated in Gravestock, Alexander [1988]

III. táblázat. A kőzetfizikai mérések összesitése
Gravestock, Alexander [1988]

Табл. III. Обзор измерений физических свойств
Gravestock, Alexander [1988]

All plugs were cut, trimmed, and measured for effective porosity by helium injection and horizontal permeablility to nitrogen (not Klinkenberg corrected) at overburden pressure.

Absolute grain density and cation exchange capacity (*CEC*) were determined on 246 plugs. Forty-seven samples were subject to X-ray diffraction analysis to find the distribution of the bulk mineralogy and the mineralogy of the < 2 μm fraction. Sixty samples were submitted for electrical properties determination, using simulated formation brines, twenty-one of these had repeat measurements of conductivity in NaCl brines of differing salinity. Results are tabulated in GRAVESTOCK, ALEXANDER [1988]. Five grain size categories were selected by visual examination: coarse-, medium- and fine sandstone, siltstone and mudrock. Fine sandstone samples were further sub-divided into two sets: those with permeability of 100 md or more, and those with less than 100 md permeability.

2. 2 *Petrophysical properties*

The petrophysical properties relevant to this paper are summarised in Figs. 3-8.

Figure 3 shows the porosity distribution for the selected visual grain size categories. In spite of the considerable overlap between the porosity ranges there is a clear decreasing trend in average porosity with decreasing grain size. A similar trend has been observed for the Permian reservoir rocks of the Cooper Basin, underlying the Eromanga Basin [MARTIN, HAMILTON 1981, SCHULZ-ROJAHN, PHILLIPS 1989]. When unconsolidated marine sediments are considered the grainsize—porosity relation is just the opposite (that is, the smaller the grain size the higher the porosity [HAMILTON 1972]), we assume that the trend shown by Figure 3 is due to the differences in compaction and diagenesis acting on sediments of different grain size.

The permeability vs. porosity cross plots (*Fig. 4*) show completely different patterns in the different visual grain-size ranges. The cross plot for 'fine sands' (shown twice in Fig. 4) reveals a dual character corresponding to the high permeability (k >100 md) and low permeability (k <100 md) categories. GRAVESTOCK, ALEXANDER [1986] emphasised that two porosity-permeability trends were apparent. They later [GRAVESTOCK, ALEXANDER 1988] provided empirical equations for each trend.

Semi-quantitative X-ray diffraction data for 47 samples are summarised in *Fig. 5*, which shows the distribution of the bulk mineralogy and of the < 2 μm fraction as function of the visual grain size of the host facies for each sample. The bulk mineralogy is quartz dominated whereas the clay size fraction is chiefly kaolinite, other minerals being relatively minor. The < 2 μm fraction rarely exceeded 20 percent by weight of the bulk sample.

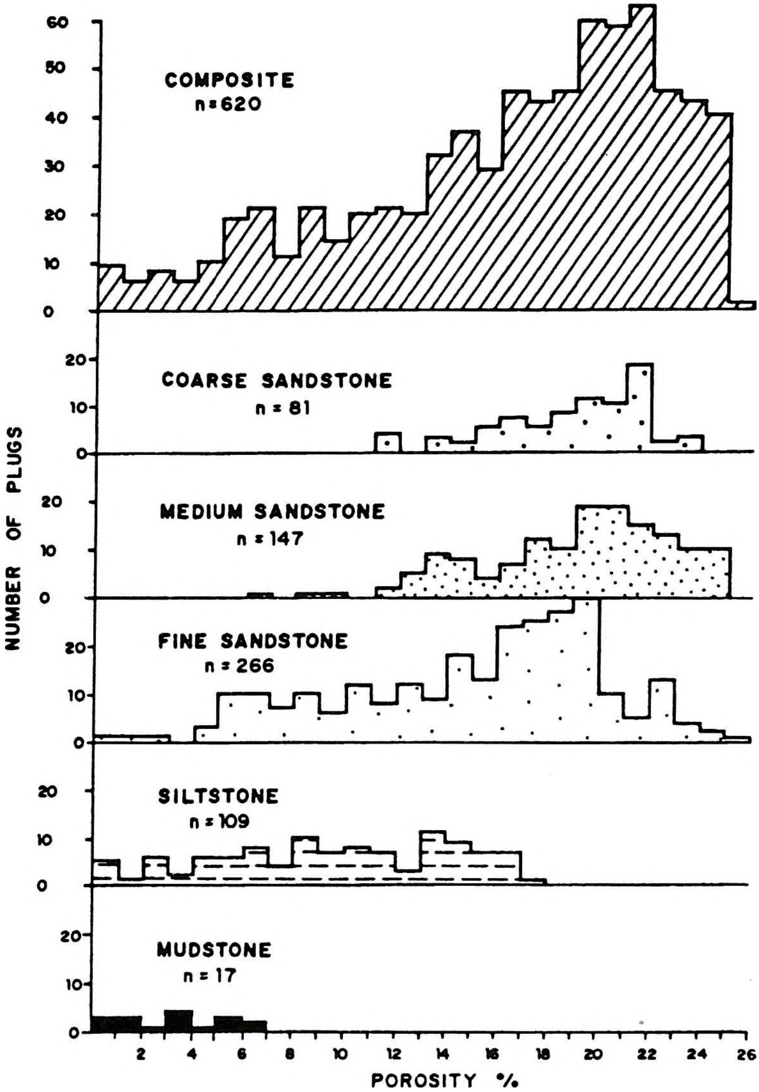

Fig. 3. Porosity distribution by visual grain-size [from GRAVESTOCK, ALEXANDER 1988]

3. ábra. A porozitás eloszlása különböző szemcseméretek esetében [GRAVESTOCK, ALEXANDER 1988]

Рис.3. Распределение пористости при различных размерах зерен [GRAVESTOCK, ALEXANDER 1988]

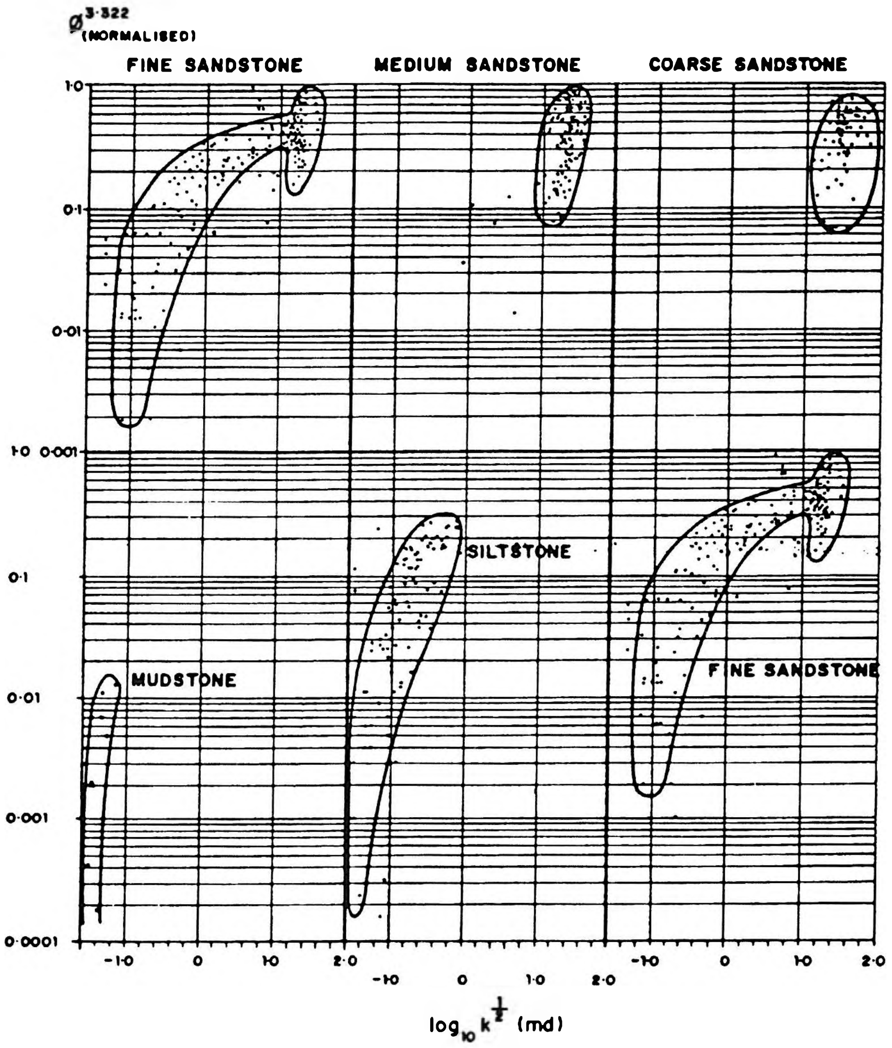

Fig. 4. Porosity—permeability trends by visual grain-size [from GRAVESTOCK, ALEXANDER 1988]

4. ábra. Porozitás—permeabilitás trendek különböző szemcseméretek esetében [GRAVESTOCK, ALEXANDER 1988]

Рис. 4. Тренды пористости–проницаемости при различных размерах зерен [GRAVESTOCK, ALEXANDER, 1988]

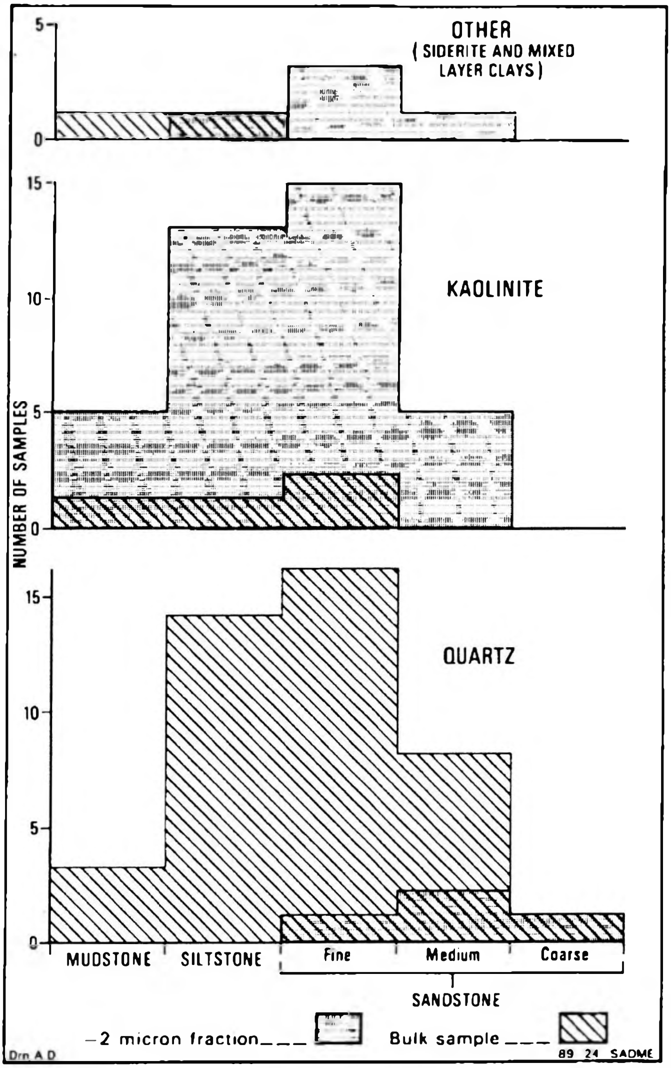

Fig. 5. Distribution of bulk and < 2 μm mineralogy determined by semi-quantitative X-ray diffraction, as a function of visual grain-size of the host facies [from GRAVESTOCK, ALEXANDER 1988]

5. ábra. A teljes minta, ill. a < 2 μm frakció, fél-kvantitatív röntgen-diffrakcióval meghatározott ásványtartalom eloszlása, különböző szemcseméretű hordozókőzetek esetében [GRAVESTOCK, ALEXANDER 1988]

Рис.5. Распределение минерального состава полной пробы и фракции меньше 2 мкм, определенного полуколичественным рентген-дифракционным способом для вмещающей породы с различным размером зерен [GRAVESTOCK, ALEXANDER 1988]

Clay minerals of relatively low electrical activity were indicated from *CEC* measurements of 246 samples whose values range from less than 1.0 to 10 meq /100 g, which is the typical range of kaolinite (*Table IV*).

Name	*CEC* meq/100 g	Ref.*
Kaolinites	3-15 4.9 (mean) 3-25	a b c
Illites	10-40 26.6 (mean) 20-30	a, c b d
Chlorite	10-40	a, c
Smectite	80-150	a, c
Montmorillonite	100-250 82.5	d b

Table IV. Cation exchange capacity of clay minerals
(*REFERENCES: a—GRIM 1968; b—VAN OLPHEN, FRIPIAT 1979; c—EDMUNDSON, RAYMER 1979; d—PATCHETT 1975)
IV. táblázat. Agyagásványok kation csere kapacitása
(*HIVATKOZÁS: a—GRIM 1968; b—VAN OLPHEN, FRIPIAT 1979; c—EDMUNDSON, RAYMER 1979; d—PATCHETT 1975)
Табл. IV. Емкость обмена катионов глинистых минералов
(*ЛИТЕРАТУРА: a–GRIM 1968; b—VAN OLPHEN, FRIPIAT 1979; c—EDMUNDSON, RAYMER 1979; d—PATCHETT 1975)

According to literature, there is a good overall correlation between *CEC* and the specific surface of clays [PATCHETT 1975 , STEWARD and BURCK 1986]. In the present case the dominant clay mineral is presumed to be kaolinite which has a distinct narrow range of *CEC* values (Table IV). *Figure 6* shows the correlation between *CEC* and weight percent of the < 2 μm fraction for 27 samples. The relationship can be approximated by the empirical equation

$$\lambda = 0.021\, CEC \tag{13}$$

where *CEC* is in meq /100 g, λ is the weight proportion of the clay size (< 2 μm) fraction, determined from semiquantitative XRD [GRAVESTOCK, ALEXANDER 1988]. I shall assume that in the Eromanga Basin samples the greatest part of the clay size fraction actually consists of clay minerals (as found in other parts of the world [KUKAL, HILL 1986]) and that it is predominantly kaolinite as indicated by the *CEC* and XRD data. Also, as there is only a slight difference between the densities of quartz

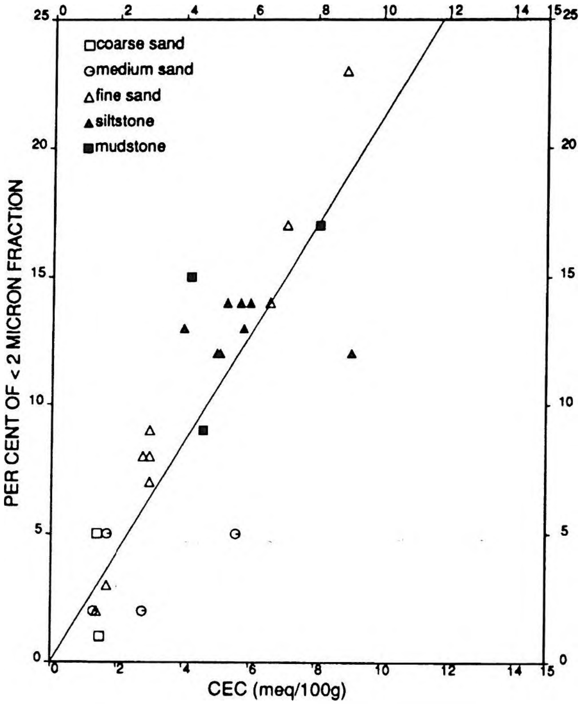

Fig. 6. Correlation between cation exchange capacity (*CEC*) and weight percent (λ) of the < 2 μm fraction. Equation of the straight line is λ = 0.021 *CEC*. The λ values were determined [by GRAVESTOCK, ALEXANDER 1988] from semiquantitative XRD

6. ábra. Korreláció a kation csere kapacitás (*CEC*) és a < 2 μm frakció súlyaránya (λ) között. A regressziós egyenes egyenlete λ = 0.021 *CEC*. A λ értékek meghatározás [GRAVESTOCK, ALEXANDER 1988] fél-kvantitatív röntgendiffrakción alapult

Рис.6. Корреляция между емкостью обмена катионов (*CEC*) и весового содержания (λ) фракции меньше 2 мкм. Уравнение линии регрессии λ = 0.021 *CEC*. Определение величины λ основано на данных полуколичиественного рентген-дифракционного способа [GRAVESTOCK, ALEXANDER 1988]

[SERRA 1984] and kaolinite [GRIM 1968], I shall identify the λ in Eq. (13) with the volume fraction of kaolinite.

Previous studies of GRAVESTOCK, ALEXANDER [1988] have already indicated that *CEC* values can be used to judge reservoir quality: good reservoir sandstones (*k* >100 md) have *CEC* values less than 3.0 meq / 100 g whereas fine grained, shaly sediments with fair to nil reservoir quality have higher *CEC*'s (*Fig. 7*). The main task of the next section will be to develop this empirical observation into a physical theory of the permeability of kaolinite bearing sandstones.

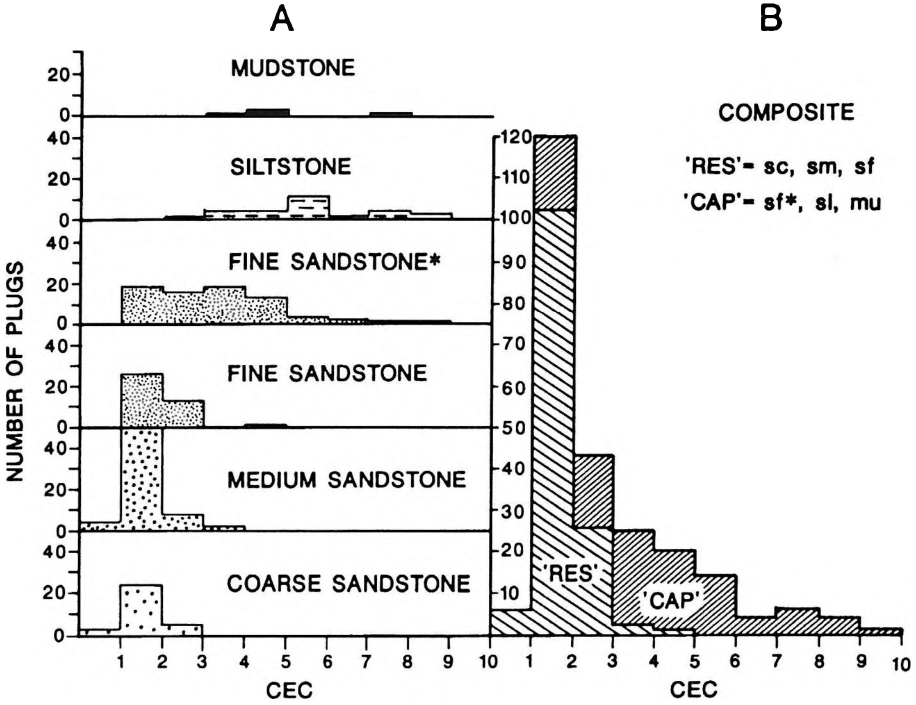

Fig. 7. Cation exchange capacity distribution with visual grain-size (A); and CAP and RES trend distribution with *CEC* (B) (CAP=caprock, RES=reservoir, sc=clean sand, sm=medium sand, sf=clean fine sand, sf*=shaly fine sand, si=siltstone, mu=mudstone) [from GRAVESTOCK, ALEXANDER 1988]

7. ábra. Kation csere kapacitás (*CEC*) eloszlása különböző szemcseméretekre (A); és a fedőkőzet ill. tárolókőzet trendek eloszlása különböző *CEC* értékekre (B). (CAP=fedőkőzet, RES=tárolókőzet, sc=tiszta homokkő, sm=közepes szemcseméretű homokkő, sf=finomszemcsés tiszta homokkő, sf*=agyagos finomszemcsés homokkő, si=homokliszt, mu=agyagpala). [GRAVESTOCK, ALEXANDER 1988]

Рис. 7. Распределение емкости обмена катионов (*CEC*) для разных размеров зерен (A) и распределение трендов покрывающих и вмещающих образований при разных значениях *CEC* (B). (CAP =покрывающие образования, RES=вмещающие породы, sc=чистые песчаники, sm=среднезернистые песчаники, sf=мелкозернистые чистые песчаники, sf*=глинистые мелкозернистые песчаники, si=печаные илы, mu=глинистые сланцы). [GRAVESTOCK, ALEXANDER 1988]

3. The percolation model

3.1 Theoretical derivation

In order to describe the permeability of the Eromanga Basin reservoir sandstones I start out from the formula [WALSH, BRACE 1984]:

$$k\,[md] = \frac{(R_{HYD}\,[mm])^2}{b}\,\Phi\,\frac{1}{\tau^2}\,10^9 \tag{3}$$

and express the hydraulic radius R_{HYD} and tortuosity τ in terms of grain radius (r), porosity (Φ) and kaolinite content (λ).

As we assume cylindrical tubes, b is taken as 2 [WALSH, BRACE 1984]. In a simplified rock model where the < 2 μm fraction consists of kaolinite, a volume V_0 of the rock will consist of:

$$V_1 = V_0\,(1-\Phi)\,(1-\lambda) \quad \text{quartz} \tag{14a}$$

$$V_2 = V_0\,(1-\Phi)\,\lambda \quad \text{kaolinite} \tag{14b}$$

$$V_3 = V_0\,\Phi \quad \text{pore} \tag{14c}$$

It is assumed that the volume fraction λ of kaolinite can be expressed in terms of *CEC* by the empirical equation (13). If the average radius of a quartz grain is r, the total quartz volume V_1 contains $N = \dfrac{V_0\,(1-\Phi)\,(1-\lambda)}{\frac{4}{3}\,r^3\,\pi}$ grains, that is in a volume V_0 of rock the total surface of quartz grains is:

$$S_{tot,\,quartz} = N\,4\,r^2\,\pi = \frac{3\,V_0\,(1-\Phi)\,(1-\lambda)}{r} \tag{15}$$

If (in thought) we remove all clay particles, an increased space $V_2 + V_3 = V_0\,[(1-\Phi)\,\lambda + \Phi]$ will be available for fluid flow.

As a cylinder of length h and radius R has a volume $V = R^2\pi h$ and surface area (without the bases) $S = 2\,R\pi h$, that is $R = (2\,V)/S$; we find from Eqs. (14 and 15) that the space $V_2 + V_3$ can be considered as a very long cylinder of average radius:

$$r_2 = \frac{2\,(V_2 + V_3)}{S_{tot,\,quartz}} = \frac{2}{3}\,\frac{\Phi + (1-\Phi)\,\lambda}{(1-\Phi)\,(1-\lambda)}\,r \tag{16}$$

If we put back again the kaolinite particles the radius of the cylinder will be reduced to r_1, $r_1 < r_2$ because kaolinite sticks to the walls. As all the pore space is contained within the long cylinder of radius r, and all the clay particles are dispersed within the ring $r_1 \le r \le r_2$ we can write:

$$\frac{r_1^2}{r_2^2} = \frac{\Phi V}{[\Phi V + (1 - \Phi) \lambda V]}$$

that is

$$r_1 = r_2 \sqrt{\frac{\Phi}{\Phi + (1 - \Phi) \lambda}} = r_2 \sqrt{p} \tag{17}$$

where we have introduced the notation

$$p = \frac{\Phi}{[\Phi + (1 - \Phi) \lambda]} = \frac{V_3}{(V_2 + V_3)} \tag{18a}$$

Obviously, $0 \le p \le 1$; p has a simple physical meaning: it is the ratio of open pore space to the total space filled by pores or clays. We shall also need the proportion of clay in this space, it is

$$q = 1 - p = \frac{\lambda (1 - \Phi)}{[\Phi + (1 - \Phi) \lambda]} = \frac{V_2}{(V_2 + V_3)} \tag{18b}$$

As in Darcy's Law [DULLIEN 1979] the hydraulic radius R_{HYD} is defined as the flow cross sectional area divided by the wetted perimeter, in Eq. (3) we shall use

$$R_{HYD} = \frac{r_1^2 \pi}{2 r_1 \pi} = \frac{r_1}{2} \tag{19}$$

If we assume a constant tortuosity and substitute Eqs. (16–19) into Eq. (2) we find that for any given kaolinite volume fraction λ the permeability would tend to zero as a power of Φ and that it is impossible to have zero permeability for finite (non zero) porosities. To be able to explain the experimental data (*viz.* the very low or zero permeabilities above a certain clay content, see Fig. 7) I shall transform the continuous Darcy flow to a lattice percolation problem. Let us make the pores of the rock correspond to the nodes of a discrete lattice, throats will correspond to the bonds (*Fig. 8*, where the symbolic 'current' represents hydraulic flow). If a given throat is completely blocked by kaolinite the corresponding bond will be considered as 'cut' otherwise it is 'uncut', independently of the actual radius of

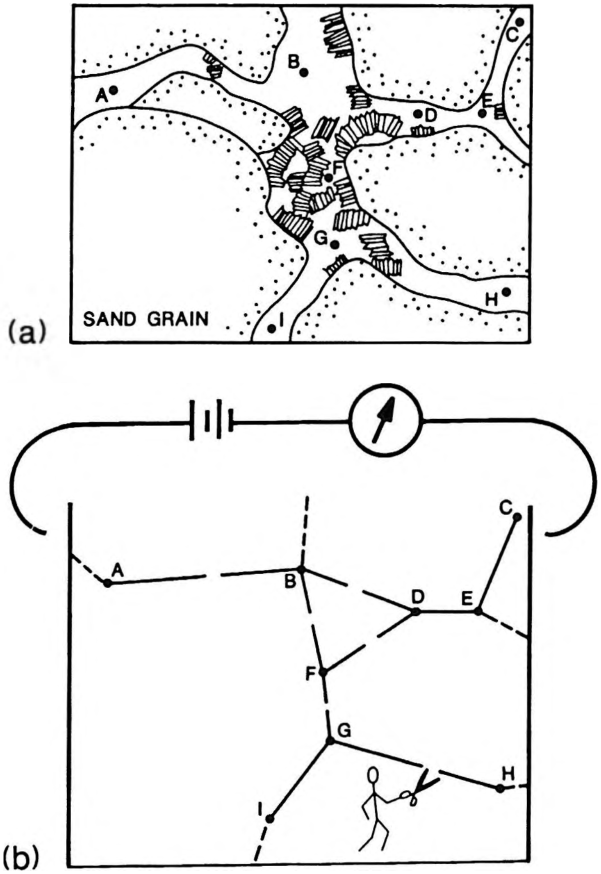

Fig. 8. Fluid transfer through kaolinite-bearing sandstone (a) and the corresponding lattice percolation model (b). Nodes correspond to pores, uncut bonds to open throats, cut bonds to throats blocked by kaolinite particles. The symbolic 'current' can be an arbitrary transfer process

8. ábra. Folyadék-áramlás kaolinit-tartalmú homokkövön keresztül (a), és a megfelelő diszkrét perkolációs model (b). A pórusoknak csomópont, nyílt toroknak elvágatlan él, a kaolinit részecskék által eltorlaszolt toroknak elvágott él felel meg. A szimbolikus "áram" tetszőleges átviteli folyamat lehet

Рис.8. Миграция жидкости через каолинит-содержаший песчаник (a) и отвечающая ей дискретная перколяционная модель (b). Порам соответствует точка, открытым горловинам - непересеченная грань, а закрытым горловинам- пересеченная грань. Символическому току может отвечать любой процесс переноса

the throat. The coordination number *Z* of the network depends on the original packing of the quartz grains and on subsequent compaction and diagenesis history. As the number of long-, concavo-convex and sutured contacts between grains increases with depth and age of the rock [TAYLOR 1950, SMALLEY 1967], the coordination number Z will generally decrease with increasing compaction (note the missing bond in Fig. 8b between nodes A and F, because of the concavo-convex contact between the adjacent grains). Generally, Z ranges between 1 and 6 for sandstones. Using the empirical rule [VYSSOTSKY et al. 1961]:

$$Z p_c = \frac{d}{(d-1)} \tag{6}$$

and assuming a 3-dimensional lattice, the bond percolation threshold probability becomes

$$p_c = \frac{1.5}{Z} \tag{20}$$

Because kaolinite is distributed as discrete book-like clusters (Fig. 8a), I assume that any given throat connecting adjacent pores is open with probability p and blocked by kaolinite particles with probability q (Eqs. 18a,b). In the equivalent lattice percolation problem (Fig. 8b) a fraction q of the bonds are randomly cut, and a fraction $p = 1 - q$ are left intact.

By the definition of the percolation threshold, the fluid cannot flow through the sample for $p < p_c$ and percolation only starts for $p > p_c$. Generally, the fluid particles will follow complicated zig-zag paths, the closer is p to p_c, the greater will be the length $L(x)$ of a typical flow path between two nodes, which are in a geometrical sense only a distance x apart.

As it was shown in Section 1.2, for $p \to p_c$ the tortuosity tends to infinity as

$$\tau \sim (p - p_c)^{-0.83\,[\alpha - 1]} \tag{11}$$

that is $\frac{1}{\tau^2}$ of the permeability equation (2) or (3) will tend to zero as

$$\frac{1}{\tau^2} \sim (p - p_c)^{1.66\,[\alpha - 1]} \tag{21}$$

In Eqs. (11 and 21) α ($\alpha \geq 1$) is the fractal dimension [RITZENBERGER and COHEN 1984] of the percolation path for small distances. Let us define a percolation function *PERC* as

$$PERC\,(p) = \begin{cases} 0 & \text{if } p \leq p_c \\ C_0\,(p - p_c)^{1.66\,[\alpha - 1]} = C_0\,(p - p_c)^{PEX} & \text{if } p \geq p_c \end{cases} \tag{22}$$

where *PEX* (percolation exponent) is defined as

$$PEX = 1.66\,(\alpha - 1) \tag{23}$$

and the normalizing constant C_0 is chosen as to make *PERC(1)=1*, that is

$$C_0 = \frac{1}{(1 - p_c)^{PEX}} \tag{24}$$

We still have to find the constant factor τ_0 in the tortuosity function

$$\frac{1}{\tau^2} = \frac{1}{\tau_0^2}\, PERC(p) \tag{25}$$

For clean sandstones $\lambda = 0$, consequently $p=1$ and *PERC(1)*=1, that is for τ_0 we must choose some average tortuosity value which is characteristic to clean sands in the ambient pressure range of the Eromanga Basin reservoir rocks [GRAVESTOCK and ALEXANDER 1988] (12,500–22,000 kPa). According to high-pressure studies [VOLAROVITCH et al. 1968] $\tau_0 = 4$ seems a reasonable choice.

Combining Eqs. (3, 13 and 16–25) the final expression for k becomes

$$k = \begin{cases} \dfrac{R_{HYD}^2}{b\,\tau_0^2}\,\Phi\,10^9\,\dfrac{(p - p_c)^{PEX}}{(1 - p_c)^{PEX}} & \text{if } p \geq p_c \\[2ex] 0 & \text{if } p \leq p_c \end{cases} \tag{26a}$$

with

$$b = 2, \quad \tau_0 = 4 \tag{26b}$$

$$R_{HYD} = \frac{1}{3}\,\frac{\Phi + (1 - \Phi)\,\lambda}{(1 - \Phi)\,(1 - \lambda)}\, r\sqrt{p} \tag{26c}$$

$$\lambda = 0.021\, CEC \tag{26d}$$

$$p = \frac{\Phi}{[\Phi + (1 - \Phi)\,\lambda]} \tag{26e}$$

$$p_c = \frac{1.5}{Z} \tag{26f}$$

Equation (26) is the main result of the present paper. In the actual application of these expressions to Eromanga Basin sandstones, the coordination number Z and the percolation exponent PEX were determined numerically. I assumed various Z and PEX values ($1 \leq Z \leq 6$; $1 \leq PEX \leq 6$), computed the permeabilities $k_{comp}(Z, PEX)$ for all samples and then minimised the error

$$DEV(Z, PEX) = \sum [\log k_{meas} - \log k_{comp}(Z, PEX)]^2 \qquad (27)$$

with respect to Z and PEX.

Note that Eq. (26) has the same form as the Katz-Thompson [1986] percolation equation

$$k = \beta \, \Phi \, l_{\max}^2 \, [p(l_{\max}) - p_c)]^t \qquad (12)$$

even the constant factors are the same ($\beta = \frac{1}{32}$ in Eq. (12) and $\frac{1}{(b\,\tau_0^2)} = \frac{1}{32}$ in Eq. (26)).

Equation (26) of the present paper, however (which strictly speaking only applies to kaolinite-bearing sands) has been derived using quite different arguments, and the percolation factor $(p - p_c)^{PEX}$ corresponds to the normalized reciprocal squared tortuosity of the fluid paths near the percolation threshold.

3.2 Application to the Eromanga Basin reservoir rocks

I applied the percolation model of Eqs. (26a-f) to compute the permeabilities of 229 sandstone samples from Eromanga Basin reservoirs. In the computations I used measured values of porosity and of cation exchange capacity (CEC), and visual grain size estimations. I assumed that the clay size (< 2 μm) fraction behaves as kaolinite for all samples, in the sense that the permeability reduction is due to the blocking of a part of the throats by discrete clusters of clay particles. The clay volume content was estimated from the measured CEC using Eq. (13). The percolation parameters Z and PEX had been numerically optimised for each lithology class. The main problem in applying Eqs. (26) to the real data has been that in Eq. (26c) we need a numerical value for the mean grain radius r. First, I identified the qualitative lithologic classes with the Wentworth size classes [PETTIJOHN et al. 1972] (see Table V) and defined $\bar{r}$ as the radius of a particle at the middle of the corresponding size range, that is $\bar{r} = 0.375$; 0.1875; 0.094; 0.094; 0.02 for the respective lithologies 1, 2, 3, 4 and 5 (Table V). As this

Lithology Number	Code	Name	Wentworth Size Range (mm)	$\bar{r}$	No. of samples	Φ_{min}	Φ_{max}	Z_{opt}	PEX_{opt}
1	❑	Coarse sandstone	1-0.5	0.375	31	0.11	0.24	2.5	1.5
2	❍	Medium sandstone	0.5-0.25	0.188	57	0.06	0.25	2.5	3.0
3	■	High k (clean) fine sandstone	0.25-0.125	0.094	37	0.0	0.26	-	0
4	Δ	Low k (shaly) fine sandstone	0.25-0.125	0.094	74	0.0	0.26	6.0	5.5
5	▲	Silstone	0.0625-0.0039	0.02	30	0.0	0.18	6.0	2.0

Table V. Summary of data used to construct Figure 9
V. táblázat. A 9. ábra szerkesztéséhez felhasznált adatok
Табл. V. Данные, использованные при составлении рис.9.

resulted in an unreasonable large scatter in k_{comp}, I decided to estimate graintsize within the allowed range by assuming some smooth dependence on porosity. After many trials and errors I have found that the best way for approximating the grain size of any sample of a given lithology i (i=1, 2,..., 5) is to linearly interpolate the logarithm of the grain size between the Wentworth limits as Φ varies between the measured bounds $\Phi^{(i)}_{\min}$ and $\Phi^{(i)}_{\max}$:

$$\log 2r(i) = \log 2r_{\max}(i) + \frac{\Phi - \Phi_{\min}(i)}{\Phi_{\max}(i) - \Phi_{\min}(i)} [\log 2r_{\max}(i) - \log 2r_{\min}(i)]$$

$$(i = 1, 2, ..., 5) \qquad (28)$$

(The grainsize-porosity dependence of Eq. (28) is in accord with the results of HAMILTON [1972] for recent marine sediments.)

The optimal coordination number Z_{opt} and percolation exponent PEX_{opt} were separately determined for each lithology. I computed k from Eqs. (26a-f) and Eq. (28) for different values of Z and PEX ($2 \leq Z \leq 6$; $1 \leq PEX \leq 6$) and determined Z_{opt} and PEX_{opt} as to minimise the error between the logarithms of the measured and computed permeabilities. Using the optimised values of Z and PEX (compiled in Table V) a fair agreement was obtained between measured and computed permeabilities over seven orders of magnitude (*Fig. 9*). The optimisation of expression

(27) with respect to *Z* and *PEX* was not unambiguous: as shown in *Fig. 10* for each lithology there are distinct clusters of suboptimal parameters (*Z*, *PEX*) around the optimal (Z_{opt}, PEX_{opt}) which were found almost as effective in optimising the error, apart from insignificant digits.

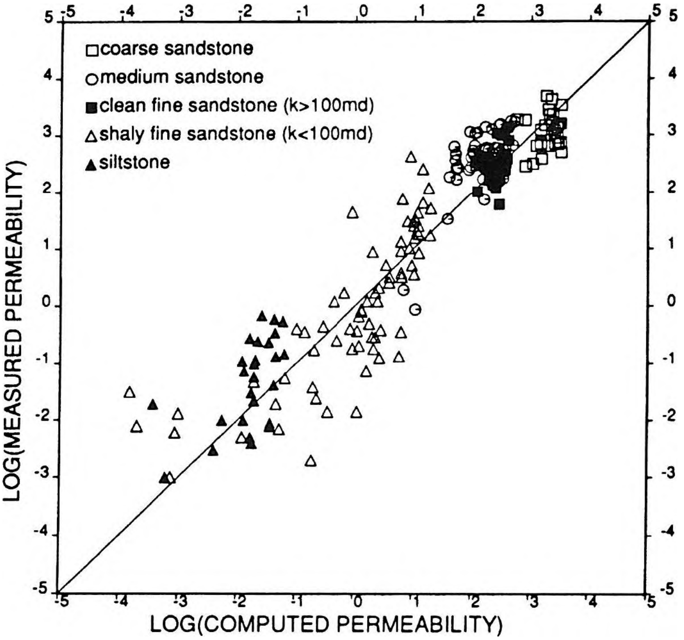

Fig. 9. Crossplot of measured vs. computed permeabilites

9. ábra. Mért permeabilitás — számított permeabilitás crossplot

Рис. 9. Связь между измеренной и вычисленной проницаемостью

4. Discussion and conclusions

Using the optimised percolation parameters (Table V) I could keep the deviation between measured and computed permeabilities within order of magnitude limits, except for a few fine-grained samples (Fig. 9). The scatter is due to three factors:

a) visual, rather than quantitative, average grain-size estimation; samples frequently displayed a range of grain sizes of several phi units;

b) difficulties in measuring very low permeabilities; and

c) using an insufficient number of semiquantitative XRD data to express kaolinite volume content in terms of *CEC* (Eq. 13).

As by Eqs. (26a,c) permeability is proportional to the squared radius of quartz grains, if grain size is only known qualitatively to belong to a given Wentworth scale class this involves a scatter of $\pm\log_{10}2^2 = \pm0.6$ in $\log k_{comp}$.

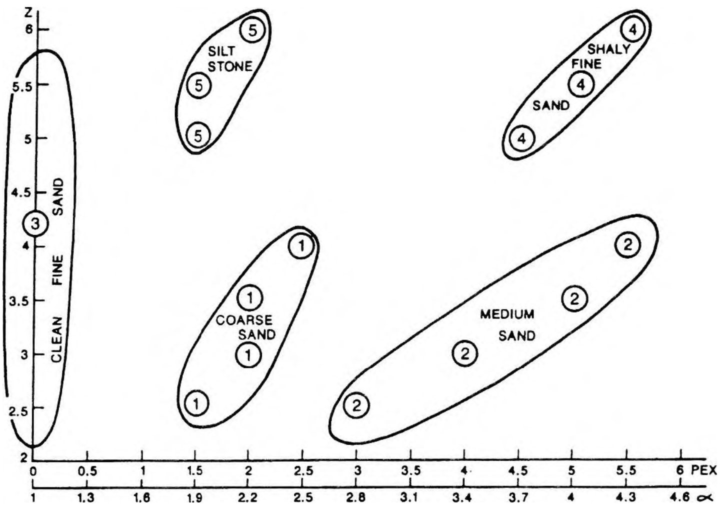

Fig. 10. Optimal percolation parameters Z and PEX for the different lithologies (Z=coordination number, PEX=percolation exponent, α =fractal dimension of the tortuous flow path)

10. ábra. Optimális perkolációs paraméterek különböző litológiákra (Z=koordinációs szám, PEX=perkolációs hatvány kitevő, α=a tekervényes folyadékpálya fraktál-dimenziója)

Рис.10. Оптимальные перколяционные параметры для разного литологического состава (Z= координационное число, PEX=перколяционная степень, α=фрактал-измерение траектории жидкости

The grain-size of 'siltstone' can be anywhere between 0.0625-0.0039 mm which implies a scatter of more than two orders of magnitude in k_{comp}. Also, the fine sandstones with k <100 md very likely spread over 2 or 3 Wentworth classes (judged from the range of their permeabilities) which explains the large scatter for this lithology.

The scatter of fine-grained samples is further increased by the less reliable measurement of very low permeabilities.

In spite of the known difficulties [MIAN, HILCHIE 1982] of the measurement of *CEC*, GRAVESTOCK, ALEXANDER [1988] found very good correlation between *CEC* values and semiquantitative X-ray diffraction analysis of the < 2 μm size fraction. They were, however 'cautious of accepting semiquantitative XRD data on the standard against which to calibrate wireline logs' [GRAVESTOCk, ALEXANDER 1988, p. 75] and, obviously, the same criticism applies to the calibration involved by Eq. (13) of the present paper.

I am convinced that unless one can estimate the grain-size distribution and sedimentary fabric from digital image analysis of thin sections [BERRYMAN, BLAIR 1986] it is hopeless to aim at a better than order of magnitude agreement between experimental and computed permeabilities over a large porosity and grainsize range. The same conclusion has been drawn by BERRYMAN and BLAIR [1986] when reviewing recent theories of permeability.

Obviously, the double logarithmic plot of Fig. 9 does not contain those data for which either one or both of k_{meas} and k_{comp} are zero. There were only five such cases: for a 'shaly fine sandstone' sample I had $k_{meas}=0$ and $k_{comp}=0$; there were 3 'siltstone' samples and a 'shaly fine sandstone' sample with $0 < k_{meas} < 0.004$ md and $k_{comp}=0$.

It is possible to deduce the experimentally known interdependences between pressure, permeability and shaliness from a mathematical analysis of Eqs. (26a-f). For increasing pressure porosity will exponentially decrease [HEDBERG 1926], this leads to a decrease in hydraulic radius (Eq. 26c) and in the value of p (Eq. 26e). As some of the throats will close up under pressure, the average coordination number Z will also decrease, that is the percolation threshold p_c becomes larger (Eq. 26f). Consequently, both factors R_{HYD} and $(p - p_c)$ in Eq. (26a) are decreasing with increasing pressure which leads to an overall permeability decrease with increasing pressure.

Compaction has a similar effect: besides the reduction of porosity, the number of long, concavo-convex and sutured contacts between quartz grains would generally increase with depth and age [TAYLOR 1950, SMALLEY 1967], this reduces the average number of bonds belonging to a node in the corresponding percolation lattice (Fig. 8b). The coordination number Z decreases, that is the percolation threshold p_c increases (Eq. 26f). The percolation model also predicts — at least for kaolinite bearing sandstones — that the permeability reduction with increasing compaction is much more serious than porosity reduction.

An increase in kaolinite content λ slightly reduces the hydraulic radius (according to Eqs. 26c,e) but its permeability reducing effect is mainly due to the increased tortuosity described by the percolation function $\tau^2 \sim (p - p_c)^{-PEX}$.

Figure 10, showing the optimum percolation parameters (Z_{opt}, PEX_{opt}) for the different lithologies, deserves a closer lock. Observe that there are two horizontal scales: the percolation exponent PEX and the fractal dimension of the percolating fluid path α. The two values are related by: $PEX = 1.66\,(\alpha - 1)$ for 3-dimensional percolation [RITZENBERGER, COHEN 1984].

For 'clean fine sands' (lithology 3, $k \geq 100$ md) $PEX=0$, that is there is no percolation transition and tortuosity is constant independently of kaolinite content. 'Siltstones' (lith. 5) and 'shaly fine sand' (lith. 4, $k < 100$ md) have a more complicated pore network (Z=5-6) than 'coarse sands' and 'medium sands' (liths. 1 and 2) where Z=2-4.

The optimal percolation exponent is $PEX=0$ (no percolation) for 'clean fine sands'; PEX=1.5-2.5 for 'coarse sands' and 'siltstone', PEX=3-5.5 for 'medium sand' and PEX=4.5-5.5 for 'shaly fine sand'. This seems to settle the controversy [THOMPSON et al. 1987] which is the 'correct' percolation exponent: 1.9 found by KATZ, THOMPSON [1986] or the 'Swiss cheese' model percolation exponent 4.4 of Halperin's group [HALPERIN et al. 1985]. In the present example, 'siltstones' and 'coarse sand' are closer to the KATZ and THOMPSON [1986] model, while 'medium sand' and the low permeability 'shaly fine sand' to the 'Swiss cheese' model [ELAM et al. 1984, HALPERIN et al. 1985]. In general, different percolation exponents can be expected for sands of different grain-size and different clay morphology.

The percolation exponent has a simple physical meaning [RITZENBERGER and COHEN 1984]: by Eq. (23) *PEX* is connected to the fractal dimension of the fluid paths near the percolation threshold.

For the high permeability 'clean fine sand', where there is no percolation transition, the fluid path is one-dimensional. For 'coarse sand' and 'siltstones' $\alpha \approx 2$ which is the fractal dimension of Brownian motion in the 3-dimensional Euclidian space (Table II). This corresponds to the model of MOSOLOV, DINARYEV [1987] who assumed the transfer of fluid particles in a porous rock as a random Brownian motion. For 'medium sands' $\alpha = 1.8-4.3$, for 'shaly fine sand' ($k < 100$ md) $\alpha = 3.7-4.3$.

According to the Alexander-Orbach conjecture [STANLEY 1986] the fractal dimension of a random walk over a d_f-dimensional fractal structure is:

$$d_W = \frac{3}{2} d_f \qquad (29)$$

Thus, the tortous fluid paths in 'medium sands' and low permeability 'shaly fine sands' can be visualized as random walks over 1.9-2.9-dimensional and 2.5-2.9-dimensional fractal pore-spaces, respectively. The high fractal dimensionality of the pore space of these sandstones is in conformity with published results of small angle neutron scattering experiments [WONG 1988] where for certain sandstones fractal dimensions as high as 2.96 have been reported.

Equations (26a-f) only apply for sandstones containing 'discrete particle' type clay [NEASHAM 1977], for example, kaolinite. The empirical equation (13) has been established for the Eromanga Basin samples, for any other region similar calibration should be sought between kaolinite content and *CEC*, or between kaolinite content and wireline logs.

The most important finding of the present paper is that the vanishing permeability at and below the percolation threshold can be ascribed to the divergence of tortuosity. I expect this conclusion to remain valid for other clay morphologies, though different percolation models would describe the effect of pore lining (chlorite) and pore bridging (illite) clays. Mixed clay morphologies (as e.g. the Permian sandstones from the Cooper Basin, South Australia, where the illite/kaolinite ratio has been found [SCHULZ-ROJAHN, PHILLIPS 1989] to depend on the grainsize of the host rock) pose an intriguing, if not intractable, challenge.

Acknowledgements

Thanks are due to Dr. D. Gravestock and Ms. E. Alexander of the South Australian Department of Mines and Energy for providing me with a copy of their report [GRAVESTOCK, ALEXANDER 1988] and for their kind permission to use their petrophysical data. They reviewed the first draft of this paper, suggested many useful changes and kindly permitted to reproduce four illustrations of their report [GRAVESTOCK, ALEXANDER 1988] as Figs. (3, 4, 5 and 7) of the present paper.

Also, I greatly appreciate the help and encouragement of Dr. J. Jones of the Department of Geology and Geophysics, University of Adelaide.

REFERENCES

AMAEFULE J. O., KERSEY D. G., MARSCHALL D. M., POWELL J. D., VALENCIA L. E., KEELAND D. K. 1988: Reservoir description: A practical synergistic engineering and geological approach based on analysis of core data. SPE Paper 18167

BERRYMAN J. G., BLAIR S. C. 1986: Use of digital image analysis to estimate fluid permeability of porous materials: Application of two-point correlation functions. J. Appl. Phys. **60**, 6, pp. 1930-1938

BROADBENT S. R. 1954: Discussion on Symposium on Monte Carlo Methods. J. Roy. Statistic. Soc. B. 68 p.

DENSON K. H., SHINDALA A. S., FENN C. D. 1968: Permeability of sand with dispersed clay particles. Water Resource Res. **4**, 6, pp. 1275-1276

DULLIEN F. A. L. 1979: Porous Media. Fluid Transport and Pore Structure. Academic Press, New York

EDMUNDSON H., RAYMER L. L. 1979: Radioactive logging parameters for common minerals. SPWLA 20th Ann. Log. Symp. Trans. Paper O

EFROS A. L. 1986: Physics and Geometry of Disorder. Percolation theory. Mir Publishers, Moscow

ELAM W. T., KERSTEIN A. R., REHR J. J. 1984: Critical properties of the void percolation problem for spheres. Phys. Rev. Letts. **52**, 17, pp. 1516-1519

EREMENKO N. A. 1968: Geology of Oil and Gas. (In Russian) Nedra, Moscow

ESSAM J. W. 1972: Percolation and cluster size. *In*: Domb C. and Green M. S. (Eds.) Phase Transitions and Critical Phenomena. Vol. 2 Academic Press, London-New York pp. 197-270

FISCH R., HARRIS A. B. 1978: Critical behaviour of random resistor networks near the percolation threshold. Phys. Rev. B. **18**, 1, pp. 416-420

GOODE P., SEN P. N. 1988: Charge density and permeability in clay-bearing sandstones. Geophysics **53**, 12, p. 1610-1612

GRAVESTOCK D. I., ALEXANDER E. M. 1986: Porosity and permeability of reservoirs and caprocks in the Eromanga Basin, South Australia. The Australian Petroleum Exploration Association Journal **26**, pp. 202-213

GRAVESTOCK D. I., ALEXANDER E. M. 1988: Eromanga Basin, South Australia, Core and Well Log Study. National Energy Research, Development and Demonstration Programme, Project Number 820, Rept. No. NERDDP/EG89/803

GRAVESTOCK D. I., ALEXANDER E. M. 1989: Petrophysics of oil reservoirs in the Eromanga Basin, South Australia. Proc. of the Cooper and Eromanga Basins Conf. Adelaide, pp. 142-151

GRIM R. E. 1968: Clay Mineralogy (2nd Ed.) McGraw-Hill Book Co., New York

HALPERIN B. I., FENG S., SEN, P. N. 1985: Differences between lattice and continuum percolation exponents. Phys. Rev. Lett. **54**, 22, pp. 2391-2394

HAMILTON E. L. 1972: Compressional wave attenuation in marine sediments. Geophysics **37**, 4, pp. 620-646

HAMMERSLEY J. M. 1983: Origins of percolation theory. *In*: Deutscher G., Zallen R. and Adler J. (Eds.) Percolation Structures and Processes. Ann. Israel Phys. Soc. **5**, pp. 48-57

HEDBERG H. D. 1926: The effect of gravitational compaction on the structure of sedimentary rocks. Bull. AAPG **10**, 11, pp. 1035-1072

KATZ A. J., THOMPSON A. H. 1986: Quantitative prediction of permeability in porous rock. Phys. Rev. B. **34**, pp. 8179-9181

KORVIN G. 1992: Fractal Models in the Earth Sciences. Elsevier, Amsterdam - New York

KUKAL G. C., HILL R. E. 1986: Log analysis of clay volume: an evaluation of techniques and assumptions used in an Upper Cretaceous sand-shale sequence. SPWLA 27th Ann. Log. Symp., Trans., Paper RR

LE GUILLOU J. C., ZINN-JUSTIN J. 1977: Critical exponents for the n-vector model in three dimensions from field theory. Phys. Rev. Lett. **39**, pp. 95-98.

LUBENSKY T. C. 1977: Scaling theory of phase transitions in diluted systems near the percolation threshold. Phys. Rev. B. **15**, 1, pp. 311-314

MANDELBROT B. B. 1982: The Fractal Geometry of Nature. W. H. Freeman and Co., New York

MARTIN K. R., HAMILTON N. J. 1981: Diagenesis and reservoir quality, Toolache Formation, Cooper Basin. The Australian Petroleum Exploration Association Journal **21**, Pt. 1, pp. 143-154

MIAN M. A., HILCHIE D. W. 1982: Comparison of results from three cation exchange capacity (CEC) analysis techniques. The Log Analyst **23**, 5, pp. 10-16

MICHAELS A. S., LIN C. S. 1954: Permeability of kaolinite. Ind. and Eng. Chem. **46**, 6, pp. 1239-1246

MOSOLOV A. B., DINARYEV O. Yu. 1987: Fractal models of porous media. (In Russian) J. Techn. Phys. **57**, 9, pp. 1679-1685

NEASHAM J. W. 1977: The morphology of dispersed clay in sandstone reservoirs and its effects on sandstone shaliness, pore space and fluid flow properties. SPE Paper 6858

PATCHETT J. G. 1975: An investigation of shale conductivity. SPWLA 16th Ann. Log. Symp. Trans., Paper U

PETTIJOHN F. J., POTTER P. E., SIEVER R. 1972: Sand and Sandstone. Springer, Berlin-Heidelberg-New York

RITZENBERGER A. L., COHEN R. J. 1984: First passage percolation: Scaling and critical exponents. Phys. Rev. B. **30**, 7, pp. 4038-4040

SCHULZ-ROJAHN J. P., PHILLIPS S. E. 1989: Diagenetic alteration of Permian reservoir sandstones in the Nappameri Trough and adjacent areas, southern Cooper Basin. Proc. of the Cooper and Eromanga Basins Conf., Adelaide, pp. 629-645

SEN P. N., GOODE P. A., SIBBIT A. 1988: Electrical conduction in clay bearing sandstones at low and high salinities. J. Appl. Phys. **63**, 10, pp. 4832-4840

SERRA O. 1984: Fundamentals of Well-Log Interpretation. I. The Acquisition of Logging Data. Elsevier, Amsterdam-Oxford-New York-Tokyo

SMALLEY I. J. 1967: A simple model of a diagenetic system. Sedimentology, **8**, pp. 27-33

STANLEY H. E. 1986: Form: an introduction to self-similarity and fractal behaviour. *In:* Stanley H. E. and Ostrowsky N. (Eds.) On Growth and Form. Fractal and Non-Fractal Patterns in Physics. Martinas Nijhoff, Publ., Dordrecht, pp. 21-53

STEWARD H. E., BURCK L. J. S. 1986: Improved cation exchange capacity/Q_v determination using the multi-temperature membrane potential test. The Log Analyst **27**, 1, pp. 25-38

TAYLOR J. M. 1950: Pore space reduction of sandstone. Bull. AAPG **34**, 4, pp. 701-716

THOMPSON A. H., KATZ A. J., KROHN C. E. 1987: The microgeometry and transport properties of sedimentary rock. Adv. Phys. **36**, 5, pp. 625-694

VAN OLPHEN H., FRIPIAT J. J. 1979: Data Handbook for Clay Materials and Other Non Metallic Minerals. Pergamon Press, New York

VOLAROVICH M. P., MARMORSHTEIN L. M., MEKLER, Yu. B. 1968: Variation in the structure of the pore space in sandtsones under pressure. (In Russian) Izv. Akad. Nauk. SSSR, Earth Phys. No. **6**, pp. 15-19

VYSSOTSKY V. A., GORDON S. B., FRISCH, H. L., HAMMERSLEY J. M. 1961: Critical percolation probabilities (bond problem). Phys. Rev. **123**, 5, pp. 1566-1567

WALSH J. B., BRACE W. F. 1984: The effect of pressure on porosity and the transport properties of rock. Journal Geophys. Res. **89**, B11, pp. 9425-9431

WARDLAW N. C., MCKELLAR M. 1981: Mercury porosimetry and the interpretation of pore geometry in sedimentary and artificial models. Powder Techn. **29**, pp. 127-143

WONG P.-Z. 1988: The statistical physics of sedimentary rock. Phys. Today **41**, 12, pp. 24-32

ZALLEN R. 1983: Introduction to percolation: A model for all seasons. *In*: Deutscher G., Zallen R. and Adler J. (Eds.) Percolation Structures and Processes. Ann. Israel Phys. Soc. **5**, pp. 4-16

ZIMAN J. M. 1979: Models of Disorder. Cambridge U. Press, Cambridge

KAOLINIT TARTALMÚ HOMOKKÖVEK PERMEABILITÁSÁNAK PERKOLÁCIÓS MODELLJE

KORVIN Gábor

A porózus kőzetek permeabilitására vonatkozó korszerű elképzelések, és a Perkolációs Elmélet alapjainak rövid ismertetése után új modellt vezetek le a diszkrét agyagrészecskéket (kaolinit) tartalmazó agyagos homokkövek permeabilitására. A kísérletileg tapasztalt permeabilitás-csökkenés elegendően nagy agyagtartalom és alacsony, de nem zéró porozitás esetében perkolációs jelenség, annak következtében, hogy a kaolinit részecskék a pórusok közötti áteresztő nyílások ("torkok") kritikus hányadát eltorlaszolják.

A fő eredmény (26a-f egyenletek) a permeabilitás kifejezése a szemcseméret, porozitás és a kaolinit térfogathányad segítségével. Szerepel a képeletben a $(p_c - p)^{PEX}$ perkolációs faktor, amely a tortuozitás divergenciájaként értelmezhető a perkolációs küszöb közelében. A *PEX* perkolációs hatványkitevő egyszerű kapcsolatban áll a tekervényes folyadékpálya fraktál-dimenziójával.

A modellt 229 db, júra - korai kréta korú, az Eromanga medence (Dél-Ausztrália) folyami és tavi eredetű tárolóiból származó, kaolinittartalmú homokkő minta permeabilitásának kiszámítására alkalmaztam. A közelítő diszkrét perkolációs rács koordinációsszámát és a perkolációs hatványkitevőt számítógépes optimumkereséssel határoztam meg, ezenkívül nem volt más illesztési paraméter.

Jó egyezést kaptam a mért és számított permeabilitások között, több mint hét nagyságrenden át. Különböző perkolációs hatványkitevők feleltek meg az egyes litológiáknak: 0 a nagy permeabilitású tiszta homokkőnek, 1,5-2 a durvaszemcsés homokkőnek és a homoklisztnek, 3-5,5 a közepes szemcseméretű homokkőnek és 4,5-5,5 az alacsony permeabilitású (k < 100 md) finomszemcsés homokkőnek.

ПЕРКОЛЯЦИОННАЯ МОДЕЛЬ ПРОНИЦАЕМОСТИ КАОЛИНИТ-СОДЕРЖАЩИХ ПЕСЧАНИКОВ

Габор КОРВИН

После описания современных представлений о проницаемости пористых пород и основ перколяционной теории дается новая модель проницаемости глинистых песчаников, содержащих дискретные глинистые зерна (каолинита). Установленное опытным путем уменьшение проницаемости при достаточно высоком содержании глины и низкой, но отличающейся от нуля, пористости является перколяционным явлением в связи с тем, что зерна каолинита закрывают критическую часть межпоровых отверстий (горловин).

Главным результатом работы являются уравнения 26a-f, выражающие зависимость проницаемости от размера зерен, пористости и объемного содержания каолинита. В формуле имеется перколяционный фактор $(p_c - p)^{PEX}$, который можно понимать как дивергенцию тортуосности вблизи

перколяционного порога. Перколяционная степень PEX имеет простую связь с фрактал-димeнсией траектории жидкости.

Модель была применена для вычисления проницаемости 229 образцов каолинит-содержащих песчаников юрского и мелового возраста отобранных из резервуаров речного и озерного происхождения бассейна Эромендж (Южная Австралия). Перколяционная степень и координационное число приближенной дискретной перколяционной решетки были определены компьютерным способом оптимизации (других параметров сопряжения не было).

Между измеренными и расчетными значениями проницаемости наблюдается хорошее совпадение при диапазоне 7 порядков величины. Перколяционная степень зависит от литологического состава образца : 0—для чистых песчаников высокой проницаемости, 1.5-2—для грубозернистых песчаников и песчаного ила, 3-5.5—для среднезернистых песчаников и 4.5-5.5—для мелкозернистых песчаников низкой проницаемости.

GEOPHYSICAL TRANSACTION S 1992
Vol. 37. No. 2-3. pp. 211-228

EXPLORATION OF THE DÉVAVÁNYA-SOUTH BASEMENT STRUCTURE FOR HYDROCARBONS — A CASE HISTORY

Sándor PAP*, Viktor SŐREG* and Irén PAP-HASZNOS*

In 1987, wildcat Déva-D-1 reaching the basement of fissured, brecciated gneiss, provided a two-phase mixture of oil and water. As the quantity of oil was relatively significant (24.7 m^3/day oil, 7.1 m^3/day water and 1380 m^3/day gas through a 3 mm valve), it was decided to carry out a detailed investigation of the area. In 1989, the Canadian company Teknica prepared a SEISLOG section from the seismic line crossing Déva-D-1, to locate another well. This well, drilled in the same year, reached the crystalline basement at a higher position, but provided much less oil than the former one. To clarify the situation, a new seismic network was shot in 1989. By integrating all available geological and geophysical information, it was found that the strongly tectonized basement consists of hydrodynamically separated blocks. The boundaries of these blocks are formed by faults of different nature. Geochemical data suggest that the oils of Déva-D-1 belong to two different types that do not form a common system. It can even be supposed that the oils have no reservoir(s), but they migrate along the conduits formed by the fissured, brecciated zones of the basement. Proposals for further investigation are given although great risk is envolved.

Keywords: Pannonian Basin, hydrocarbons, crystalline basement, fault zones, migration, geochemical methods

1. The first phase (1981-82)

At least a decade ago seismic profiles of the neighbouring hydrocarbon fields of the Békés Basin reached the area, that we now call Dévaványa-south. The first seismic survey which delineated the structure was the 1981-82 Dévaványa-Körösladány project.

* Geofizikai Kutató Vállalat, Szolnok, Körösi u. 43. H-5000

Manuscript received: 24 July, 1991

Because it was difficult to follow the surface of the eroded Precambrian basement in the seismic time sections two contour-maps were constructed, the more probable one being presented in *Fig. 1*. Although the tectonic zone in the northwest was clearly seen in all sections, the other tectonic indications could not be systematized. Well Déva-D-1 was later located on the slope of the nose-like structure.

2. The second phase (1987-88)

The time sections of the 1981-82 survey were interpreted in 1987 by seismic stratigraphy in the framework of an OKGT-USGS contract. In this study, nine localities of basal turbidites of Early Pannonian age pinching

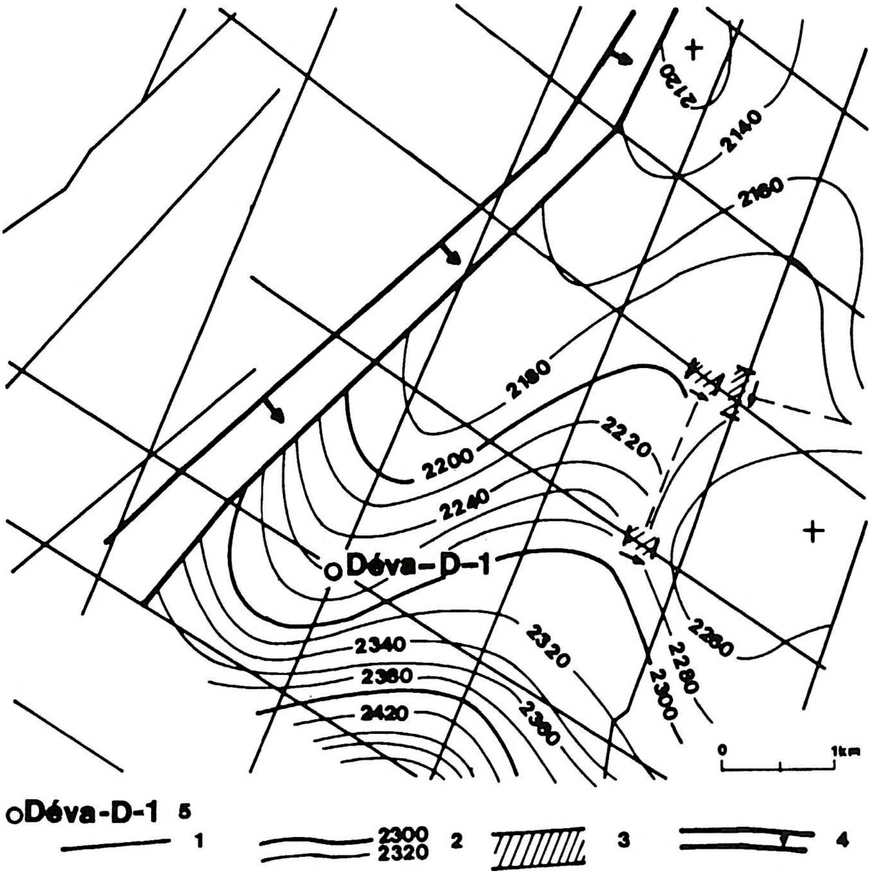

out in onlap structure (thickness about 400-500 m) were marked out in the Békés Basin. The task of well Déva-D-1 was to test one of these onlaps combined with a nose-like Miocene-Precambrian structure. The Precambrian basement was planned to be penetrated for 100 m.

Hydrocarbon indications were observed while drilling in the fissured, cataclastic granitic biotite gneiss basement, therefore the penetration was longer than planned (137 m), and three layer tests were carried out. The results of these tests are presented in *Table I* and *Fig. 2*, and some details are also given:

- Test No. 1 was carried out in an open part of the hole. Inflow from a medium permeability reservoir of seemingly unlimited reserves was recorded.
- For test No. 2 the layer was opened by perforation under depression. Yield data and effective thickness suggested higher permeability than test No. 1.
- For test No. 3, the layer was opened similarly to test No. 2. Simultaneously with the production test, logging was carried out, too. These showed inflow from the 2986-2987 m depth interval as a mixture of oil and water.

The following temperatures were recorded during test production at the depth of 2988 m:

— during production	169.7 °C
— 0.5 hours after production stop	168.8 °C
— 3.5 hours after production stop	165.4 °C
— 5.5 hours after production stop	164.0 °C

Temperature data recorded in both wells Déva-D-1 and -2 are plotted in *Fig. 3*.

After 43 hours of production, the oil yield decreased to 5 % of the initial value. Gas chromatograph measurements showed similar normal alkane

Fig. 1. Dévaványa-south area. Reflection time contour-map of a horizon chosen close to the metamorphic basement (constructed by E. Varga, E. Frindt 1983)
1—seismic line (DvG) of the 1981-82 survey; 2—time contours in ms (datum plane: +50 m);
3—fault indication; 4—regional fault zone; 5—well

1. ábra. Dévaványa-dél. A metamorf medencealjzat közelében kijelölt szint reflexiós időtérképe. (Szerkesztette: Varga E., Fridt E. 1983.)
1—1981-82-ben mért DvG jelű szeizmikus vonalak; 2—időszintvonalak ms-ban (tsz. feletti 50 m-es értékre vonatkoztatva); 3— töréses öv; 4—regionális vető; 5—mélyfúrás

Рис. 1. Участок Dévaványa-юг. Карта изохрон отражающего горизонта, отмеченного вблизи метаморфического фундамента (составили: E. Varga, E. Frindt 1983)
1— сейсмические профили (DvG), измеренные в 1981-82. гг.; 2— изохроны в мсек, отнесенные к уровню 50 м н.у.м.; 3—зона раздробления; 4— региональный разлом; 5— скважина

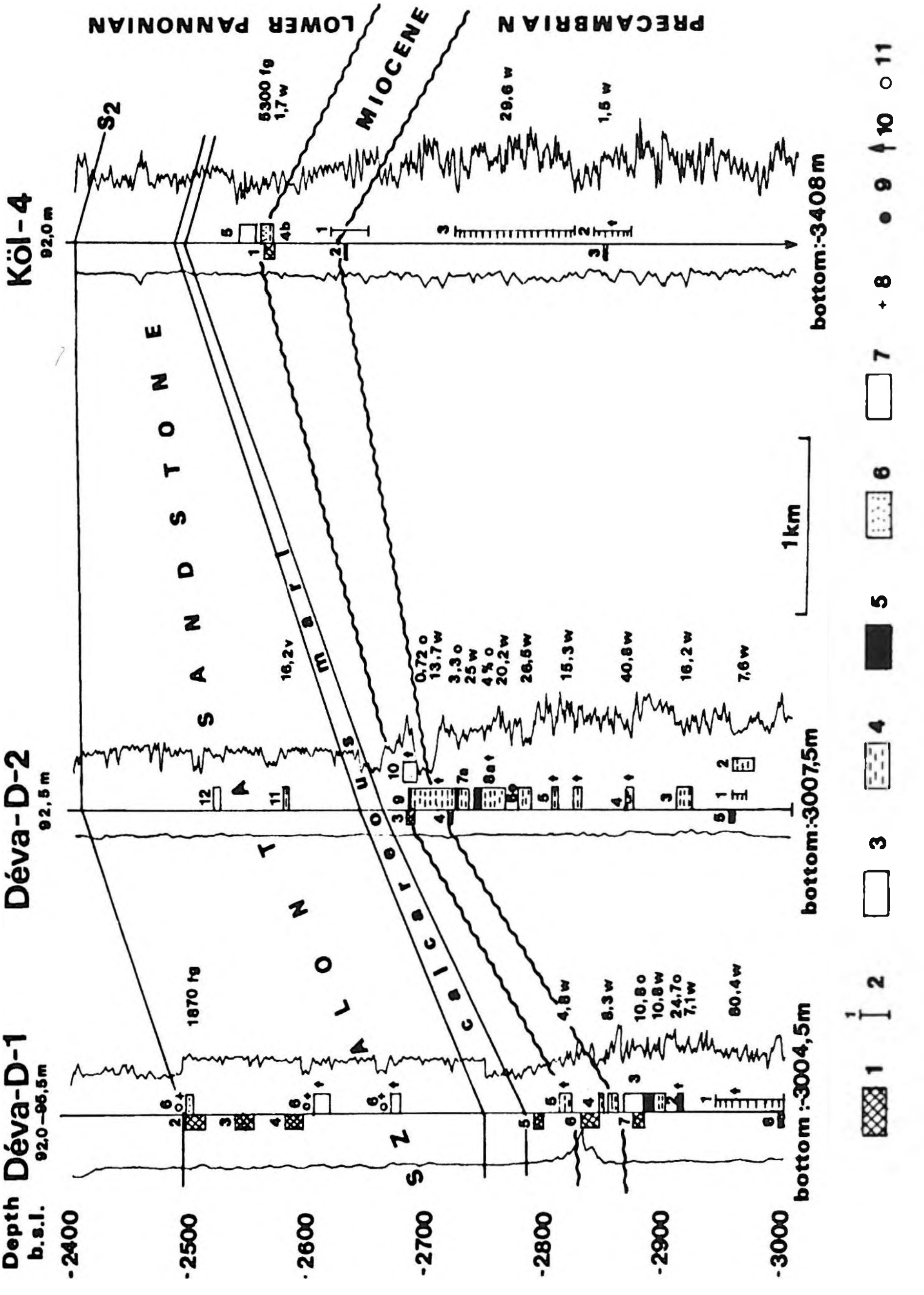
Depth b.s.l.
-2400
-2500
-2600
-2700
-2800
-2900
-3000
Déva-D-1
92,0—95,5m
bottom:-3004,5m
Déva-D-2
92,5m
bottom:-3007,5m
Köl-4
92,0m
bottom:-3408m
S2
LOWER PANNONIAN
MIOCENE
PRECAMBRIAN
SZOLNOK SANDSTONE
Tótkomlós calcareous marl
1km
1870 fg
4,8w
8,3w
10,8o
10,8w
24,7o
7,1w
80,4w
16,2v
0,72o
13,7w
3,3o
25w
4%o
20,2w
26,5w
15,3w
40,8w
16,2w
7,6w
5300 fg
1,7w
29,6w
1,5w
1
2
3
4
5
6
7
+ 8
● 9
10
○ 11

Fig. 2. Layer test results in the three wells of the study area
1—core and its number; 2—drill stem test and its number; 3—layer test and its number; 4—water inflow; 5—oil inflow; 6—gas inflow; 7—no inflow; 8—water show; 9—oil show; 10—gas show; 11—distillate show; o—oil; g—gas; w—water. Yields are given in m^3/day

2. ábra. A Dévaványa-déli és a Körösladány-4 sz. fúrások rétegvizsgálati eredményei
1—magfúrás és száma; 2—fúrószáras teszteres rétegvizsgálat és száma; 3—rétegvizsgálat és száma; 4—vízbeáramlás; 5—kőolajbeáramlás; 6—földgázbeáramlás; 7—nem adott beáramlást; 8—víznyom; 9—kőolajnyom; 10—földgáznyom; 11—párlatnyom; o—kőolaj; g—földgáz; w—víz. A hozamok m^3/nap-ban

Рис.2. Результаты исследования слоев по скважинам Dévaványa-юг и Körösladány-4
1–кэрновое бурение и его номер; 2–исследование слоев по буровому снаряду тестером и его номер; 3–исследование слоев и его номер; 4–просачивание воды; 5–просачивание нефти; 6–просачивание газа; 7– нет просачивания; 8–следы воды; 9–следы нефти; 10–следы газа; 11–следы дистиллята; o– нефти; g–газа; w–воды. Дебиты в м^3/сут

TEST		YIELD (m^3/day)		
number	location	oil	gas	water
3.	2963,0-2998,0	at the end of the test after flushing 3 m^3	200	88,4
2.	3010,0-3014,0	24,7	1380	7,1
1.	3041,0-3100,0	10,8 (by the end of the test 5 %)	350	10,8

Table I. Layer tests in the basement complex of well Déva-D-1
I. táblázat A metamorf medencealjzat vizsgálatának eredményei a Déva-D-1 fúrásban
Табл. I. Результаты исследования метаморфического фундамента в скважине Déva-D-1

distribution in tests Nos. 1 and 3, while the oil of test No. 2 contained more light hydrocarbons than the other two. The normal alkane distribution curve of the oil of test No. 2 shifted towards lower carbon atomic numbers compared to the other two (see *Fig. 4*). Analysis of gases, on the other hand, showed similarity between gases of tests Nos. 2 and 3, and proved that of test No. 1 to be of different origin.

The NaCl content of waters from tests 1 and 3 showed similarity, while that of test No. 2 was different. The complete analyses of waters could not be compared, because there was no water in test No. 3. The layer pressure in test No. 2 also proved to be different from the other two (see *Fig. 5*).

All these data led us to the conclusion that the fluids (or a part of them) of test No. 2 migrate upwards through a fissure system from the deeper parts of the metamorphic basement. It could not unambiguously be deter-

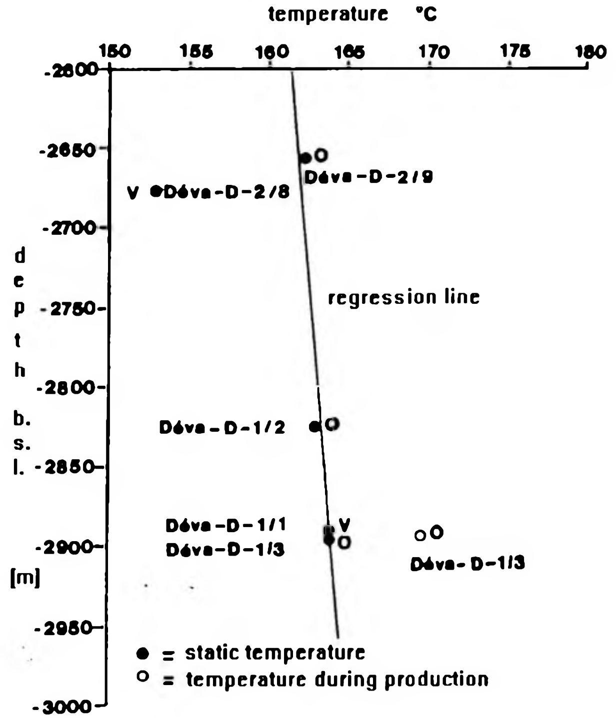

Fig. 3. Temperatures recorded during layer tests w—water inflow; o—oil inflow;

3. ábra. Rétegvizsgálatok során mért hőmérsékletek w—vízbeáramlás; o—kőolajbeáramlás

Рис. 3. Температура, измеренная при исследовании слоев w–просачивание воды; o–просачивание нефти

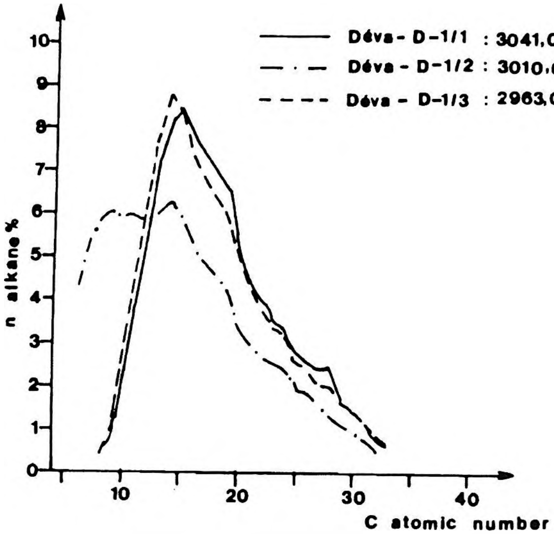

Fig. 4. Normal alkane distribution of oils found in the crystalline basement reservoir of well Déva-D-1

4. ábra. A Déva-D-1 fúrással feltárt metamorfit tárolóból származó kőolajok normál-alkán eloszlása

Рис. 4. Распределение нормального алькана нефти метаморфического резервуара вскрытого скважиной Déva-D-1

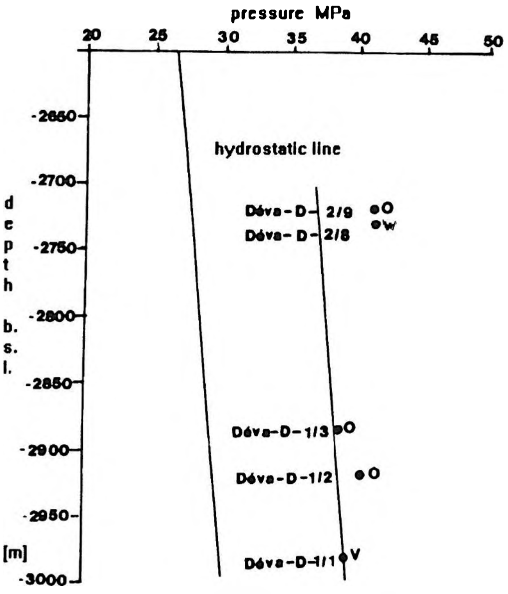

Fig. 5. Static pressures determined in the crystalline basement during layer tests in the two wells of Dévaványa
w—water inflow; o—oil inflow;

5. ábra. Rétegvizsgálatok során meghatározott statikus nyomások a dévaványa-déli fúrások által feltárt metamorfitokban
w—vízbeáramlás; o—kőolajbeáramlás

Рис. 5. Статическое давление, определенное при исследовании слоев в метаморфитах, вскрытых скважинами участка Dévaványa-юг
w—просачивание воды;
o—просачивание нефти

mined how many reservoirs exist in the basement complex. In spite of all these contradictory data, it was decided to continue exploration.

As the inner structure of the basement seemed to be crucial in solving these problems, seismic profile Dv-21 was reshot in 1987 using the latest data acquisition and processing techniques. Reflection characteristics of the basement (both surface and inner structure) were much better in this section (*Fig. 6*, for location see *Fig. 7*) than in the former ones. Two reflection patterns could be distinguished in the basement: one with low-frequency strong signals of medium continuity, and one consisting of poor-energy reflection fragments representing more or less sheared and fissured blocks. The most important feature is the overthrust plane acting as a detachment plane for the smaller faults.

A new structural map was constructed (Fig. 7), based on the new seismic profile (Dv-21), and the reprocessing of the older ones. Although it seemed most probable that oil and gas accumulation were linked with the tectonic features it was not possible to determine whether the basement elevation had a decisive role or not, i.e. whether the next well should be located towards the top zone of the elevation (point B in Fig. 7) or in the strike direction (point A in Fig. 7).

3. The third phase (1989-91)

Taking into account all the available data of seismics, well logging, layer tests and geochemical data, as well as the SEISLOG section produced

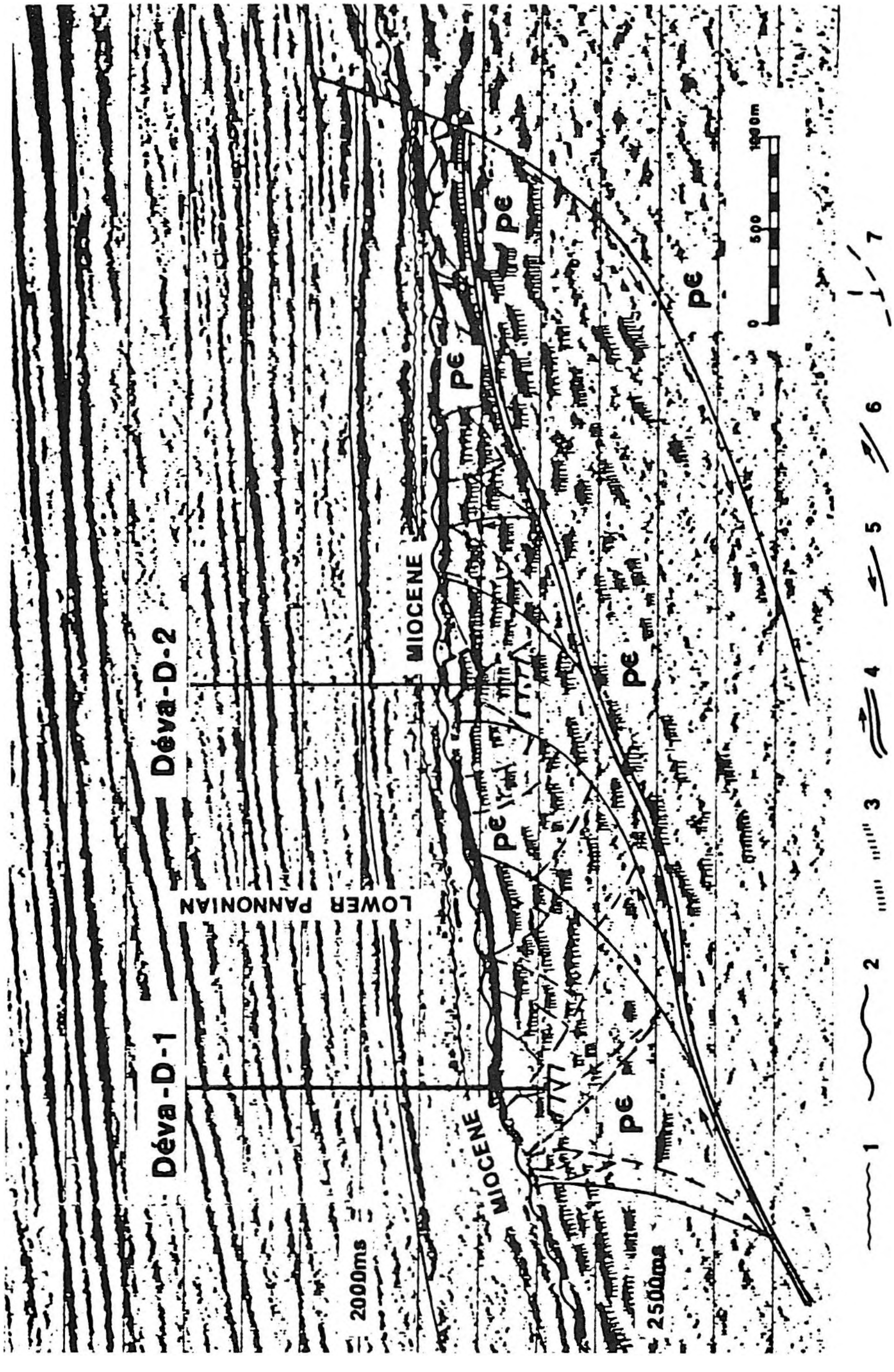
Déva-D-1
Déva-D-2
LOWER PANNONIAN
MIOCENE
MIOCENE
Pɛ
Pɛ
Pɛ
Pɛ
Pɛ
Pɛ
Pɛ
2000ms
2500ms
0
500
1000m
1
2
3
4
5
6
7

by the Canadian company Teknica, from the data of seismic section Dv-21 it was decided to locate well Déva-D-2 at point B (the SEISLOG method is described in several publications, its application and results in the Dévaványa-south area can be found in the interim report of GKV A-7/89).

Well Déva-D-2 was drilled in 1989. It reached the metamorphic basement complex at a depth of 2801 m (162 m nearer the surface than well Déva-D-1), and penetrated it for 299 m. Lithologically it was similar to the biotite gneiss known from Déva-D-1. Five layer tests were carried out below 2890 m, but pumping provided no more than water. Above this depth the water showed traces of oil which increased with decreasing depth (see Fig. 2). The maximum inflow of oil was near the top of the basement in test No. 9 (between 2815 and 2827 m): 3.3 m^3/day oil and 25 m^3/day saline water with combustible gas. The above data, as well as the next well, Köl-4 (being at an even higher structural position) prove that in this area oil and gas accumulation are not tied to structural elevation.

To clarify the situation, simultaneously to drilling well Déva-D-2, a new detailed reflection survey was shot. The structural time contour map with all relevant data is presented in *Fig. 8*, the geoseismic section connecting the three wells in *Fig. 9*. The palaeogeomorphologic dome of approximately NNE-SSW strike, is bounded by structural zones both on the NW and SE. Between these zones the basement was overthrust NE-wardly by compression from the south. The imbricated biotite gneiss block moved upwards along several small inverse fault planes.

The geochemical data are as follows: The normal alkane distribution of distillation residue over 200 °C of oils of both Déva-south wells is practically the same (*Fig. 10*). The quantity of paraffin hydrocarbons, the maximum of carbon atom distribution, the carbon preference index and the ratio of pristane/phitane differ but negligibly (*Table II*). These data suggest a moderately reducing oil generation environment, and moderate maturity

Fig. 6. A portion of seismic time section Dv-21
1—top of Miocene; 2—top of Precambrian basement; 3—'emphasized' reflections; 4—regional overthrust; 5—normal fault; 6—overthrust of lower order, limit of block; 7 — fault planes

6. ábra. A Dv-21 szeizmikus szelvény egy szakasza
1—miocén tető; 2—prekambriumi tető; 3—"kiemelt" reflexió; 4—regionális feltolódási öv; 5—törés; 6—másodlagos feltolódás, blokk-határ; 7—törési síkok

Рис. 6. Интервал сейсмического профиля Dv-21
1–кровля миоценового возраста; 2–кровля докембрийского возраста; 3–отражение от приподнятого блока; 4–зона регионального надвига; 5–разлом; 6–вторичный надвиг, граница блоков; 7–плоскости разломов

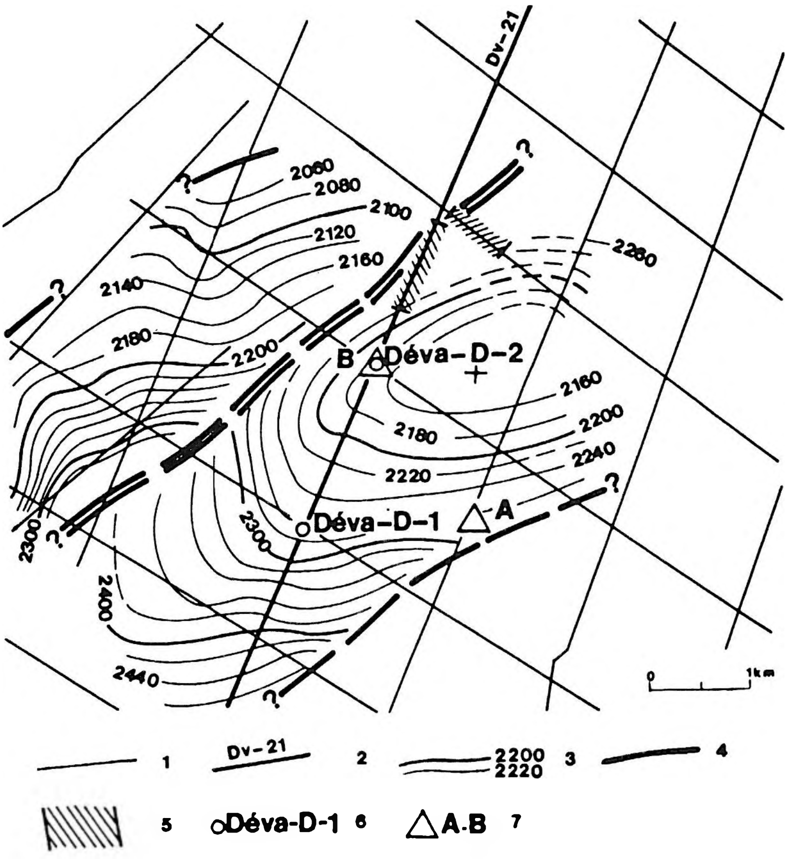

Fig. 7. Seismic time contour- map of the surface of the crystalline basement (constructed by B. SZANYI, 1988)

1—seismic lines (DvG) of the 1981-82 survey; 2—seismic line Dv-21 shot in 1987; 3—time contours in ms (datum plane: +50 m); 4—fault zone or boundary of the presumed overthrust zone; 5—zone of fractured basement; 6—well; 7—proposed location of well

7. ábra. A metamorf medencealjzat felszínének szeizmikus időtérképvázlata. (Szerkesztette: SZANYI B. 1988)

1— 1981-82-ben mért DvG jelű szeizmikus vonalak; 2—1987-ben mért Dv-21 jelű szeizmikus vonal; 3—időszintvonalak ms-ben (tsz. feletti 50 m-es értékre vonatkoztatva); 4—vetőzóna, vagy feltételezett rátolódási zóna határa; 5—medencealjzat töredezett zónája; 6—mélyfúrás; 7—tervezett fúrási variációk

Рис. 7. Схема изохрон поверхности метаморфического фундамента третичного бассейна (составил: B. SZANYI 1988. г.)

1—сейсмические профили (DvG), измеренные в 1981-82. гг.; 2—сейсмический профиль Dv-21, измеренный в 1987. г.; 3—изохроны в мсек, отнесенные к уровню 50 м н.у.м.; 4—границы разломной зоны или зоны предпологаемого надвига; 5—зона раздробления в фунданенте третичного бассейна; 6—скважина; 7—варианты проектной скважины

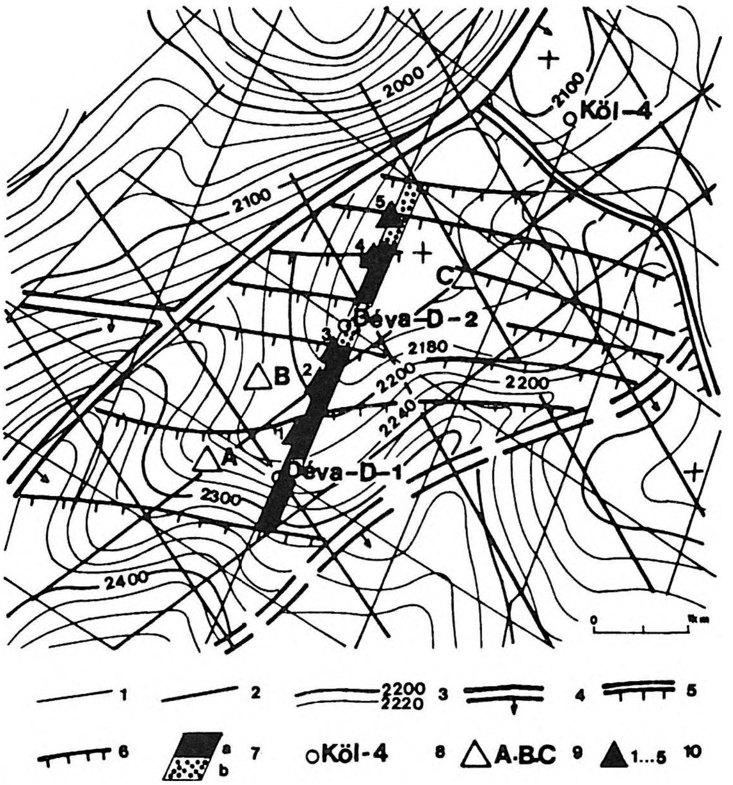

Fig. 8. Seismic time contour-map of the surface of the metamorphic basement (constructed by A. PRIBUS, B. SZANYI and V. SÓREG, 1990)
1—seismic lines of the 1981-82 survey; 2—seismic lines of the 1989 survey; 3—time contours in ms (datum plane: + 50 m); 4—fault zone; 5—limit of compressional zone; 6—overthrust; 7—prediction of Teknica, based on SEISLOG processing: a) oil, b) gas; 8—well; 9—our proposals for drilling locations; 10—drilling localities proposed by Teknica

8. ábra. A metamorf medencealjzat felszínének szeizmikus időtérképe. (Szerkesztette: PRIBUS A., SZANYI B., SÓREG V., 1990)
1—1981-82-ben mért részletező szeizmikus vonalak; 2—1989-ben mért részletező szeizmikus vonalak; 3—időszintvonalak ms-ben (tsz. feletti 50 m-es értékre vonatkoztatva); 4—vetőzóna; 5—feltételezett kompressziós zóna határa; 6—feltolódás; 7—előrejelzés a Teknica cég szeizlog feldolgozása alapján: a) kőolaj; b) földgáz; 8—mélyfúrás; 9—lehetséges fúráspontok; 10—a Teknika cég által javasolt fúrások

Рис. 8. Карта изохрон поверхности метаморфического фундамента третичного бассейна (составили: A. PRIBUS, B. SZANYI и V. SÓREG,1990. г.)
1–сейсмические профили, измеренные в 1981-82. гг.; 2–детальные сейсмические профили, измеренные в 1989. г.; 3–изохроны мсек, отнесенные к уровню 50 м н.у.м.; 4–зона разлома; 5–границы предпологаемой зоны компрессии; 6–надвиг; 7–интерпретация по обработке сейслог фирмой Техника : а) нефть; b) газ; 8–скважина; 9–варианты проектной скважины; 10–скважины, рекомендованные фирмой Техника

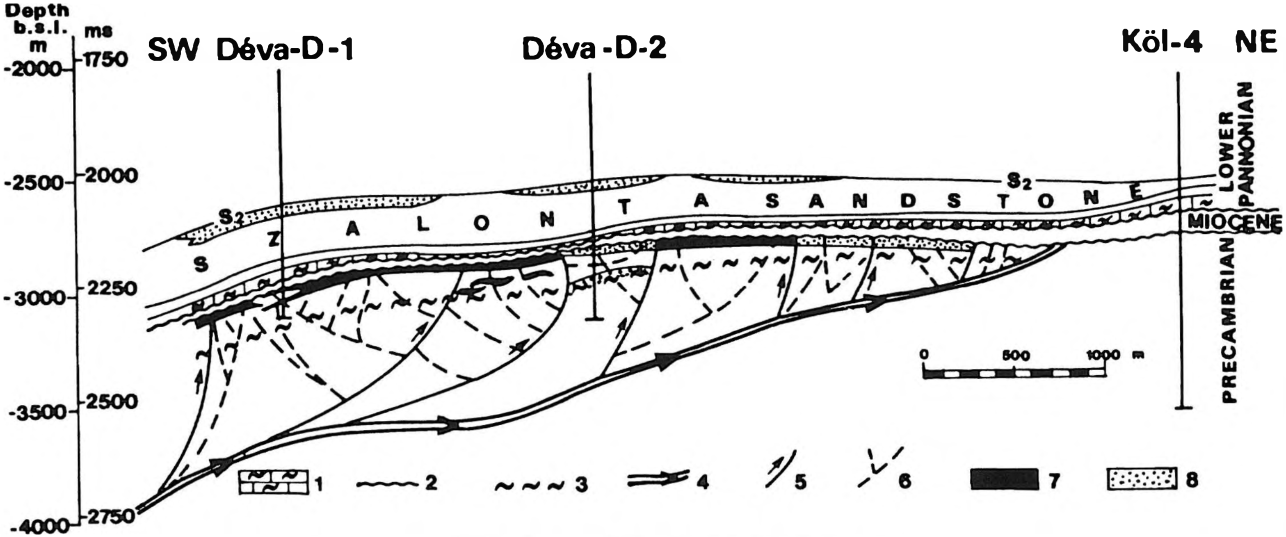

Fig. 9. Seismo-geological section with latest data

1—carbonaceous-marly distal turbidites of Maros Formation Group (Pannonian s.l.); 2—unconformity; 3—uncertain horizon within the crystalline basement; 4—regional overthrust, possible migration conduit; 5—overthrust of lower order limit of block; 6—fault planes; 7—oil accumulation, prediction based on SEISLOG processing; 8—gas accumulation, prediction based on SEISLOG processing

9. ábra. Vázlatos földtani-szénhidrogénföldtani metszet

1—Pannóniai s.l. Marosi Formációcsoport karbonátos, márgás disztális üledékei; 2—diszkordancia felszín; 3—bizonytalan szint a prekambriumi metamorfitban; 4— regionális feltolódási öv, valószínűleg migrációs út; 5—másodlagos feltolódás, blokk-határ; 6—törési síkok; 7—szeizlog feldolgozás alapján lehetséges kőolajfelhalmozódás; 8—szeizlog feldolgozás alapján lehetséges földgázfelhalmozódás

Рис. 9. Схематичный сейсмо-геологический разрез

1—карбонатные и мергеловые дистальные осадочные породы марошской формации паннонского возраста; 2—поверхность несогласия; 3—ненадежно выделенный горизонт в докембрийских метаморфических образованиях; 4—региональная зона надвига, вероятно являющаяся каналом миграции; 5—вторичный надвиг, граница блоков; 6—плоскости разломов; 7—скопление нефти по обработке сейслог; 8—скопление газа по обработке сейслог of hydrocarbons. On the other hand, the normal alkane distribution of crude oils determined by gas chromatography (*Fig. 11*) shows that oils of test No. 2 of well Déva-D-1 and tests Nos. 7 and 8 of well Déva-D-2 have similar composition: the curves shift towards lower carbon atomic numbers. The oils of these three tests contain a higher ratio of lighter hydrocarbons, consequently their paraffin content is higher than that of the others (*Table III*).

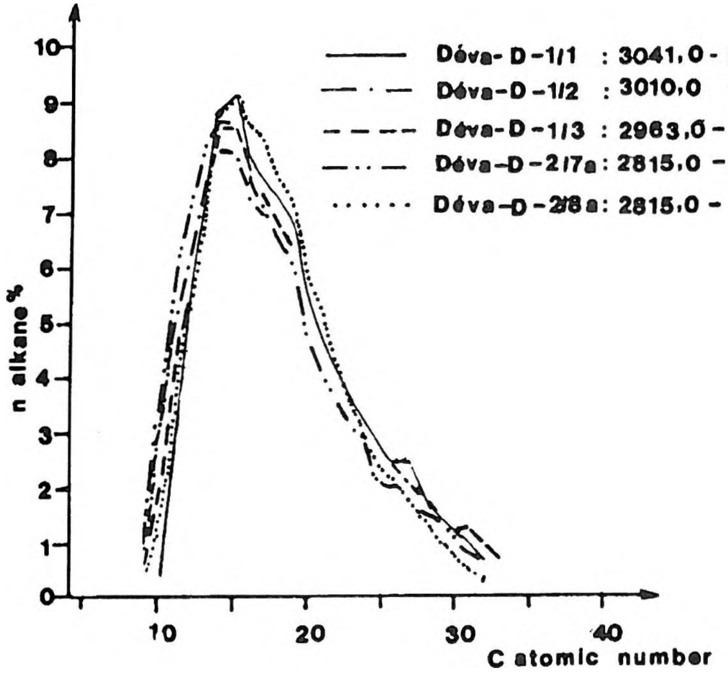

Fig. 10. Normal alkane distribution of distillation residues above 200 °C of oils from the metamorphites of Dévaványa-south area

10. ábra. A Dévaványa-déli terület metamorfitjaiból származó kőolajok 200 °C feletti desztillációs maradékainak normál-alkán eloszlása

Рис. 10. Распределение нормального алькана остатков дистилляции при температуре выше 200 °C нефти из метаморфитов участка Dévaványa-юг

Well number	Déva-D-1			Déva-D-2	
number and location (m) of test	1 3041-3100	2 3010-3014	3 2963-2993	7a 2815-2827	8 2815-2859
C max	15.00	14.00	15.00	14.00	15.00
Pristane Phitane	1.25	1.30	1.23	1.27	1.32
CPI$_{C21-31}$	1.04	1.01	0.99	0.99	1.01
OEP	1.03	0.99	1.01	1.01	1.02
Total paraffin CH (weight %)	54.40	54.30	54.80	54.50	56.60

Table II. Geochemical data of distillation residues above 200 °C of oils from the metamorphites of Dévaványa-south area

II. táblázat A dévaványa-déli kőolajok 200 °C fölötti desztillációs maradékainak adatai

Табл. II. Данные анализа остатков дистилляции при температуре выше 200 °C нефти участка Dévaványa-юг

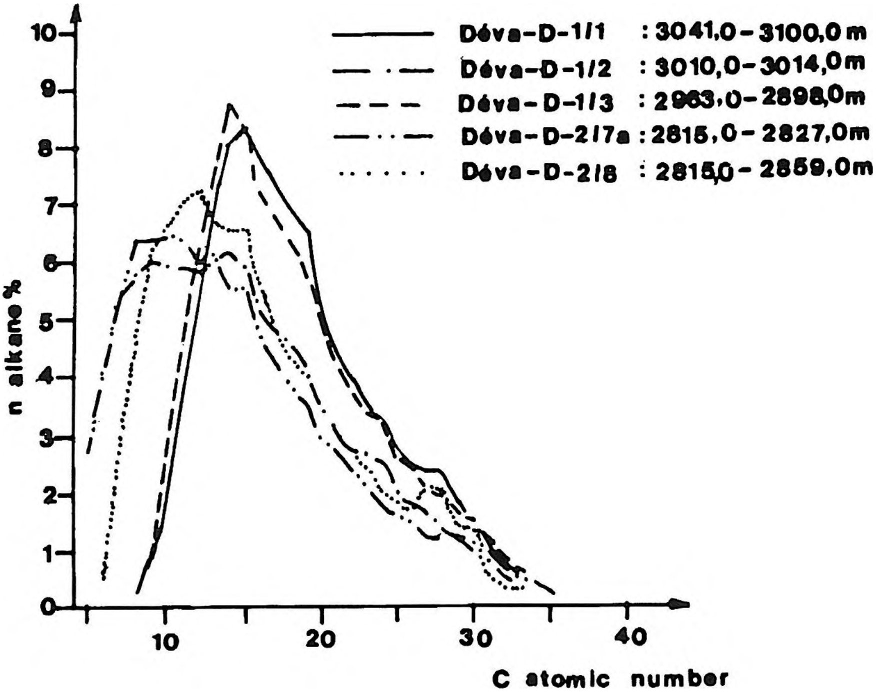

Fig. 11. Normal alkane distribution of crude oils from the metamorphites of Dévaványa-south area

11. ábra. A Dévaványa-déli terület metamorfitjaiból származó kőolajok normál-alkán eloszlása

Рис. 11. Распределение нормального алькана нефти метаморфитов участка Dévaványa-юг

Well number	Déva-D-1			Déva-D-2	
Number and location (m) of test	1 3041-3100	2 3010-3014	3 2963-2993	7a 2815-2827	8 2815-2859
C max	15.00	14.00	14.00	10.00	12.00
$\frac{\text{Pristane}}{\text{Phitane}}$	1.25	1.30	1.23	1.27	1.32
CPI$_{C21-31}$	1.04	1.01	0.99	0.99	1.01
OEP	1.03	0.99	1.01	1.01	1.02
Total paraffin HC (weight %)	58.70	45. 70	46.80	52.30	52.30

Table III. Characteristic geochemical data of crude oils of Dévaványa-south area
III. táblázat A dévaványa-déli nyersolajok jellemző adatai
Табл. III. Характерные данные нефти участка Dévaványa-юг

We had recourse to one more possibility: geoelectric direct hydrocarbon exploration, which might increase the number of hits. The WEGA-D electromagnetic system for measuring resistivity/conductivity and polarizability, was first developed in Poland and it was improved by cooperation between GKV and Polish geophysicists [DZWINEL 1979, DZWINEL 1983, DZWINEL, NAGY 1985, NAGY 1988]. The method is based on the fact that in the vicinity of hydrocarbon fields some special minerogenesis and rock alterations occur, giving rise to conductivity and polarizability changes (in both directions in the case of conductivity, and increase in the case of IP). For the cluster analysis of data, at least two wells (one productive and one dry) have to be in the study area. The result of this analysis is a probability contour map (*Fig. 12*).

4. Conclusions

In contemplating the causes of the differences in the composition of oils, several of them seem to be acceptable. They may have been caused by different migration velocities, or it may be presumed that the oil migrating upwards from the deep Neogene depressions to the SW along the overthrust plane, found remnants of previously migrating oils of different composition and a mixture came into being, or this mixing of different oils occurred during migration. Nevertheless, oil could only reach those parts of the reservoir system which were in contact with the overthrust plane. Therefore even within hydrodynamically distinct blocks no uniform phase order was formed: oil and water can be found above, below and side-by-side each other, depending on partial hydrodynamic connection or separation of fissured, permeable blocks.

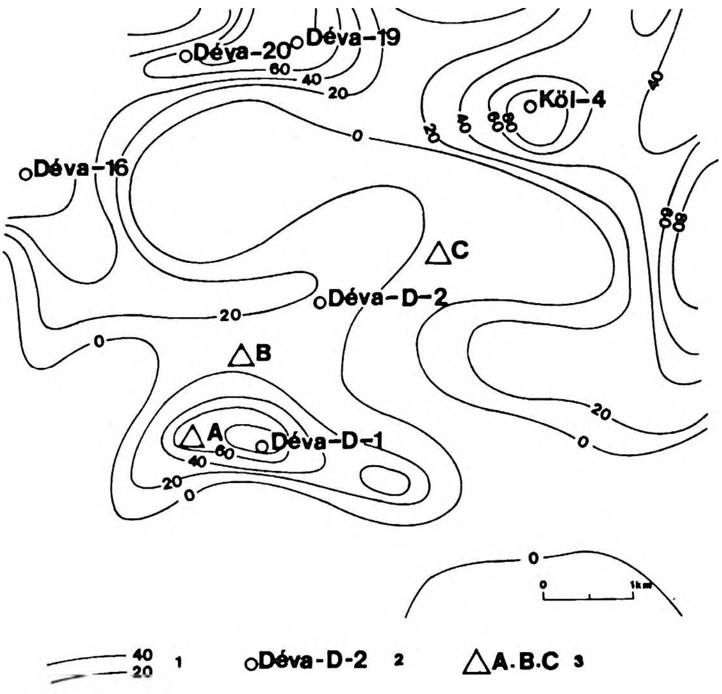

Fig. 12. Probability contour-map of WEGA—D survey
1—probability values in %; 2—existing well; 3—proposed locations for drilling
12. ábra. A terület WEGA-D anomália képe
1—WEGA-D valószínűségértékek %-ban; 2—mélyfúrás; 3—fúrási variációk
Рис.12. АномалииWEGA-D на участке
1—значения вероятности WEGA-D в процентах; 2— скважина; 3— варианты проектных скважин

Clarification of the extremely complex situation is further hindered by infiltrating fluids from deeper reservoirs during layer tests. In addition to the above-mentioned differences in pore fluids, some anomalous temperature (Déva-D-1/3, Fig. 3) and pressure data (Déva-D-2/7, Fig. 5) indicate such partial connection and separation of blocks. It can even be supposed that no reservoirs exist, but instead there are migration conduits in the basement complex, and these provide the inflowing oils in the wells.

In locating further exploration wells, the question is which of the blocks should be drilled. Those blocks near to the limits of the compressional zone (legend 5 in Fig. 8), are most probably too small to contain significant pore volume. Based on their SEISLOG processing, Canadian experts suggested drilling locations for oil in the basement complex and for gas in the Szalonta Sandstone along seismic section Dv-21 (see Fig. 8). However well Déva-D-2 did not verify these predictions. The probability contour lines of the WEGA-D map (Fig. 12) suggest that the most promising parts of the study area have already been drilled, although no test production has been carried out yet. Similarly, 3-D seismics, which may have contributed to the clarification of the situation, was not yet shot.

For further drilling locations we see three possibilities: (i) West of well Déva-D-1, inside the probability anomaly of the WEGA-D map (point A, Fig. 12). In spite of the basement being in a lower position than in the existing well, that block seems to be the biggest (Fig. 8) and once it proved productive, not to mention the probability high. (ii) NNW of well Déva-D-1 (point B in Figs. 8 and 12) for testing the second largest block. This point is the westward projection of Point 2 of Teknica, where the block seems to be broader. (iii) NE of well Déva-D-2 (point C in Figs. 8 and 12) with the task of penetrating the overthrust plane which may be the main migration conduit, containing oil. This is the equivalent of Point 4 of Teknica. It must be admitted, however, that all three points are high-risk investments.

REFERENCES

DZWINEL J. 1979: Direct exploration for hydrocarbons by the WEGA-D system. Proceedings II, 24th Geophysical Symposium, Cracow, pp. 234-244

DZWINEL J. 1983: Fundamental concept and practical aspects of cybernetic systems for direct exploration of mineral deposits. Acta Geophys. Pol. **31**, 3, pp. 307-315

DZWINEL J., NAGY Z. 1985: New achievements in field application of the WEGA-D system. Paper presented at the 47th EAEG Meeting, Budapest, Hungary

NAGY Z. 1988: Controlled source methods and effects of non uniform source fields. IAGA Working Group 3. 9th Workshop on Electromagnetic Induction in the Earth and Moon. 24-31 October, 1988, Sochi-Dagonis, USSR

Interim reports of GKV: A-4/88, A-10/88, A-7/89, A-2/91

A DÉVAVÁNYA-DÉLI METAMORF MEDENCEALJZATI SZERKEZET SZÉNHIDROGÉNKUTATÁSI PROBLÉMÁI — ESETTANULMÁNY

PAP Sándor, SŐREG Viktor és PAPNÉ HASZNOS Irén

1987-ben a Déva-D-1 fúrásban, miután elérte a repedezett breccsásodott aljzatot, vízből és kőolajból álló kétfázisú beáramlás következett be. Mivel a kőolaj mennyisége viszonylag jelentős volt (3 mm-es fúvókán 24,7 m^3/nap kőolaj, 7,1 m^3/nap víz és 1380 m^3/nap éghető gáz) a terület továbbkutatását határoztuk el. 1989-ben a kanadai Teknica cég elkészítette egy, a fúráson átmenő szeizmikus szelvény szeizlog változatát egy másik fúrás elhelyezése céljából. A még ebben az évben lemélyített Déva-D-2 fúrás a medencealjzatot magasabb szerkezeti helyzetben tárta fel, azonban lényegesen kevesebb kőolajat adott mint az előző fúrás. A szerkezeti viszonyok tisztázására 1989-ben újabb szeizmikus mérésekre került sor. Feldolgozva az összes rendelkezésre álló geológiai és geofizikai

információt megállapítható, hogy az erősen tektonizált aljzat egymástól hidrodinamikailag elkülönülő blokkokból épül fel. A blokkok határait különböző típusú vetőzónák jelölik ki. Geokémiai elemzések alapján feltételezhető, hogy a Déva-D-1 fúrás kőolajbeáramlásai nem egy rendszerhez tartoznak és két különböző típusú kőolajból állnak. Felmerül az a lehetőség is, hogy a kőolaj nem telepből vagy telepekből származik, hanem fellazult részekből, tektonikai övekből indulva töredezett zónában migrál. Bár a kockázat nagy, továbbkutatási javaslatokat nyújtottunk be.

ПРОБЛЕМЫ РАЗВЕДКИ УГЛЕВОДОРОДОВ НА УЧАСТКЕ DÉVAVÁNYA-ЮГ С ФУНДАМЕНТОМ, СОСТОЯЩИМ ИЗ МЕТАМОРФИЧЕСКИХ ПОРОД

Шандор ПАП, Виктор ШЕРЕГ, Ирен ПАПНЕ ХАСНОШ

В 1987. г. скважина Déva-D-1 достигла фундамента третичного бассейна, сложенного трещиноватыми, брекчированными породами. После этого в скважину началось просачивание двухкомпонентной жидкости, состоящей из воды и нефти. Так как количество нефти оказалось относительно значительным (через сопла с диаметром 3 мм получены за сутки 24.7 м^3 нефти, 7.1 м^3 воды и 1380 м^3 горючего газа), было решено продолжать исследование. В 1989. г. канадской фирмой Текника был изготовлен вариант сейслог одного из сейсмических разрезов, проходящих через эту скважину, с целью проложения другой.

Пробуренная в этом же году скважина Déva-D-2 вскрыла фундамент в более приподнятом структурном положении, чем Déva-D-1, однако из скважины было получено значительно меньше нефти. Для выяснения структурных соотношений в 1989. г. проводились новые сейсморазведочные измерения. После обработки всей имеющейся геологической и геофизической информации можно установить, что сильно тектонизированный фундамент состоит из гидродинамически отделяющихся друг от друга блоков. Границами блоков являются разнотипные зоны разломов. По данным геохимических анализов можно установить, что нефть скважины Déva-D-1 относится к разным системам и состоит из двух типов. Имеет место и такое предположение, согласно которому нефть получена не из одного или нескольких локальных тел, а мигрирует из раздробленных тектонизированных зон по трещиноватым зонам. Несмотря на большой риск рекомендуется дальнейшее изучение участка.

GEOPHYSICAL TRANSACTIONS 1992
Vol. 37. No. 2-3. pp. 229-240

AMPLITUDE ATTENUATION AND INDUSTRIAL NOISE ORIGIN IN THE EASTERN ALPS

W. LENHARDT* and K. ARIC**

A seismic model of the crust is presented, based on data evaluated by the 'Alpine Explosion Seismology Group' (AESG). Information taken from the amplitudes are derived. It is shown that the amplitude decay in this region can be simulated by introducing a relatively low quality factor (Q) in the crust.

The resulting Q values appear to be relatively small since they include scattering effects. Based on two different seismic phases, direct P-wave and Moho reflections, a crustal model could be divided into an upper and a lower part. The upper crust showed relatively constant absorption with Q at 6 Hz is about 90. In the lower crust a slight trend could be observed, starting with Q=350 in the west and increasing to 550 in the east. Geothermal sources should be situated in the upper crust due to the lower Q at shotpoint F.

Industrial noise covered the range of signal frequencies. Most of the noise could be attributed to agricultural machines and appeared to be monochromatic.

Keywords: seismic modeling, crust, quality factor, absorption, noise

1. Introduction

In September 1975 seismic measurements were carried out in European cooperation on a long range profile (Alp 75) along the strike of the Alps between France and Hungary [AESG, Reporter: H. MILLER 1976]. *Fig. 1a* shows the refraction profiles 04 and 05 of ALP 75 with shotpoints *D* near Innsbruck, *E* near Judenburg and *F* in Hungary and also the main tectonic

---

* Abteilung Geophysik, Zentralanstalt für Meteorologie und Geodinamik, Hohe Warte 38, A-1190 Wien

** Institut für Meteorologie und Geophysik der Universität Wien, Hohe Warte 38, A-1190 Wien
Manuscript received: 28 August, 1989

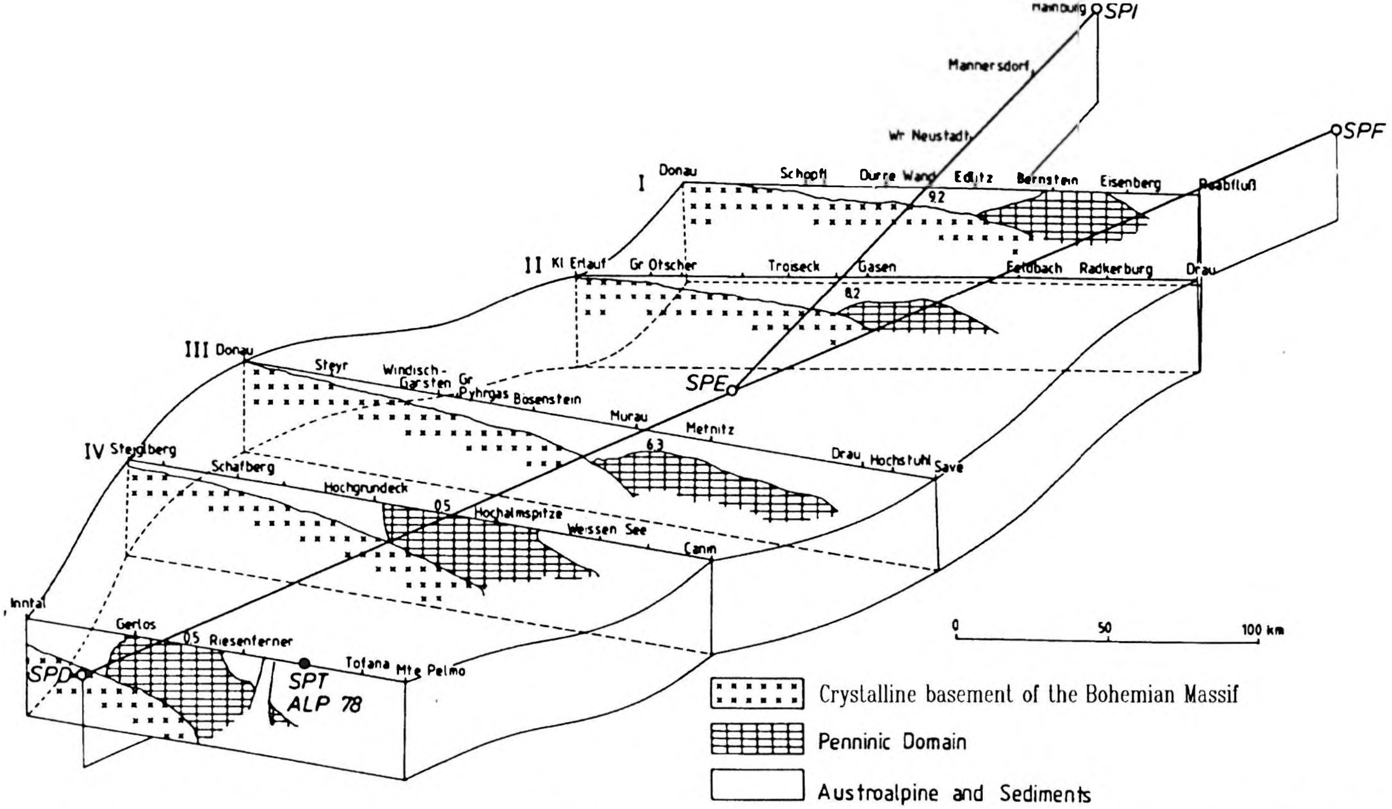

Fig. 1a. Profiles and shotpoints in the eastern parts of ALP 75, the upper crust with tectonic units [after PREY 1980, simplified]. The depth of the basement is given in km

1a. ábra. Szelvények és robbantási pontok az ALP 75 szelvény keleti részén, a felső kéreg tektonikai egységeivel [PREY 1980, egyszerűsítve]. Az aljzat mélysége km-ben van feltüntetve

Рис. 1a. Профили и точки взрыва на восточной части ALP 75 и тектонические единицы верхней коры [PREY 1980, с упрощением]. Глубинные отметки в км units. Some technical data of the ALP 75 shots used in this study are given in *Table I.*

Shot	Type	Elevation (m)	No. of charges	Total charge (TNT), (kg)
D1	Lake	2250	30	1500
D2	Lake	2250	50	2500
E1	Lake	2050	30	1500
E2	Lake	2050	50	2500
F1	Boreholes	200	15	1000
F2	Boreholes	200	32	2000
F3	Boreholes	200	60	4000

Table I. Description of shot points
I. táblázat. A robbantópontok leírása
Табл. I. Описание точек взрыва

Seismic energies were observed up to distances of 500 km with a MARS 66 recorder [BERCKHEMER 1970]. The equipment has a constant transfer function starting at 2 Hz. The seismic records were bandpass filtered from 2 to 30 Hz.

Intensive studies were carried out in seismic modelling based on traveltimes [MILLER et al. 1977, ARIC et al. 1979]. A seismic model for the East Alpine region published by ARIC [1981] was adapted and slightly improved near the shotpoints and at the Moho, to fit the observed amplitudes (*Figs.* 1a, *1b*). For this purpose a ray tracing program [ARIC et al. 1980] was improved in order to include the computation of theoretical amplitudes of first onsets and Moho reflections based on

$$A_{Theor.} = A_0 \cdot ke \cdot kz \cdot ks \cdot ka$$

where

A_0 amplitude at the shotpoint
ke geometrical spreading
kz reflection and transmission coefficient
ks effect of free surface
ka absorption

During the computation of theoretical amplitudes and the evaluation of the recordings, problems of seismic noise were encountered. Therefore, the second part of this paper deals with the identification and problems connected with the seismic noise [LENHARDT 1983]. Especially for the determination of the main signal frequency of the first onset, we found that noise spectra often covered the frequency range of the signal.

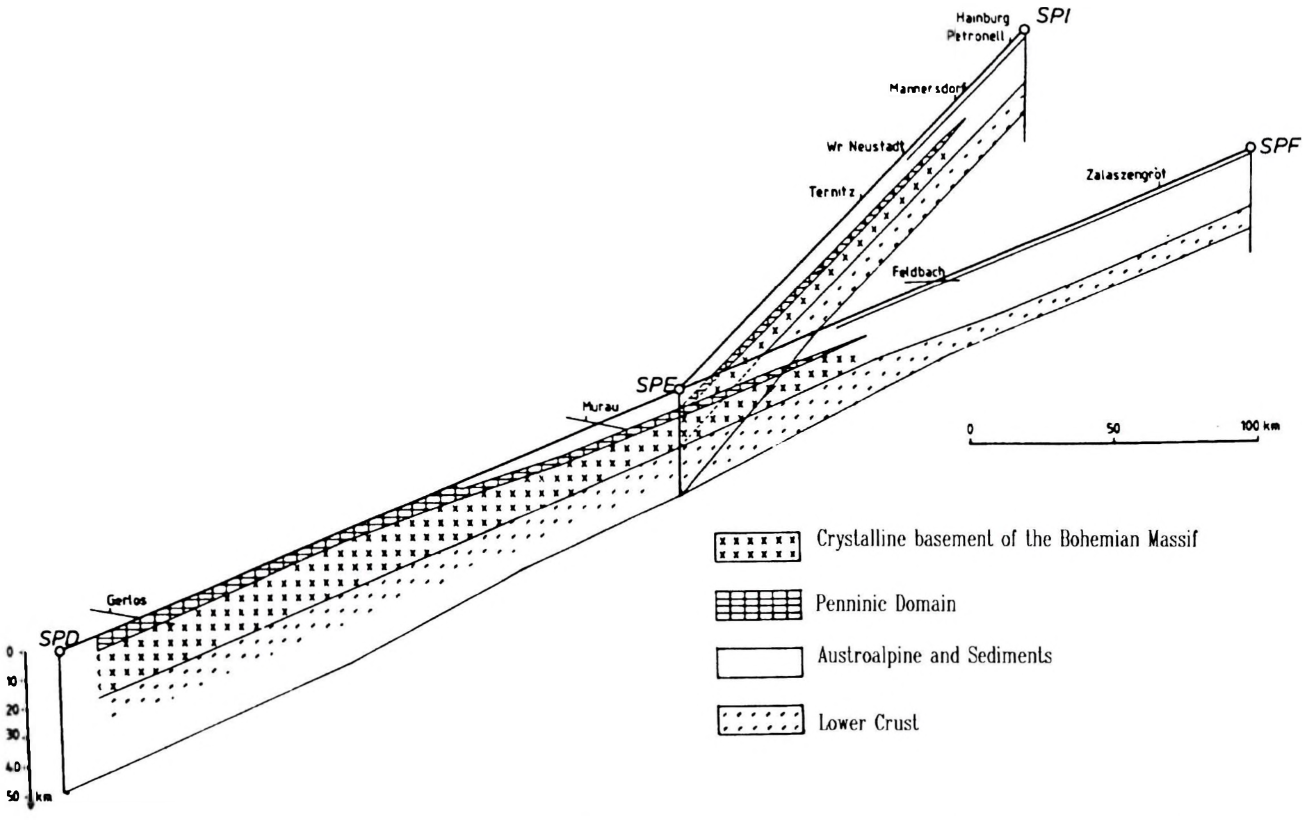

Fig. 1b. Crust in the Eastern Alps and its tectonic geological interpretation based on the available seismic data [Aric 1981]
1b. ábra. A kéreg a Keleti-Alpok területén tektonikai-geológiai értelmezéssel, a rendelkezésre álló szeizmikus adatok alapján [Aric 1981]
Рис. 1b. Земная кора на участке Восточных Альп по имеющимся сейсмическим данным и геолого-тектоническая интерпретация [Aric 1981]

2. First estimation of quality factor in the crust based on an empirical law of amplitude decay

The evaluation of first onsets showed a remarkably constant decay of amplitudes. Therefore, a first estimation of the seismic quality factor *Q* [KNOPOFF 1964] based on a simplified crustal model (see *Figs. 2* and *3*) was carried out [LENHARDT 1983].

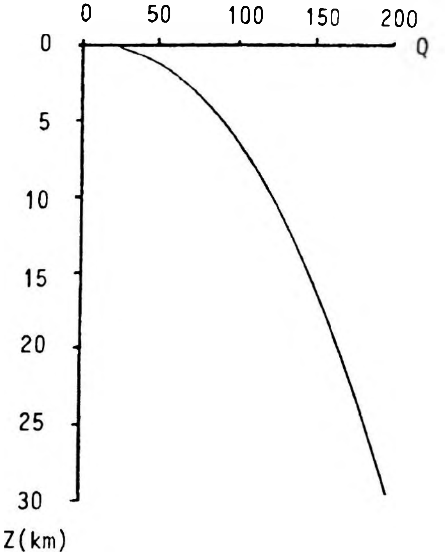

Fig. 2. First estimation of $Q=f(z)$ from an amplitude decay of $x^{-1.8}$ (km)

2. ábra. A $Q=f(z)$ első közelítése $x^{-1.8}$ (km) amplitúdócsökkenéssel

Рис. 2. Первое приближение функции $Q=f(z)$ при затухании амплитуд $x^{-1.8}$ (km)

Empirically we can approximate the observed amplitude decay by

$$A(x) = A_0\, x^{-1.8}$$

which should also agree with the theoretical formula including both geometrical spreading and absorption given by

$$A(x) = \frac{A_0\, e^{-\alpha(x)\, s(x)}}{s(x)}$$

x	surface distance from shotpoint (km)
$\alpha(x)$	depth-dependent absorption coefficient
$s(x)$	length of ray path (km)

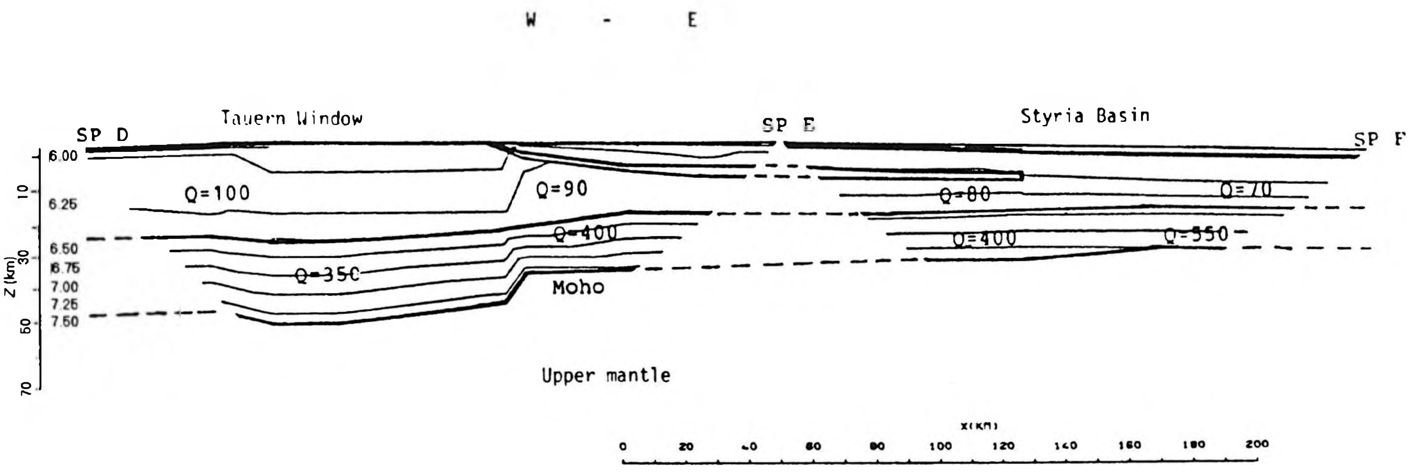

Fig. 3. Model of the crust between shotpoint *D* (Tyrol) and shotpoint *F* (Hungary) derived from traveltimes. The *Q* values computed from *P*-wave amplitudes refer to a frequency of 6 Hz. Accuracy of *Q* is 20 % (see also Figs. 1a, 1b)

3. ábra. A menetidő adatokból levezetett kéregmodell *D* (Tirol) és *F* (Magyarország) robbantópontok között. A *P*-hullám amplitúdókból számított *Q* értékek 6 Hz-re vonatkoznak. *Q* pontossága 20 % (lásd még 1a, 1b ábrákat)

Рис. 3. Модель коры, полученная по данным времени хода между точки взрыва *D* (Тирол) и *F* (Венгрия). Значения *Q*, расчитанные по амплитудам волн *P*, относятся к частоте 6 гц. Точность параметра 20 проц (см. также рис. 1a. и 1b.)

α is related to Q by

$$Q = \frac{2\,\pi}{1 - e^{-2\,\alpha\,\lambda}}$$

with λ wavelength. In a lateral homogenous medium with constant gradient, the maximum depth of ray penetration is tied to the surface distance of emergence by

$$z(x) = \left(\frac{x^2}{4} + \frac{v_0^2}{b^2}\right)^{\frac{1}{2}} - \frac{v_0}{b}$$

$z(x)$	maximum depth (km)
v_0	P-wave velocity at surface (km/s)
b	gradient of the v_0

hence $\alpha(x)$ as a function of depth can be described by the observation distance $\alpha(x) \approx \alpha(z)$. To find a variation of the absorption coefficient with depth or distance, we can solve the problem iteratively by incrementing the observation distance x (equivalent to the depth of penetration of the seismic ray) taking into account the absorption which was computed from the layers above.

Therefore

$$\alpha_i = \frac{-\ln\left((s_i + 2\sum_{j=1}^{i-1} s_j) \,/\, (x_i^{-1.8} \prod_{j=1}^{i-1} e^{-2\,\alpha_j s_j})\right)}{s_i}$$

x_i	surface distance (km)
s_i	ray path length in layer i (km)
s_j	ray path length in layer j (km)
α_j	absorption coefficient of layer j

The factor 2 in the summation of the ray paths in the recently computed layers refers to the down and upgoing ray. By introducing the simple model for the crust with velocity of

$$v = v_1 + k \cdot z\,; \quad v_1 = 6.00 \text{ km/s}\,; \quad k = 0.04 \text{ 1/s}$$

z	depth (km)
v	average P-wave velocity (km/s) from z (km)

and the initial condition where the first layer has a constant absorption and velocity, we find the depth dependence of Q. Figure 2 shows the resulting discrete function $Q=f(z)$ using the dominant frequency of 6 Hz.

In the upper part of the model we get Q values less than 150. Since the lower crust should show much higher values (Fig. 3), a ray tracing program was adapted to enable Q to be computed from a crustal model derived from traveltimes observed in the East Alpine region. By using both of the first onsets (refracted P-waves) and reflections from the Moho, it was possible to divide the crust into an upper and a lower layer with constant Q. As a result of three shotpoints at large distances from each other (distance about 220 km) a slight lateral change in Q becomes apparent (Fig. 3).

It can be stated that the upper crust has an almost constant Q of about 90. ARIC et al. [1980] introduced a low-velocity layer in the upper crust near to shotpoint E to explain reflection onsets. This thin zone at a depth between 8 and 12 km was interpreted by ARIC [1981] as the 'Schieferhülle' of the Austroalpine unit (PREY [1980], see Figs. 1a and 1b). This layer is also supported by theoretical amplitudes which show their maximum in the observed range between 60 and 90 km.

The absorption in the lower crust seems to be very much less, hence the Q-factor is higher. We find Q values of 350 in the western part which increase to 550 in the east shotpoint F. This result contradicts the usual concept of low Q — high geothermal gradient. Therefore the source of heat in Hungary has to be expected in the upper crust [ARIC et al. 1987].

Knowledge of the origin of seismic noise is interesting from several aspects. First of all the design of a seismic array strongly depends on the background seismicity. Further, if recorded data are disturbed by unwanted stationary time series, the design of filters can be optimized by applying a noise analysis. Practically all unwanted signals and time series are usually understood as noise. Now we can differentiate between sources of natural origin and those that are man-made. Whereas emitted time series of natural sources are extremely broadbanded due to different mechanisms like tides, wind and natural background seismicity, man-made noise in the near field due to industry mainly lies between 2 and 50 Hz. Especially in this frequency range we have to expect signals on the seismic long range profiles.

The evaluation of industrial noise is determined and limited by amplification. Recordings in the near field (10 km) could not be used since the signal to noise ratio was too high and a filter to remove the noise became ineffective. Due to the amplification which is chosen for a good evaluation of the first onset, the noise is simply covered by white noise from digitizing.

As a lower level of industrial noise an empirical amplitude of 10^{-4} cm/s was chosen.

3. Evaluation and identification of seismic noise

As mentioned above only a frequency range from 2 to 30 Hz can be interpreted. Time intervals of 256 samples equivalent to 2.56 seconds were analysed by FFT [COOLEY and TUKEY 1965] of each vertical component. Since the amplitude decay approximately follows an exponential law we have a short explanation on the distribution of noise amplitudes for the profiles (*Fig. 4*).

The amplitudes of the seismic waves which were caused by the charges fired by ALP 75, were comperable if they were weighted by $x^{1.8}$ (km). Yet Fig. 4 shows a signal to noise ratio exceeding 1.0 in about 100 km which calls for effective filtering in the far field for that charge and geometry of blasting. At distances up to 100 km first onsets and noise amplitudes can have similar amplitudes (Fig. 4). It should be mentioned that any kind of distributed shots (borehole, lake) produced similar signals and the frequency range always overlapped with that of the noise. A variation of signal

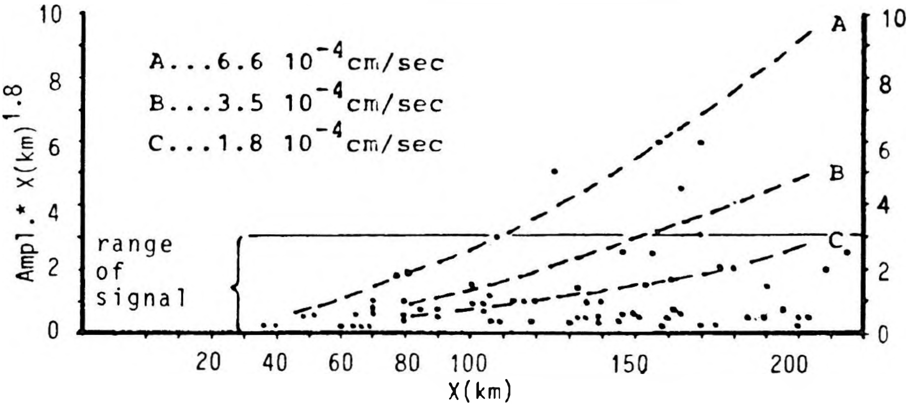

Fig. 4. Noise amplitudes on both profiles and their increase due to distance weighting to ensure that the amplitude of the first onset is constant. The dots are the observed noise amplitudes along the profiles. The signal has a reference amplitude from 0.1 to 3. Minimum noise amplitude belongs to $1\cdot10^{-4}$ cm/s

4. ábra. Zaj-amplitúdók a szelvényeken és növekedésük az első beérkezések konstans amplitúdóját biztosítva a távolság szerinti súlyozásnak megfelelően. A pontok az észlelt zaj-amplitúdókat jelölik. A jel referencia amplitúdószintje 0,1-3. A minimális zaj-amplitúdó $1\cdot10^{-4}$ cm/s-nak felel meg

Рис. 4. Амплитуда шумов по профилю и ее увеличение согласно взвешиванию по расстоянию при сохранении постоянства амплитуды первых поступлений. Точками обозначены наблюденные амплитуды шума. Уровень амплитуды опорного сигнала 0.1-3. Минимальная амплитуда шума соответствует $1\cdot10^{-4}$ см/сек form by shot geometry and charge on a long-range profile seems to be impossible due to the absorption of seismic waves in the earth.

Noise interpretation can be carried out only at distances greater than 10 km from the shotpoint. At smaller distances the amplification of the equipment was usually very low in order to read the amplitudes. Similarly MEISSNER and STEGENA [1977] (pp. 51-53) observed that a noise level of 10^{-4} cm/s limits the radius (10 km) of seismic observations around each station.

Especially next to the Tauern window (Fig. 3), in absence of any industry, only 16 2/3 Hz were observed but not completely explained. The Austrian Railway usually uses this frequency otherwise it should not influence stations at a distance of more than 10 km (*Fig. 5*). One feature which appeared very soon was the strong amplification of low frequency noise (2-5 Hz) in sedimentary basins as described STEIN et al. [1967] and PLESINGER and WIELAND [1974], in the same range of amplification of factor 10. Extremely high absorption in sediments is the reason for the loss of the higher parts of the frequency spectrum and the low frequency parts of the seismic signature are enhanced due to resonance.

Low frequencies (4-6 Hz) are also produced by industrial organizations equipped with machines such as saw-mills (Fig. 5) which are very frequent in the Alpine region. Other industries (coal mining, steel) cover a frequency range from 2-6 Hz that is precisely the expected spectra from blasts in the far field. Since the frequency content of the *P*-wavelet lies between 5 and 6 Hz for *P*-waves at distances from 30 to 200 km, monochromatic noise emitted by industry could be eliminated by using filters.

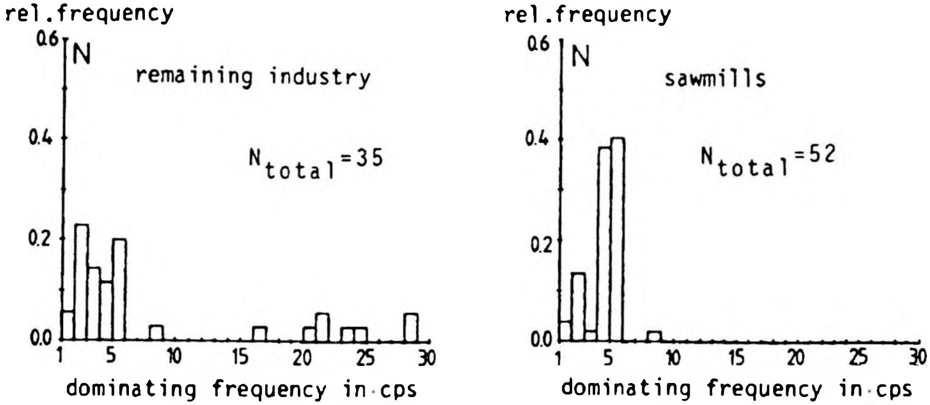

Fig. 5. Dominating frequencies of noise and their corresponding sources
5. ábra. Domináns zaj-frekvenciák és a hozzájuk tartozó források
Рис.5. Доминирующие частоты шума и отвечающие им источники

Acknowledgement

This study is part of international project P 5612 (Struktur und Bewegung der Lithosphäre) and was financially supported by the 'Fonds zur Förderung der wissenschaftlichen Forschung' in Austria and by the Austrian Academy of Sciences (Geophysical Commission) in Vienna.

REFERENCES

AESG Reporter MILLER H. 1976: A Lithospheric Seismic Profile along the Axis of the Alps, 1975. I: First Results. Pageoph. **114**, 6, pp. 1109-1120

ARIC K. 1981: Deutung krustenseismischer und seismologischer Ergebnisse in Zusammenhang mit der Tektonik des Alpenostrandes. ÖAW, Math. nat. wiss. Kl. Abt. I, 190, **8**, Springer Verl., Wien

ARIC K., GUTDEUTSCH R., KLINGER G., LENHARDT W. 1987: Seismological studies in the Eastern Alps. Geodynamics of the Eastern Alps. F. Deuticke Verl., Wien

ARIC K., GUTDEUTSCH R., SAILER A. 1980: Computation of Travel Times and Rays in a Medium of Two-dimensional Velocity Distribution. Pageoph. **118**, 3, pp. 796-806

ARIC K., ALBU I., GUTDEUTSCH R., MITUCH E., POSGAY K. 1979: Deutung der refraktionsseismischen Messungen auf dem östlichen Abschnitt des Alpenlängsprofiles. Acta Geodaet., Geophys. et Montanist. Acad. Sci. Hun. Tom. **14**, 1-2, pp. 237-245

BERCKHEMER H. 1970: MARS 66. Eine Magnetbandapparatur für seismische Tiefensondierung. Zft. f. Geoph. **36**, 4, pp. 501-518

COOLEY J. W., TUKEY J. W. 1965: An algorithm for the machine calculation of complex Fourier series. Math. of Computation **19**, 90, pp. 297-301

KNOPOFF L. 1964: Q. Rev. Geoph. **2**, 4, pp. 625-660

LENHARDT W. 1983: Bestimmung der Absorptionseigenschaften der Erdkruste im Bereich der Ostalpen. Dissertation, Univ. Wien

MEISSNER R., STEGENA L. 1977: Praxis der seismischen Feldmessung und Auswertung. Studienhefte zur Angewandte Geophysik 1, Geb. Borntraeger, Stuttgart, Akadémiai Könyvkiadó, Budapest, 275 p.

MILLER H., GEBRANDE H. and SCHMEDES E. 1977: Ein verbessertes Strukturmodell für die Ostalpen, abgeleitet aus refraktionsseismischen Daten unter Berücksichtigung des Alpenlängsprofiles. Geol. Rundschau **66**, pp. 289-308

PLEŠINGER A. and WIELANDT E. 1974: Seismic noise at 2 Hz in Europe. J. Geoph. **40**, 1, pp. 131-136

PREY S. 1980: Die Geologie Österreichs in ihrem heutigen geodynamischen Entwicklungsstand sowie die geologischen Bauteile und ihre Zusammenhänge. *In*: Der Geologische Aufbau Österreichs. Springer Verl., Wien

STEIN A., STEINBECK J., VECCHIA O. and FRÖHLICH R. 1967: Deep seismic sounding in the plain of Po and the Central Alps. General Assembly IUGG, Zürich

AMPLITÚDÓCSILLAPODÁS ÉS IPARI ZAJOK EREDETE A KELETI-ALPOKBAN

W. LENHARDT és K. ARIC

Az "Alpine Explosion Seismology Group" (AESG) által kiértékelt adatokon alapuló szeizmikus kéregmodell kerül bemutatásra. Levezetik az amplitúdókból nyerhető információkat és megmutatják, hogy az amplitúdócsökkenés ezen a területen a kéregre vonatkozó, viszonylag kicsi Q faktor bevezetésével szimulálható.

Az eredményként kapott Q értékek alacsonynak bizonyultak mivel tartalmazzák a szóródási hatásokat. Két különböző szeizmikus fázisnak megfelelően—direkt P-hullám és Moho-reflexiók—a kéregmodell egy felső és egy alsó részre osztható. A felső kéreg viszonylag állandó abszorpciót mutatott Q=90 értékkel 6 Hz-nél. Az alsó kéregben egy enyhe emelkedő tendencia figyelhető meg Q=350-től Q=550-re, nyugatról kelet felé haladva. Az F robbantópontnál jelentkező alacsonyabb Q-nak megfelelően geotermikus forrás valószínű a felső kéregben.

Az ipari zajok lefedték a jelfrekvenciák tartományát. A zajok legnagyobb része monokromatikusnak bizonyult és mezőgazdasági berendezéseknek tulajdonítható.

ПРИЧИНА ЗАТУХАНИЯ АМПЛИТУД И ПРОМЫШЛЕННЫХ ШУМОВ В ВОСТОЧНЫХ АЛЬПАХ

В. ЛЕНХАРДТ, К. АРИК

Показывается сейсмическая модель земной коры, основанная на интерпретации данных, выполненной (AESG). Приводятся данные, получаемые по амплитудам, и показывается, что затухание амплитуд на участке хорошо симулируется введением фактора Q относительно небольшой величины, и отнесенной к коре.

Полученные в результате величины Q оказались низкими в связи с влиянием дисперсии. Модель коры, составленная по двум разным волнам (прямая P волна и отражения от поверхности Мохо), разделяется на верхнюю и нижнюю часть. Верхняя кора характеризуется постоянством абсорбции при Q=90 на 6 гц. В нижней коре отмечается тенденция слабого повышения значения Q с запада Q=350 на восток Q=550. Согласно низким значениям Q у точки взрыва F в верхней коре предпологается наличие геотермического источника.

Диапазон частот сигналов перекрыт шумом промышленного происхождения. Основная часть шумов оказалась монохроматичной, и, по-видимому,связана с работой сельскохозяйственной техники.


Strike oil
by advertising
with us

ALLIED ASSOCIATES GEOPHYSICAL LTD

79-81 Windsor Walk, Luton, Beds England LU1 5DP Tel (0582) 425079 Telex 825562 Fax (0582) 480477

UK's LEADING SUPPLIER OF RENTAL GEOPHYSICAL, GEOTECHNICAL, & SURVEYING EQUIPMENT

SEISMIC EQUIPMENT

Bison IFP 9000 Seismograph
ABEM Mark III Seismograph
Nimbus ES1210F Seismograph Complete
Single Channel Seismograph Complete
DMT-911 Recorders
HVB Blasters
Geophone Cables 10 20 30M Take Outs
Geophones
Single Channel Recorders
Dynasource Energy System
Buffalo Gun Energy System

MAGNETICS

G-856X Portable Proton Magnetometers
G-816 Magnetometers
G-826 Magnetometers
G-866 Magnetometers

GROUND PROBING RADAR

SIR-10 Consoles
SIR-8 Console
EPC 1600 Recorders
EPC 8700 Thermal Recorders
120 MHz Transducers
80 MHz Transducers
500 MHz Transducers
1 GHz Transducers
Generators
Various PSU's
Additional Cables
Distance Meters

GRAVITY

Model "D" Gravity Meters
Model "G" Gravity Meters

EM

EM38
EM31 Conductivity Meter
EM16 Conductivity Meter
EM16/16R Resistivity Meters
EM34 Conductivity Meter 10, 20, 40M Cables
EM37 Transient EM Unit

RESISTIVITY

ABEM Terrameter
ABEM Booster
BGS 128 Offset Sounding System
BGS 256 Offset Sounding System
Wenner Array

In addition to rental equipment we currently have equipment for sale. For example ES2415, ES1210F, EM16/16R, G-816, G856, G826/826A, equipment spares.

NOTE: *Allied Associates stock a comprehensive range of equipment spares and consumables and provide a repair & maintenance service.*

We would be pleased to assist with any customer's enquiry. Telephone (0582) 425079

Place your order through our first agency in Hungary.

To place an order, we request the information listed in the box below.

1. Customer name
   (a maximum of 36 characters)
2. Customer representative
3. Shipping address
4. Mailing or billing address
   (if different)
5. Telephone, Telex or Fax number
6. Method of shipment

ELGI c/o L. Verő
Columbus St. 17-23
H - 1145 Budapest, Hungary
PHONE: 36-1-1637-438
FAX: 36-1-1637-256

• *Orders must be placed and prepaid with ELGI.*

SOFTWARE
for Geophysical and
Hydrogeological
Data Interpretation,
Processing & Presentation

INTERPEX LIMITED

715 14th Street ■ Golden, Colorado 80401 USA ■ (303) 278-9124 FAX: (303) 278-4007

DON'T BUY EQUIPMENT OR SERVICES UNTIL YOU KNOW THE FACTS

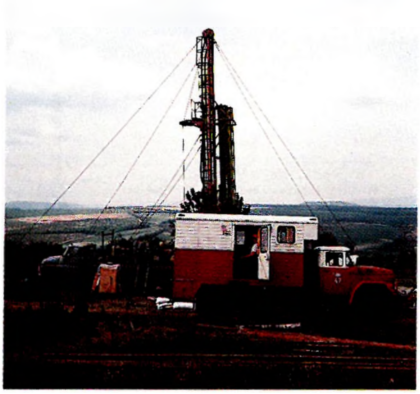

ELGI's Well Logging Divison has put its 25 years of experience to work again in the new line of well logging technology in
water,
coal,
mineral,
geotechnical
prospecting

HERE'S WHAT WE OFFER

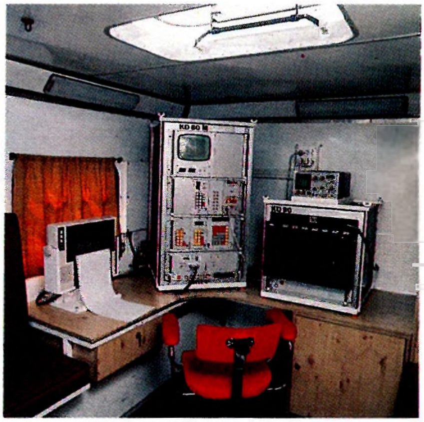

- Complete series of surface instruments from portable models to the PC controlled data logger
- Sondes for all methods: electrical, nuclear, acoustic, magnetic, mechanical, etc.
- Depth capacity down to 5000 m
- On-site or office computer evaluation
- International Metrological Base for calibration to true petrophysical parameters
- Training and in-house courses
- Design laboratory for custom-tailored assemblies

Just think of us as the scientific source of borehole geophysics you may never have heard of

SALES ✤ ✤ ✤ ✤ RENTALS ✤ ✤ ✤ ✤ SERVICES

Well Logging Division of ELGI
POB 35, Budapest, H-1440 Hungary
Phone: (361) 252-4999, Telex: 22-6194,
Fax: (361) 183-7316

INVITATION

The Association of Hungarian Geophysicists decided at its annual meeting to establish the "Foundation for Hungarian Geophysicists" and elected its first Advisory Board for 3 years. The foundation has been started with a moderate initial capital of 300 000 HUF, which has by now increased to more than 3 million and it is open for everybody.

The aim of the foundation is to help Hungarian geophysicists. There are two main target groups whose application for grants will be accepted with preference: young geophysicists needing assistance (travels, participation at conferences, publications,post-graduate education etc.) at the beginning of their professional life as well as retired and unemployed colleagues whose economic and social position became especially unfavourable.

The nine members of the Advisory Board invite everybody to join this foundation; donations should be communicated with the Board. Organisations and persons donating sums exceeding the initial capital will have the opportunity to delegate representatives into the Board. Detailed information is available at the following address:

Advisory Board of the
"Foundation for Hungarian Geophysicists"
H-1371 Budapest, P.O.B. 431
Budapest, I., Fő u. 68.
Telephone 201-2011/590
Telex 22-4343
Telefax 156-1215

Copyright

Authorization to photocopy items for internal or personal use in research, study or teaching is granted by the Eötvös Loránd Geophysical Institute of Hungary for individuals, instructors, libraries or other non- commercial organizations. We permit abstracting services to use the abstracts of our journal articles without fee in the preparation of their services. Other kinds of copying, such as copying for general distribution, for advertising or promotional purposes, for creating new collective works, or for resale are not permitted. Special requests should be addressed to the Editor. There is no charge for using figures, tables and short quotes from this journal for re-publication in scientific books and journals, but the material must be cited appropriately, indicating its source.

Az Eötvös Loránd Geofizikai Intézet hozzájárul ahhoz, hogy kiadványainak anyagáról belső vagy személyes felhasználásra kutatási vagy oktatási célokra magánszemélyek, oktatók, könyvtárak vagy egyéb, nem kereskedelmi szervezetek másolatokat készítsenek. Engedélyezzük a megjelentetett cikkek összefoglalóinak felhasználását referátumok összeállításában. Egyéb célú másoláshoz, mint például: terjesztés, hirdetési vagy reklám célok, új, összefoglaló jellegű anyagok összeállítása, eladás, nem járulunk hozzá. Az egyedi kéréseket kérjük a szerkesztőnek címezni. Nem számolunk fel díjat a kiadványainkban szereplő ábrák, táblázatok, rövid idézetek más tudományos cikkben vagy könyvben való újrafelhasználásáért, de az idézés pontosságát és a forrás megjelölését megkívánjuk.